COLOR SCIENCE AND TECHNOLOGY OF NOVEL NANOPHOSPHORS FOR HIGH-EFFICIENCY HIGH-QUALITY LEDs

A THESIS
SUBMITTED TO THE DEPARTMENT OF ELECTRICAL AND ELECTRONICS ENGINEERING
AND THE GRADUATE SCHOOL OF ENGINEERING AND SCIENCE
OF BILKENT UNIVERSITY
IN PARTIAL FULLFILMENT OF THE REQUIREMENTS
FOR THE DEGREE OF
MASTER OF SCIENCE

By
Talha Erdem
August 2011

I certify that I have read this thesis and that in my opinion it is fully adequate, in scope and in quality, as a thesis for the degree of Master of Science.

_____

Assoc. Prof. Dr. Hilmi Volkan Demir (Supervisor)

I certify that I have read this thesis and that in my opinion it is fully adequate, in scope and in quality, as a thesis for the degree of Master of Science.

_____

Prof. Dr. Ayhan Altıntaş

I certify that I have read this thesis and that in my opinion it is fully adequate, in scope and in quality, as a thesis for the degree of Master of Science.

_____

Assoc. Prof. Dr. Dönüş Tuncel

Approved for the Graduate School of Engineering and Science:

_____

Prof. Dr. Levent Onural

Director of the Graduate School of Engineering and Science

ABSTRACT

COLOR SCIENCE AND TECHNOLOGY OF NOVEL NANOPHOSPHORS FOR HIGH-EFFICIENCY HIGH-QUALITY LEDs

Talha Erdem
M.S. in Electrical and Electronics Engineering
Supervisor: Assoc. Prof. Dr. Hilmi Volkan Demir

August 2011

Today almost one-fifth of the world's electrical energy is consumed for artificial lighting. To revolutionize general lighting to reduce its energy consumption, high-efficiency, high-quality light-emitting diodes (LEDs) are necessary. However, to achieve the targeted energy efficiency, present technologies have important drawbacks. For example, phosphor-based LEDs suffer from the emission tail of red phosphors towards longer wavelengths. This deep-red emission decreases substantially the luminous efficiency of optical radiation. Additionally, the emission spectrum of phosphor powders cannot be controlled properly for high-quality lighting, as this requires careful spectral tuning. At this point, new nanophosphors made of colloidal quantum dots and crosslinkable conjugated polymer nanoparticles have risen among the most promising alternative color convertors because they allow for an excellent capability of spectral tuning. In this thesis, we propose and present high-efficiency, high-quality white LEDs using quantum dot nanophosphors that that exhibit luminous efficacy of optical radiation ≥380 lm/W_{opt}, color rendering index ≥90 and correlated color temperature ≤4000 K. We find that Stoke's shift causes a fundamental loss >15%, which limits the maximum feasible luminous efficiency to 326.6 lm/W_{elect}. Considering a state-of-the-art blue LED (with 81.3% photon conversion efficiency), this corresponds to 265.5 lm/W_{elect}. To achieve 100 and

200 lm/W_{elect}, the layered quantum dot films are required to have respective quantum efficiencies of 39 and 79%. In addition, we report our numerical modeling and experimental demonstrations of the quantum dot integrated LEDs for the different vision regimes of human eye. Finally, we present LEDs based on the color tuning capability of conjugated polymer nanoparticles for the first time. Considering the outcomes of this thesis, we believe that our research efforts will help the development and industrialization of white light emitting diodes using nanophosphor components.

Keywords: White light emitting diodes (white LED), color science, photometry, luminous efficacy, color rendering, color temperature, color tuning, spectral tuning.

ÖZET

NANOFOSFORLARIN YÜKSEK VERİMLİLİK YÜKSEK KALİTE LED UYGULAMALARI İÇİN RENK BİLİMİ VE TEKNOLOJİSİ

Talha Erdem
Elektrik ve Elektronik Mühendisliği Bölümü Yüksek Lisans
Tez Yöneticisi: Doç. Dr. Hilmi Volkan Demir
Ağustos 2011

Günümüzde dünya enerji tüketiminin yaklaşık beşte biri yapay aydınlatma için kullanılmaktadır. Genel aydınlatma uygulamalarında bu enerji tüketimini düşürecek teknolojik devrimi hayata geçirebilmek için verimliliği ve kalitesi yüksek ışık yayan diyotların (LED) kullanımına geçilmesi bir zorunluluk haline gelmiştir. Ancak hedeflenen verimlilik seviyelerine ulaşabilmek için günümüz teknolojilerinin önemli zaafları vardır. Örneğin, fosfor tabanlı LED'lerin en büyük sorunları arasında kırmızı fosforların uzun dalgaboylarına uzanan ışıma spektrumları yer almaktadır. Bu derin-kırmızı bölgedeki ışıma, optik ışımanın aydınlatma verimliliğini (LER) önemli düzeyde azaltmaktadır. Bunlara ek olarak, fosfor tozlarının ışıma spektrumlarının kontrol edilemeyişi dikkatli spektrum ayarlanabilirliğini gerektiren yüksek kaliteli aydınlatma uygulamaları için sorun teşkil etmektedir. Bu noktada, kolloid kuantum noktacıkları ve çapraz zincirlenebilir polimer nanoparçacıklar spektrum kontrolüne izin vermelerinden dolayı var olan renk dönüştürücü malzemelere alternatif olarak öne çıkmaktadırlar. Bu tezde kuantum noktacık nanofosforlar kullanarak yüksek verimlilikte ve kalitede beyaz LED'leri teklif ediyor ve gösterimini yapıyoruz. Bu LED'lerin optik ışımanın aydınlatma verimliliği değerleri 380 lm/W_{opt}'den, renk dönüşüm indisleri ise 90'dan daha yüksek değerlere ulaşabilmekte; benzer renk sıcaklığı ise 4000 K'in altında yer almaktadır. Sadece Stock kaymasından

kaynaklanan temel kaybın en az %15 olduğunu ve elektriksel aydınlatma verimliliğinin (LE) en yüksek 326.6 lm/W_{elect} olabileceğini yine bu tezde gösteriyoruz. Bu da güç dönüşüm verimliliği açısından günümüzün en iyi mavi LED'leri kullanıldığında (%81.3), 265.5 lm/W_{elect} seviyesinde bir elektriksel aydınlatma verimliğine denk gelmektedir. 100 ve 200 lm/W_{elect} seviyesine ulaşmak için katmanlı kuantum noktacık filmlerinin verimliliklerinin sırasıyla %39 ve %79 olması gerekmektedir. Bu iç aydınlatma uygulamaları için yapılan çalışmaların yanında, diğer görme modları için de modelleme ve deneysel gösterimlerimiz yine bu tez içerisinde yer almaktadır. Son olarak, renk kontrolüne imkân veren konjüge edilmiş polimer nanoparçacıkların da ilk defa bir LED tasarımında kullanımını rapor ediyoruz. Bu tezdeki çalışmalarımızı göz önüne alarak, çalışmalarımızın nanofosfor temelli beyaz LED'lerin geliştirilmesi ve endüstrileşmesinde önemli katkıları olacağını ummaktayız.

Anahtar Kelimeler: Beyaz ışık yayan diyotlar (beyaz LED), renk bilimi, aydınlatma verimliliği, renk dönüşümü, renk sıcaklığı, renk kontrolü, spektrum kontrolü.

Acknowledgements

“Bihî, the word that adorns every other word…”

As one of the major milestones of my life, herewith I finished my MS studies with this thesis. There have been a lot of people who helped and supported me during this process, which had been sometimes very stressful and sometimes very entertaining. I owe many thanks to all of them.

First, I would like to thank my supervisor Prof. Hilmi Volkan Demir. He helped and supported me in every part of this thesis; more importantly, he has been always very kind and friendly to me. I would also like to thank Prof. Dönüş Tuncel, who has guided and helped me during our collaborative works. I owe many thanks to Prof. Ayhan Altıntaş, who has accepted to be in my thesis committee.

Dr. Sedat Nizamoglu and Evren Mutlugün have never hesitated to help me. More importantly, they have been great guides in my research as well as great friends of mine. Their friendship will never be forgotten.

I would also like to thank all the past and present members of Demir Group: Emre Sarı, Tuncay Özel, Rohat Melik, İlkem Özge Özel, Aslı Yılmaz, Gülis Zengin, Neslihan Çiçek, Refik Sina Toru, Can Uran, Cüneyt Eroğlu, Onur Akın, Kazım Gürkan Polat, Mustafa Akın Sefünç, Burak Güzeltürk, Hatice Ertuğrul, Sayım Gökyar, Veli Tayfun Kılıç, Kıvanç Güngör, Ahmet Fatih Cihan, Shahab Akhavan, Yusuf Keleştemur, Yasemin Coşkun, Durmuş Uğur Karatay, Ozan Yerli, Togay Amirahmadov, Özgün Akyüz, Dr. Nihan Koşku Perkgöz, Dr. Urartu Özgür Ş. Şeker, Dr. Pedro Ludwig Hernandez-Martinez, Dr. Olga Samarskaya. It is/has been a privilege working with all these people.

During my master's studies, I worked closely with the Dönüş Tuncel's Group. In addition to the many skills that I gained during my research with them, I also had great friends. Knowing all of them has been a great honor for me. I would like to thank Dr. Eun Ju Park, Zeynep Göksel Özsarp, Müge Artar and Vüsala Ibrahimova for their excellent friendship. I enjoyed every minute of it while working with them.

In addition to all these great people, I also would like to thank Dr. Stephen Hickey and Dr. Nikolay Gaponik for their hospitality while I was in Dresden.

At this point, I, of course, thank my family: My father and mother, for their supports and patience, and for many things that I cannot put into words. Also I owe many thanks to my brothers that are with me whenever I need them. I would also like to thank my aunt and her husband, who have turned Ankara to a bearable city for me.

I would also like to thank TUBITAK BIDEB for the financial support.

Table of Contents

List of Figures

List of Tables

Chapter 1

Introduction

Today traditional fossil based energy production undesirably leads to dramatic increase in CO_2 content of the atmosphere, which consequently adversely affects the climate [1]. To slow down this trend, scientists throughout the world continue working on energy efficiency in different fields of science [2,3]. One of those areas is the reduction and optimization of the energy consumed by the electrical devices, which can take a significant role in combatting climate change if targeted performance levels are realized.

Among various applications, lighting has an important place for potential energy saving as today ca. 20% of the global electrical energy consumption is used for the artificial lighting [4]. In the under-developed parts of the world, gas lamps are still used, which possess very low light quality and efficiency. As the regional economic power increases, the most widely used light sources become fluorescent lamps (and incandescent lamps in some places). However, these sources are not enough for high-efficiency.

Solid state lighting offers a huge potential in terms of energy efficiency. If the light emitting diodes (LED) achieve the targeted efficiencies, the energy consumed for lighting applications can be reduced by fifty percent [5]. According to a recent report published by the US Department of Energy, 133 TWh of electrical energy can be saved annually in the USA in case that general illumination sources are replaced entirely with LEDs [6]. However, to realize such a large-scale change of light sources, they need to be designed specifically

for the aimed applications so that high-quality white light can be obtained in addition to high-efficiency, requiring a reasonable production cost and capacity.

For high-quality lighting, the capability of the light sources to render the real colors of the illuminated objects is an important criterion. In addition to increasing the life quality, especially for indoor lighting, this property of light sources can be crucial for street lighting applications since good color rendering increases the perception of color contrast under low ambient lighting conditions, which consequently might help to save human life against the risk of life-threatening accidents. Moreover, a good light source should have a good spectral match between the emitted light spectrum and the human eye sensitivity function at the luminance levels of the specific applications. If this spectral match is not good enough, the emitted optical power by the device cannot be efficiently perceived by the human eye. Furthermore, a warm white shade is desirable especially for indoor lighting applications as it can otherwise affect the human biological clock.

Satisfying all of these high-quality lighting requirements simultaneously, in addition to high energy efficiency, requires careful spectral design and material choice. Conventional light sources such as incandescent and fluorescent lamps cannot fulfill these needs as their efficiencies are not high enough and/or tuning their spectra is not possible. Although power conversion efficiencies of white LEDs, in which phosphors are typically integrated as color convertors, are relatively good, their spectra cannot be controlled and tuned to the desired extent. As a result, they fail in satisfying the requirements for high-quality white light stated above. Spectral tuning can be achieved when individual LED chips emitting different color components are used together. However, this requires an individual green-emitting LED, which is low efficiency. Also, this multichip approach for spectrally tunable white light generation is far from being cost effective.

One of the candidate materials, which can be used for color conversion instead of conventional phosphors on blue (or UV) LED chips and allows spectral tuning, is the colloidal semiconductor quantum dots (QDs). Since their emission properties can be fine-tuned by controlling their sizes and monodispersity, using multiple color components with individual narrow emission bands around strategic wavelengths enables to obtain a white light satisfying the requirements aforementioned. Another class of materials, whose emission spectra can also be tuned, is the conjugated polymer nanoparticles. By crosslinking and building a core-shell type of nanoparticle structure, one can tune the photoluminescence spectra of these particles. As a result, spectral requirements for some specific applications can be satisfied using these nanoparticles as color convertors on LED chips emitting at shorter wavelengths.

This thesis presents the results of the thesis research work for obtaining efficient, high-quality and application specific white LED designs using colloidal quantum dots and conjugated polymer nanoparticles. It is organized as follows: Chapter 1 provides a general introduction and overview to the problems addressed in our research. In Chapter 2, the basic background regarding color science and photometry is given, which is useful for evaluating the quality of the generated light in a quantitative basis. Chapter 3 covers the optical properties of the materials used in this thesis work, i.e., quantum dots and polymer nanoparticles. Chapter 4 is dedicated to the white light generation methods using LEDs. Our studies on quantum dot integrated white LEDs for indoor lighting applications are explained in Chapter 5. The performance of quantum dot integrated white LEDs for outdoor applications is discussed in Chapter 6. Chapter 7 summarizes our work on white light generation using conjugated polymer nanoparticles via crosslinking. Finally, in Chapter 8 we summarize our conclusions of this thesis.

Chapter 2

Color Science and Photometry

To evaluate the quality of white light sources, one needs to have quantitative measures so that light sources can be classified accordingly. For this purpose, basic information on color science and photometry is essential. In this chapter, we review these points starting from the structure of a human eye. Then we continue with discussing the color matching functions and color spaces. Following these, two important color rendering metrics, i.e., color rendering index and color quality scale, are explained. Subsequently, we move to the photometry and start with the eye sensitivity functions for different vision regimes and continue with the definitions of some basic photometric quantities. Then we explain luminous efficacy of optical radiation and luminous efficiency of the light sources. Finally we close this chapter with the description of scotopic-to-photopic ratio (S/P ratio) and mesopic luminance.

2.1 The Structure of Human Eye

The eye is the organ through which we see our environment. Therefore, understanding its structure and working is essential for the purposes of high-quality light generation. It has an almost spherical shape with a diameter of ca. 24 mm [7]. The cornea is the layer of the eye where the light rays first enter (Figure 2.1). It is a transparent structure and contains no blood vessels. In its front part, it exhibits an additional curvature, whose radius of curvature is about 8 mm. Tears and mucus solutions help the eye to sustain its transparency. After cornea, the light rays pass through the so-called anterior chamber which is full of a transparent liquid known as aqueous humor controlling the pressure within the eyeball. As the interior pressure of the eye is greater than the atmospheric

pressure, the amount of this liquid is essential for protecting the shape of the eye. Following this liquid part, light rays come to the lens which is responsible for focusing the incoming rays on the retina. The position of the focus is controlled through the shape change of the lens by two muscles. These muscles pull or relax the lens when the eye focuses on a far or close object and the lens takes a flat or convex shape, respectively. After the lens, light rays travel within the vitreous body, which is filled by a jelly material, and fall on the retina. This part of the eye corresponds to the two-thirds of the volume of the eye.

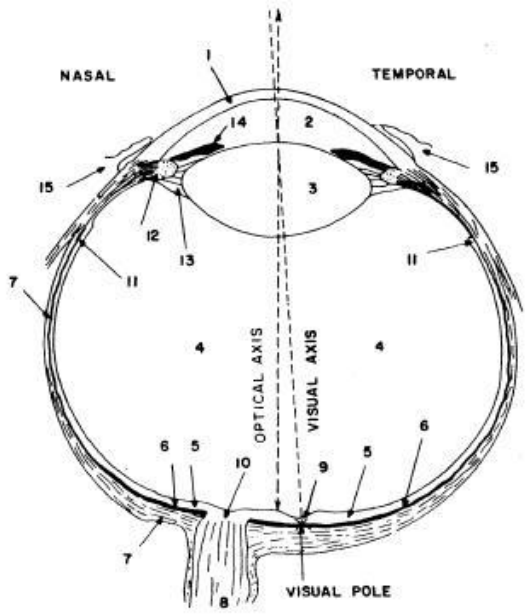

Figure 2.1 Structure of a human (right) eye. (1) cornea, (2) aqueous humor, (3) lens, (4)vitreous body, (5) retina, (6) choroid, (7) sclera, (8) optic nerves, (9) fovea, (10) optic disk, (11) front edge of retina, (12) ciliary muscle, (13) zonule fibers, (14) iris and (15) ocular conjunctiva [7].

The retina is the part of the eye where the most critical layers for vision are located and neurons and fibers are contained. According to Stell, the neurons constitute three main layers [8]. The first layer is the layer of photoreceptors; the second one is the layer of intermediate neurons. Finally, the third neural layer is the layer of ganglion cells. The light sensitive cells are called photoreceptors. There are two types of them: rods and cones. The retina is rich of rods, which are more sensitive to light compared to cones. Their sensitivity covers the whole

visible range without useful color differentiation; as a result, they cannot provide color information to the brain. On the other hand; cones have three types, each having a different wavelength range of sensitivity corresponding to blue, green and red colors [9]. As Figure 2.2 illustrates, the photoreceptors are named considering their shapes. Figure 2.3 shows the relative sensitivities of rods and red, green and blue photoreceptors with respect to optical wavelength [9].

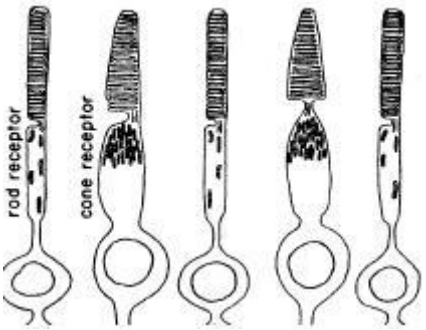

Figure 2.2 Rod and cone receptors in the eye [10].

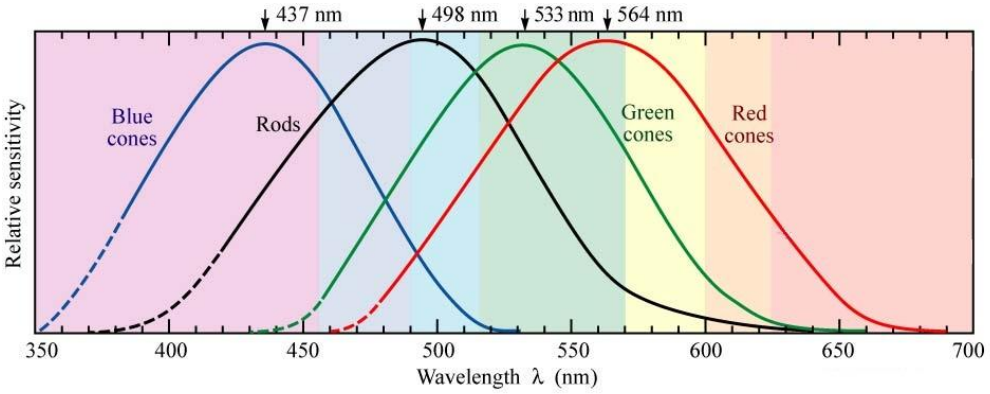

Figure 2.3 Normalized spectral sensitivities of rods and cones (red, green and blue) [9].

In addition to their spectral sensitivities, the photoreceptor activity depends on the ambient lighting levels. At high light levels, cones are more active and they dominate the vision whereas rods saturate and do not have any significant contribution to the vision. The vision at this light level is called the photopic vision. On the other hand, cones are not sensitive enough at lower light levels while rods dominate the vision. This is why we cannot distinguish different colors in the dark. This vision regime is called scotopic. There is another vision

regime where rods and cones are both active and contribute to the vision simultaneously. This regime is called the mesopic vision whose limits and significance will be discussed in the further sections of this chapter.

2.2 Color Matching Functions and Color Spaces

To engineer light sources, one needs to define colors in a mathematical sense. However, color perception of every individual slightly varies; therefore, such a definition has to be made using a statistical approach. The International Commission for Illumination (Commission Internationale de l'Eclairage, CIE) has used such an approach and published a standardized method for the definition of color [11]. CIE utilized three color matching functions: x, y and z, whose spectral distributions are given in Figure 2.4.

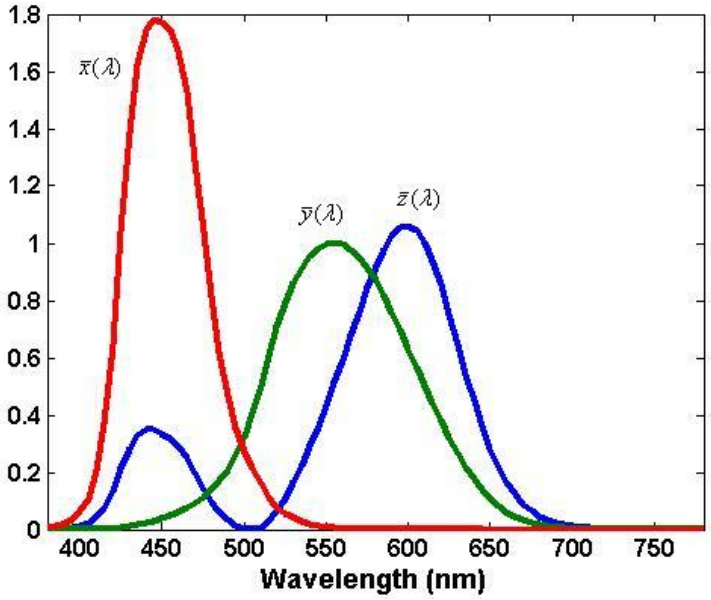

Figure 2.4 Color matching functions as defined in CIE 1931 [11].

The method proposed by CIE makes use of these color matching functions and the chromaticity diagram. The tristimulus values, X, Y and Z, are given in Equations (2.1) – (2.3) for a spectral power distribution of s(λ).

$$X = \int_{\lambda} s(\lambda)\bar{x}(\lambda)d\lambda \qquad \textbf{(2.1)}$$

$$Y = \int_{\lambda} s(\lambda)\bar{y}(\lambda)d\lambda \qquad \textbf{(2.2)}$$

$$Z = \int_{\lambda} s(\lambda)\bar{z}(\lambda)d\lambda \qquad \textbf{(2.3)}$$

The chromaticity coordinates are calculated as in Equations (2.4) – (2.7). The chromaticity diagram, which is created by using the mapping methodology described in Equations (2.1) – (2.6), is given in Figure 2.5. Since one of the three coordinates is dependent on the other two, a two dimensional color space is enough without having any information loss.

$$x = \frac{X}{X+Y+Z} \qquad \textbf{(2.4)}$$

$$y = \frac{Y}{X+Y+Z} \qquad \textbf{(2.5)}$$

$$z = \frac{Z}{X+Y+Z} = 1-x-y \qquad \textbf{(2.6)}$$

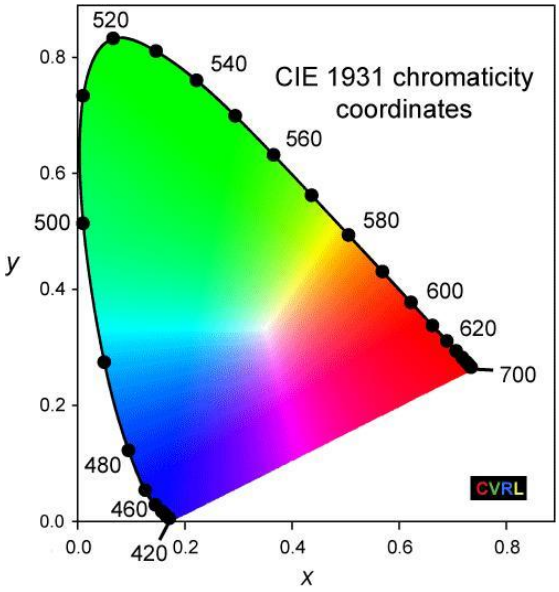

Figure 2.5 CIE 1931 (x,y) chromaticity diagram [12].

Although CIE 1931 is the most widely used chromaticity diagram, it has some important weaknesses, which was later improved by defining new color

spaces. One of the important drawbacks of CIE 1931 is that the geometric difference between colors does not correspond to the same color differences. To fix this problem, CIE introduced new chromaticity diagrams in 1960 and 1976, which are called CIE 1960 and 1976 chromaticity diagrams, respectively. These diagrams are also called (u,v) and (u',v') chromaticity diagrams [13,14]. CIE 1976 chromaticity diagram is given in Figure 2.6.

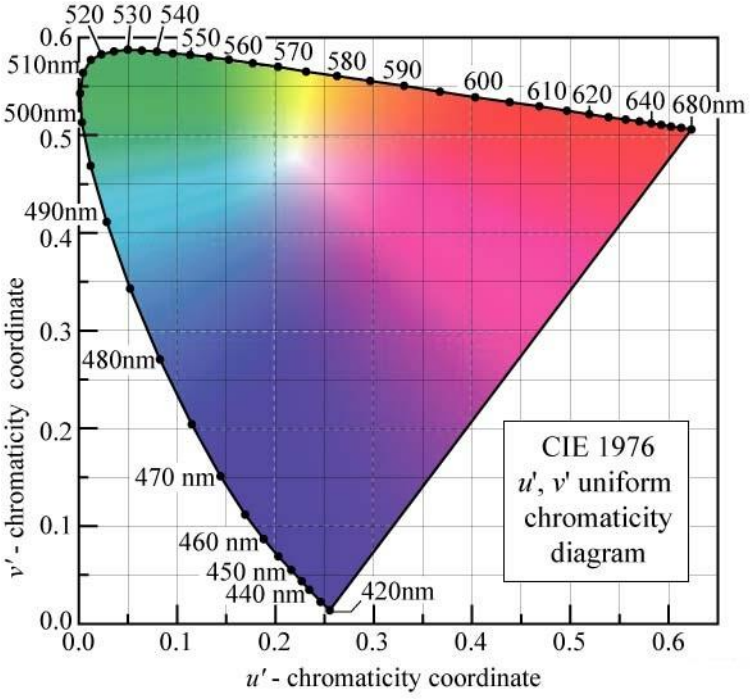

Figure 2.6 CIE 1976 chromaticity diagram [9].

Calculations of (u,v) and (u',v') chromaticity coordinates are given in Equations (2.7) – (2.9).

$$u = u' = \frac{4X}{X + 15Y + 3Z} \qquad \textbf{(2.7)}$$

$$v = \frac{6Y}{X + 15Y + 3Z} \qquad \textbf{(2.8)}$$

$$v' = \frac{9Y}{X + 15Y + 3Z} \qquad \textbf{(2.9)}$$

Another uniform color space is the CIE 1976 ($L^*a^*b^*$) chromaticity diagram [14]. The corresponding equations required for color mapping are given by Equations (2.10) – (2.12) [7].

$$L^* = 116(Y / Y_n)^{1/3} - 16 \quad \textbf{(2.10)}$$

$$a^* = 500\left[\left(\frac{X}{X_n}\right)^{1/3} - \left(\frac{Y}{Y_n}\right)^{1/3}\right] \quad \textbf{(2.11)}$$

$$b^* = 200\left[\left(\frac{X}{X_n}\right)^{1/3} - \left(\frac{Z}{Z_n}\right)^{1/3}\right] \quad \textbf{(2.12)}$$

These formulas are valid as long as X/X_n, Y/Y_n and Z/Z_n are larger than 0.01. Otherwise the calculations should be carried out using Equations (2.13) – (2.17).

$$L_m^* = 903.3\frac{Y}{Y_n} \quad \textbf{(2.13)}$$

$$a_m^* = 500\left[f\left(\frac{X}{X_n}\right) - f\left(\frac{Y}{Y_n}\right)\right] \quad \textbf{(2.14)}$$

$$b_m^* = 200\left[f\left(\frac{X}{X_n}\right) - f\left(\frac{Z}{Z_n}\right)\right] \quad \textbf{(2.15)}$$

where

$$f\left(\frac{K}{K_n}\right) = \left(\frac{K}{K_n}\right)^{1/3} \quad for\ \frac{K}{K_n} > 0.008856 \quad \textbf{(2.16)}$$

$$f\left(\frac{K}{K_n}\right) = 7.787\left(\frac{K}{K_n}\right) + \left(\frac{16}{K_n}\right) for\ \frac{K}{116} \le 0.008856 \quad \textbf{(2.17)}$$

for K is X, Y or Z. X_n, Y_n and Z_n are called the nominally white object color stimulus, and they are calculated by making use of the spectral power distributions of CIE standard illuminants like A and D_{65} and Equations (2.1) – (2.3).

2.3 Color Rendering Index and Color Quality Scale

A good white light source has to render the real colors of the objects that it illuminates. It is very critical especially for the indoor lighting applications; however, for outdoor applications, it also helps to increase the safety because good color rendering provides better color contrast and consequently, better vision under low ambient lighting.

The color rendering capability of the illuminants is calculated by several methods. In this thesis, we explain the most widely used two metrics i.e.: the color rendering index (CRI) and the color quality scale (CQS), which is developed as a similar approach to CRI.

The color rendering index (CRI) is developed by CIE in 1971 [15] and updated to its current form in 1995 [16]. It basically tests the color rendering capability of the test light source with respect to a reference light source, which is accepted to possess perfect color rendition. CRI makes use of fourteen test color samples suggested by CIE. Based on the reflection of the test light source and the reference light source from these samples, color differences are calculated for each test sample. Finally, from these color differences a color rendering index value specific for each sample is obtained. The first eight of these samples are used for determining the general color rendering index. The remaining six define the special color rendering indices. The best color rendition is given as 100, whereas the worst rendition is denoted by a CRI of -100.

Before explaining the calculation of CRI, it is helpful to clarify the notation. The subscript "*ref*" stands for the reference light source, which is in general a blackbody radiator. The subscript "*ref,i*" denotes the reflected color from the i^{th}

test sample illuminated by the reference light source. The subscript "*test*" indicates for the light source under the test whereas "*test,i*" is the reflection of the test light source from the i^{th} test samples.

The calculation starts with the transformation of (u,v) coordinates to (c,d) coordinates given by Equations (2.18) and (2.19).

$$c = (4 - u - 10v) / v \qquad \textbf{(2.18)}$$

$$d = (1.708v + 0.404 - 1.481u) / v \qquad \textbf{(2.19)}$$

Then ($u_{test,i}^{**}$,$v_{test,i}^{**}$) are calculated by Equations (2.20) and (2.21).

$$u_{test,i}^{**} = \frac{10.872 + 0.404\frac{c_{ref}}{c_{test}}c_{test,i} - 4\frac{d_{ref}}{d_{test}}d_{test,i}}{16.518 + 1.481\frac{c_{ref}}{c_{test}}c_{test,i} - \frac{d_{ref}}{d_{test}}d_{test,i}} \qquad \textbf{(2.20)}$$

$$v_{test,i}^{**} = \frac{5.520}{16.518 + 1.481\frac{c_{ref}}{c_{test}}c_{test,i} - \frac{d_{ref}}{d_{test}}d_{test,i}} \qquad \textbf{(2.21)}$$

The calculation of (u_{test}^{**},v_{test}^{**}) is given in Equations (2.22) and (2.23).

$$u_{test}^{**} = \frac{10.872 + 0.404c_{ref} - 4d_{ref}}{16.518 + 1.481c_{ref} - d_{ref}} \qquad \textbf{(2.22)}$$

$$v_{test}^{**} = \frac{5.520}{16.518 + 1.481c_{ref} - d_{ref}} \qquad \textbf{(2.23)}$$

For the calculation of color shift, we need ΔL^{**}, Δu^{**} and Δv^{**} (Equations (2.24) – (2.27)).

$$\Delta L^{**} = \left[25\ Y_{ref,i}^{\ 1/3} - 17\right] - \left[25\ Y_{test,i}^{\ 1/3} - 17\right] = L_{ref,i}^{**} - L_{test,i}^{**} \qquad \textbf{(2.24)}$$

$$\Delta u^{**} = 13L_{ref,i}^{**}(u_{ref,i} - u_{ref}) - 13L_{test,i}^{**}(u_{test,i}^{**} - u_{test}^{**}) \qquad \textbf{(2.25)}$$

$$\Delta v^{**} = 13L_{ref,i}^{**}(v_{ref,i} - v_{ref}) - 13L_{test,i}^{**}(v_{test,i}^{**} - v_{test}^{**}) \qquad \textbf{(2.26)}$$

Following these, the color difference is calculated as in Equation (2.27).

$$\Delta E_i^{**} = \sqrt{(\Delta L^{**})^2 + (\Delta u^{**})^2 + (\Delta v^{**})^2} \qquad \textbf{(2.27)}$$

After obtaining the color difference, individual color rendering indices of each test color sample can be obtained using Equation (2.28).

$$CRI_i = 100 - 4.6\Delta E_i^* \qquad \textbf{(2.28)}$$

Finally, the general color rendering index is obtained by taking the average of the first eight test color samples (Equation 2.29).

$$CRI = \frac{1}{8}\sum_{i=1}^{8} CRI_i \qquad \textbf{(2.29)}$$

Although CRI is still the most frequently used metric for color rendition, it suffers from some weaknesses that need to be overcome [17]. One of these problems is the uniform color space used in CRI, which is not recommended by CIE anymore. Another important issue regarding CRI is that it assumes perfect color rendering of blackbody radiators and reference sources even at very low and high correlated color temperatures (CCT, which will be explained in the next section). However, this is not always correct. Furthermore, CRI does not use any test color sample, which is highly saturated. As a result, it does not provide correct color rendering information of saturated colors although the results are accurate for samples having desaturated colors. On top of these, CRI makes use of the arithmetic mean of color rendering indices of each test color sample, which means that a poor rendering for one of the samples can be compensated.

Considering these problems of CRI, Davis and Ohno have developed a new metric for color rendition evaluation of light sources called color quality scale (CQS) [17]. It uses the same reference light sources as in CRI, but the test color samples are changed. Instead of eight unsaturated test color samples, CQS employs fifteen commercially available Munsell samples, all having highly saturated colors. Since a light source rendering saturated colors well succeeds a good rendition of unsaturated colors, this metric provides more healthy information of color rendering. This is especially useful for light emitting diodes, which are fabricated using narrow-band emitting material systems and structures. As it is done in the calculation of CRI, a chromatic adaptation

transform is necessary in CQS. However, CQS utilizes a modern transform, CMCCAT2000 [18]. Another important improvement of CQS compared to CRI is the choice of uniform color space. In CQS, CIE $L^*a^*b^*$ is preferred. The color difference between the reflections of the test samples illuminated by the reference and test light source is expressed in Equation (2.30).

$$\Delta E^*_{ab,i} = \sqrt{(\Delta L^*_i)^2 + (\Delta a^*_i)^2 + (\Delta b^*_i)^2} \qquad \textbf{(2.30)}$$

where

$$\Delta L^*_i = L^*_{test,i} - L^*_{ref,i} \qquad \textbf{(2.31)}$$

$$\Delta a^*_i = a^*_{test,i} - a^*_{ref,i} \qquad \textbf{(2.32)}$$

$$\Delta b^*_i = b^*_{test,i} - b^*_{ref,i} \qquad \textbf{(2.33)}$$

The chroma difference is given by Equation (2.34).

$$\Delta C^*_{ab,i} = C^*_{ab,test,i} - C^*_{ab,ref,i} \qquad \textbf{(2.34)}$$

where

$$C^*_{ref,i} = \sqrt{(a^*_{ref,i})^2 + (b^*_{ref,i})^2} \qquad \textbf{(2.35)}$$

$$C^*_{test,i} = \sqrt{(a^*_{test,i})^2 + (b^*_{test,i})^2} \qquad \textbf{(2.36)}$$

In addition to the color difference in Equation (2.30), a saturation factor is introduced in CQS so that the effect of increasing the object chroma under the test illuminant with respect to reference source is neutralized. The corrected color difference then becomes as given in Equation (2.37).

$$\Delta E^*_{ab,sat,i} = \begin{cases} \Delta E^*_{ab,i}, if\ \Delta C^*_{ab,i} \le 0 \\ \sqrt{(\Delta E^*_{ab,i})^2 - (\Delta C^*_{ab,i})^2}, otherwise \end{cases} \qquad \textbf{(2.37)}$$

One of the most important improvements of CQS compared to CRI is in the calculation of the final color rendering performance. As opposed to CRI, CQS takes root-mean-squares (rms) of individual corrected color differences, so that poor rendition of any test color sample has a more significant effect on the final value. The calculation of rms-color difference and rms-averaged CQS is given in Equations (2.38) and (2.39).

$$\Delta E_{rms} = \sqrt{\frac{1}{15}\sum_{i=1}^{15}(\Delta E^*_{ab,sat,i})^2} \qquad \textbf{(2.38)}$$

$$Q_{a,rms} = 100 - 3.1\Delta E_{rms} \qquad \textbf{(2.39)}$$

An additional difference of CQS compared to CRI is its scale. Since having a CRI less than zero, which denotes a poor color rendition, can be misleading, CQS is brought to the scale of 0–100. This scaling is undertaken using Equation (2.40).

$$CQS_{0-100} = 10\ln\{\exp(\frac{Q_{a,rms}}{10}) + 1\} \qquad \textbf{(2.40)}$$

Finally, the correction for low CCTs is introduced (in Equations (2.41) and (2.42)) and the final value of CQS is determined using Equation (2.43).

For CCT < 3500 K,

$$M_{CCT} = CCT^3(9.2672\times10^{-11}) - CCT^2(8.3959\times10^{-7}) + CCT(0.00255) - 1.612 \qquad \textbf{(2.41)}$$

For CCT ≥ 3500 K,

$$M_{CCT} = 1 \qquad \textbf{(2.42)}$$

$$CQS = M_{CCT}CQS_{0-100} \qquad \textbf{(2.43)}$$

2.4 Correlated Color Temperature

The correlated color temperature (CCT) is one of the most widely used metrics for characterizing white light sources. Before defining CCT, it is more instructive first to explain the color temperature. If the chromaticity coordinates of the white light source fall onto the Planckian locus (chromaticity coordinates of blackbody radiators at different temperatures), then the temperature of the blackbody radiator having the same chromaticity points as the white light source is called the color temperature. In case that the chromaticity coordinates of the light source under test is not on the Planckian locus, then the temperature of the blackbody radiator, whose (u',v') chromaticity coordinates are closest to the light

source under the test source, is called the correlated color temperature. The Planckian locus is given in Figure 2.7.

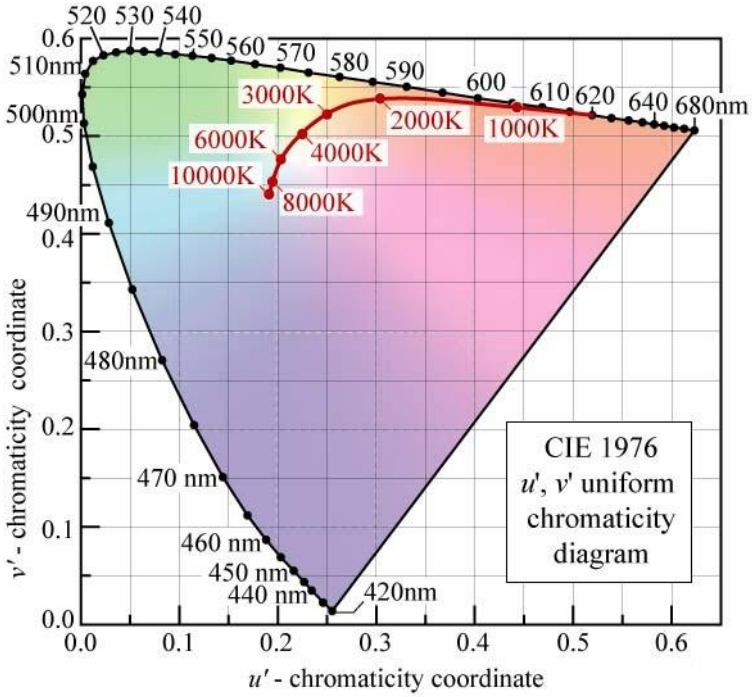

Figure 2.7 Planckian locus on CIE 1976 (u',v') chromaticity diagram [9].

White light sources having high CCTs have a bluish shade, whereas a reddish shade corresponds to lower CCTs. Therefore, cold (or cool) white light has a higher CCT and warm white sources have lower CCTs, which might look confusing at the first sight since the use of the terminology is opposite to the common usage of temperature. An incandescent light bulb has a CCT below 3000 K, the fluorescent tubes have varying CCTs between 3000 to 6500 K whereas the CCT of the sun is close to 6000 K [9]. For indoor lighting, warm white light sources are preferred as a cool white has a high bluish content which might cause shifts in the biological clock [19].

2.5 Eye Sensitivity Functions

While evaluating the quality of the white light sources, it is of significant importance that the spectra of the illuminants match the sensitivity of the human eye as well as possible. A light source would that radiates at wavelengths not sensible by the eye cannot contribute to the vision even if it has a high power conversion efficiency or high optical power.

Since the photoreceptors contributing to the vision are different at different ambient light levels, the sensitivity of the eye changes accordingly. Rod photoreceptors are responsible for the scotopic vision, which is the dark-adapted vision [9]. Its sensitivity takes its maximum at 507 nm. On the other hand, cones provide the photon adapted vision and start to work above some luminance levels. The vision at these light levels is called the photopic vision (photon-adapted vision). The sensitivity of the cones makes its peak at 555 nm. The corresponding eye sensitivity functions for scotopic [20] and photopic [11] light levels are given in Figure 2.8.

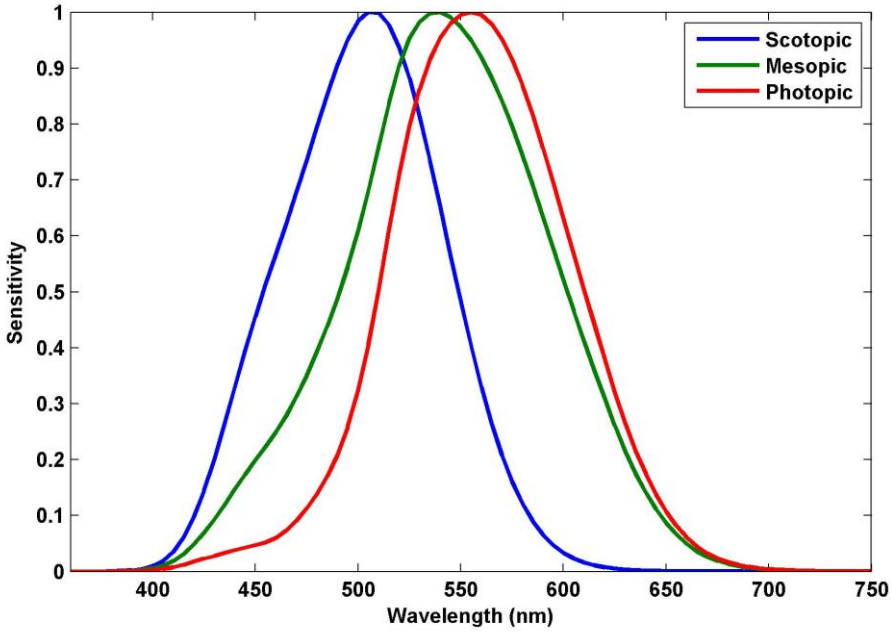

Figure 2.8 The eye sensitivity function at different vision regimes: photopic (red), mesopic (green, at a luminance of 0.5 cd/m^2) and scotopic eye sensitivity functions.

Before explaining the mesopic vision levels, it is necessary to define the luminance, which we will explain again in the next section. The luminance of a light source is calculated as in Equation (2.44).

$$L = 683\frac{lm}{W_{opt}}\int P(\lambda)V(\lambda)d\lambda \qquad \textbf{(2.44)}$$

where P(λ) and V(λ) are the spectral radiance (power per unit area per solid angle) and the photopic eye sensitivity function, respectively.

In the mesopic levels both photoreceptors are active. As a result, the sensitivity of the eye changes according to the level of contribution of rods and cones. These changes are well known for a long time ago, however, the exact limits of photopic and scotopic regimes and the eye sensitivity function at mesopic levels have been a subject of discussion. For example, Osram Sylvania defines the luminance limits of photopic and scotopic vision as 0.003 and 3 cd/m^2, respectively [21]. According to Johnson [22] and LeGrand [23] photopic vision starts at the luminance of 5 cd/m^2, whereas Kokoschka pushes this limit further to 10 cd/m^2 [24]. As IESNA (Illuminating Engineering Society of North America) puts these limits to around 0.01 cd/m^2 and 3 cd/m^2 [25], CIE 1978 claims the scotopic vision to start below 0.001 cd/ m^2 [26]. According to unified system of photometry (USP) developed by Rea, photopic vision starts above 0.6 cd/m^2 and scotopic vision starts below 0.001 cd/m^2 [27]. Another recent system for mesopic photometry is developed by MOVE consortium; according to this work, mesopic vision lies between the luminances of 0.01 cd/m^2 and 10 cd/m^2 [28,29]. In 2010, CIE recommended a system of photometry (CIE 191:2010), which is based on USP and MOVE systems [30]. According to this most recent report, mesopic regime is defined between the luminance levels of 0.005 cd/m^2 and 5 cd/m^2. In this report, the eye sensitivity function is also defined and calculated as given in Equations (2.45) and (2.46).

$$M(m)V_{mes}(\lambda) = mV(\lambda) + (1-m)V'(\lambda) \qquad \textbf{(2.45)}$$

$$L_{mes} = 683 / V_{mes}(\lambda_0)\int V_{mes}(\lambda)P(\lambda)d\lambda \qquad \textbf{(2.46)}$$

where $V(\lambda)$, $V'(\lambda)$ and $V_{mes}(\lambda)$ are the photopic, scotopic, and mesopic eye sensitivity functions, respectively; $P(\lambda)$ is the spectral radiance, $M(m)$ is a normalization constant such that $V_{mes}(\lambda)$ has the maximum value of 1, λ_0 is 555 nm, L_{mes} is the mesopic luminance, and m is a coefficient depending on visual adaptation conditions. Further details on the calculation of mesopic eye sensitivity function can be found in Ref. 30. As an exemplary case, the eye sensitivity function at a luminance of 0.5 cd/m^2 is given in Figure 2.8.

2.6 Basic Radiometric and Photometric Measures

The light sources are also sources of electromagnetic radiation. From this perspective, their performances can be evaluated with respect to their electromagnetic properties characterized by the radiometric measures. In addition to this, the light sources, especially white light sources, are subject to the sensitivity of the human eye. Therefore, these sources have to be evaluated by taking the response of the human eye into account. Scaling the radiometric units with the eye sensitivity function remedies this problem and introduces the photometric quantities.

One of the most frequently used radiometric quantities is the optical power. In the lighting community, radiant flux is alternatively used instead of optical power [9]. The photometric version of the optical power is the luminous flux and calculated using spectral radiant flux $P_\phi(\lambda)$ and eye sensitivity function $V(\lambda)$ as in Equation (2.47). The unit of luminous flux is lumen (lm).

$$\phi = 683 \frac{lm}{W_{opt}} \int P_\phi(\lambda) V(\lambda) d\lambda \qquad \textbf{(2.47)}$$

Given the spectral radiant intensity $P_{LI}(\lambda)$, i.e., the optical power per unit solid angle at varying wavelengths, the luminous intensity becomes as in Equation (2.48). The luminous intensity is given in units of lm/sr or equivalently in candelas (cd).

$$LI = 683\frac{lm}{W_{opt}}\int P_{LI}(\lambda)V(\lambda)d\lambda \qquad \textbf{(2.48)}$$

The irradiance is the optical power per unit area, its correspondent in photometry is the illuminance which has the units of lm/m^2. Given the spectral radiance (in units of $W_{opt}m^{-2}nm^{-1}$) $P_{Il}(\lambda)$, the luminance is expressed as in Equation (2.49). Its unit is lm/m^2, or equivalently lux.

$$Il = 683\frac{lm}{W_{opt}}\int P_{Il}(\lambda)V(\lambda)d\lambda \qquad \textbf{(2.49)}$$

Finally, the radiance is the radiometric quantity denoting the optical power per solid angle per unit area and has the units of $W_{opt}sr^{-1}m^{-2}$. Given the spectral radiance $P_L(\lambda)$, the luminance is calculated using Equation (2.50). Its unit is $lm/(m^2sr)$, or equivalently cd/m^2.

$$L = 683\frac{lm}{W_{opt}}\int P_{L}(\lambda)V(\lambda)d\lambda \qquad \textbf{(2.50)}$$

At this point, it is worth mentioning that the photometric quantities defined in this section are based on the photopic eye sensitivity function. However, photometric measures for mesopic and scotopic eye sensitivity functions may also be defined in the same way, but in those cases mentioning the type of the eye sensitivity function is necessary to avoid confusions. Also, one has to pay attention to equate the value of the corresponding eye sensitivity function to 1 at 555 nm. As a result, the factor 683 lm/W_{opt} changes with respect to the vision regime. For scotopic regime, this factor takes the value of 1699 lm/W_{opt}, whereas for mesopic vision regime this value varies as the photopic luminance changes.

To evaluate the quality of the white light sources, there are two equally important efficiency measures that are strongly correlated to the sensitivity of the eye. One of them denotes the efficiency of the radiated light for human perception per radiated optical power. It is called the luminous efficacy of optical radiation (LER). Given the spectral power distribution of $P(\lambda)$ and

photopic eye sensitivity function $V(\lambda)$, LER is calculated using Equation (2.51) and has the units of lm/W_{opt}.

$$LER = \frac{683 \frac{lm}{W_{opt}} \int P(\lambda) V(\lambda) d\lambda}{\int P(\lambda) d\lambda} \qquad \textbf{(2.51)}$$

The second important efficiency measure calculates the efficiency of the radiated light as perceived by the human eye per supplied electrical power, P_{elect}. This performance criterion of light sources is called the luminous efficiency (LE). It is expressed in units of lm/W_{elect} and calculated as given in Equation (2.52).

$$LE = \frac{683 \frac{lm}{W_{opt}} \int P(\lambda) V(\lambda) d\lambda}{P_{elect}} \qquad \textbf{(2.52)}$$

At this point, it is instructive to mention that LE is related to LER through the power conversion efficiency (PCE). The relation is given by Equation (2.53).

$$LE = LER \times \frac{\int P(\lambda) d\lambda}{P_{elec}} = LER \times PCE \qquad \textbf{(2.53)}$$

Another performance criterion is the ratio of scotopic-to-photopic efficiencies (S/P). If this ratio is high, then the vision in the scotopic and mesopic regimes is stronger. In addition, the brightness perception is higher in the case that S/P is high [31]. This quantity is basically the ratio of luminous fluxes in scotopic and photopic vision regimes (Equation (2.54)).

$$S/P = \frac{1699 \frac{lm}{W_{opt}} \int P(\lambda) V'(\lambda) d\lambda}{683 \frac{lm}{W_{opt}} \int P(\lambda) V(\lambda) d\lambda} \qquad \textbf{(2.54)}$$

Chapter 3

Materials: Colloidal Quantum Dots and Polymer Nanoparticles

To satisfy the photometric and colorimetric high performance for general lighting applications, a careful spectral design of the source is necessary. For this purpose, materials enabling spectral tuning are required. Within the framework of this thesis we concentrate on two different materials. These are the colloidal semiconductor quantum dots (QDs) and conjugated polymer nanoparticles (CNPs). For QDs, spectral tuning can be achieved by controlling the size and size-dispersity of QDs together with the choice of QD combinations used in the color conversion film. On the other hand, the spectra generated using CNPs can be tuned via crosslinking the nanoparticles under ultraviolet (UV) illumination. In this chapter, we review material properties of these color convertors. The first section is devoted to colloidal quantum dots while the second one covers the conjugated polymer nanoparticles.

3.1 Colloidal Quantum Dots

In recent decades, optoelectronic devices, which are based on the semiconductor materials, have already revolutionized our lifestyles. As new studies concentrate on manipulations of the materials at the nanometer scale, new structures employing quantum mechanical effects start to be developed. Colloidal semiconductor QDs are one of these structures.

Since the bandgap of these QDs can be tuned within or near the visible spectral range, semiconductor QDs have important place in photonics.

Additionally, the optical characteristics of these materials are dependent on their size. Therefore, controlling their size allows for the tuning of their optical properties. As a result, new type of lasers, light emitting diodes, solar cells, and other new optoelectronic devices can be developed.

3.1.1 Physical Picture of Quantum Dots

As the size of the materials gets smaller and smaller, the material properties cannot be explained by classical mechanics; instead, the governing mechanisms rely on the principles of quantum physics. For the semiconductor QDs, the same physical realities apply. In a QD, electrons and holes are confined in three dimensions, typically within a range of 2-10 nm [32]. This distance is also the typical extension of electrons and holes in a semiconductor material.

The quantum-confinement effects are size-dependent. To create the confinement, the QDs are surrounded by a structure whose energy bandgap is higher. Such potential barrier structures can be obtained by using different architectures. One of the most interesting styles of QDs is the colloidal ones, which are prepared via wet chemical techniques (Figure 3.1(a)) [33]. The potential barrier is created by the surrounding medium, which in general constitutes of the organic molecules called the ligands. The quantum confinement effects, which depend on the size of the QD, are controlled with the adjustment of temperature, growth time and reactants. Another common method for the creation of epitaxial QDs, which are different than the colloidal quantum dots used in this thesis, is the usage of epitaxial growth techniques. In this method, the island of an energetically small material is surrounded by a matrix with a wider energy bandgap. As an example for this kind of a structure is shown in Figure 3.1(b).

In the bulk material case, the Bohr radius of the excitons becomes in the order of a few nanometers for II-VI semiconductors [34]. As the size of the particle

gets closer to the Bohr radius, the wavefunctions start to get confined tightly within the QDs.

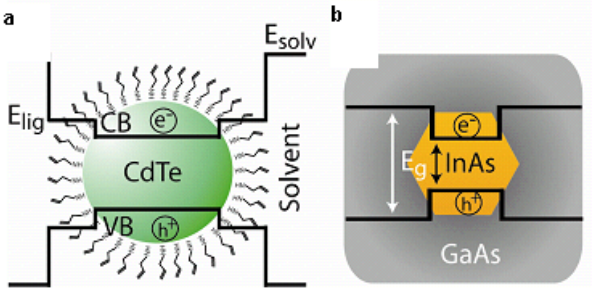

Figure 3.1 Semiconductor QDs: (a) colloidal semiconductor CdTe QDs in dispersion and (b) epitaxially grown InAs QDs within a GaAs matrix which has a larger bandgap [32].

To understand the quantum mechanical phenomena within QDs, the easiest way is to start with the Schrödinger Equation (Equation (3.1)).

$$-\frac{\hbar}{2m}\nabla^2\Psi + V(r)\Psi = E\Psi \qquad \textbf{(3.1)}$$

For the case of spherically symmetric potential, the solution of the Schrödinger Equation can be written as Equation (3.2).

$$\Psi(r,\theta,\phi) = R_{n,l}(r)Y_{l,m}(\theta,\phi) \qquad \textbf{(3.2)}$$

where *R(r)* and *Y(θ,ϕ)* are radial and angular wavefunctions, respectively. *n* stands for the principal quantum number whereas *l* and *m* are the orbital and angular momentum numbers, respectively.

In the case of infinite potential well, energy eigenvalues are given by Equation (3.3) [35]:

$$E_{n,l} = \frac{\hbar^2 \chi_{n,l}^2}{2ma^2} \qquad \textbf{(3.3)}$$

where *a* is the width of the potential well described by Equation (3.4).

$$V(r) = \begin{cases} 0, & for \quad r \le a \\ \infty, & for \quad r > a \end{cases} \qquad \textbf{(3.4)}$$

In Equation (3.3), χ_{nl} stands for the roots of the Bessel function. However, these solutions represent the case of a free electron with mass m. To have a better physical picture of QDs, the presence of electrons and holes has to be taken into account. These effects are modeled by Brus [36], and Franceschetti and Zunger [37]. According to these models, the expression of optical gap ($E_{n,l}^{opt}$) is given by Equation (3.5) [33]. In this equation, E_g stands for the bandgap, r is the radius of the quantum dot, m_e^* and m_h^* are the effective electron and hole masses, respectively. $\chi_{nl,e}$ and $\chi_{nl,h}$ denote the roots of the spherical Bessel functions having the quantum numbers of n and l. Finally, e stands for the electron charge whereas ε_{in} is the static dielectric constant inside the QD. Note that Equation (3.5) takes into account the Coulomb interaction between electrons and holes.

$$E_{n,l}^{opt} = E_g + \frac{\hbar^2}{2r^2}\left(\frac{\chi_{nl,e}^2}{m_e^*} + \frac{\chi_{nl,h}^2}{m_h^*}\right) - \frac{1.8e^2}{\varepsilon_{in} r} \qquad \textbf{(3.5)}$$

Although this equation does not give the optical transition energies of QDs accurately, it still provides the intuitive information regarding its emission properties. Further information can also be found in Ref. 35-37.

3.1.2 Synthesis of Quantum Dots

The synthesis of colloidal QDs are carried out basically in two different types of solutions. These are non-polar organic solutions and water (polar). In this part of the thesis, both of these approaches will be reviewed.

The synthesis of QDs in organic solvents basically involves the decomposition of molecular precursors [38]. In this approach, the precursors are injected into a hot solvent. As a result, atomic species, which will build up the quantum dot, are freed in a very short time. This leads to the oversaturation of the monomers required for the QD growth. Therefore, the growth of QDs is highly probable in such a medium. The temperature and the composition of the

solvent are two of the most effective parameters for the growth and the shape of the QDs [39,40]. For example, CdTe QDs in general constitute of a hexagonal wurtzite phase when synthesized in organic solvents [41]. However, by controlling the reaction conditions one can obtain structures in the cubic zinc blend phase [42]. The temperature of the solvent is important because it enables the decomposition into monomers within the solution and triggers the growth of QDs. In addition of the temperature, the solvent choice is also of great importance. In general, the solvent has two main functions [38]: First of all, the solvent disolves and disperses the QDs and the reactants taking part in the growth process. Second, the reaction speed is controlled by the solvent. In order to control the growth process, solvent molecules have to bind and unbind dynamically on the surface of the growing crystalline structure. Once a molecule leaves the surface of the QD, new atomic species, i.e., monomers, can bind to the crystal and the growth of the crystal starts. Because of these functions, the organic molecules binding on the surface of QDs are also called “surfactants” or “surface ligands”. As another function of the surfactants, it should be mentioned that they prevent QDs to get agglomerated by providing repulsion between QDs [43]. In general, a surfactant has a non-polar domain, often a long alkyl chain, and a polar head group. The shape of the non-polar group and the binding strength of the polar group are effective in the crystal growth. The non-polar tail is responsible for the diffusion properties whereas the polar domain determines the binding efficiency. Starting with the work of Murray et al. [41], tri-n-octylphosphine oxide (TOPO) and tri-n-octylphosphine (TOP) are commonly used surfactants. In addition different amines and carboxylic acids can be incorporated as surface ligands [44-46].

In the synthesis at least one of the species constituting QDs should be in liquid phase. Using a precursor, the growth can be started by quick injection. As a result, a fast nucleation occurs at high temperatures. For the growth of II-VI colloidal QDs, the elemental group II atoms are introduced in the mixture of TOP or tri-n-butylphosphine (TBP). When this mixture is heated at high

temperatures (around 300 °C), calcogen ions (for example Cd-ions) start to bind to the surfactant that are either phosphonic acids like dodecyl-, tetradecyl-, or octadecyl-phosphonic acids [44,47,48] or oleic acid [47,49]. The occurrence of this reaction is realized upon the observation of a steam and color change in the solution. After the injection of the group VI precursor, the formation of QDs starts to take place. The reaction is very fast in the beginning, but it slows down later over time. The nucleation and growth occurs after rapid injection of the solvents by increasing the precursor concentration above the nucleation threshold [43]. As a result, obtaining very small QDs emitting at shorter wavelengths is difficult. Obtaining larger QDs, which emit at longer wavelengths, requires a longer time. Some of the mostly synthesized QDs are CdS, CdSe, CdTe, ZnS, ZnSe, ZnTe and HgTe [43]. As an example of the synthesis procedure, the synthesis of CdSe QDs are given below based on the work of Yu et al. [50].

The required chemicals for the synthesis are oleic acid (OA: $CH_3(CH_2)_7CH=CH(CH_2)_7COOH$); tri-n-octylphosphine oxide (TOPO: $[CH_3(CH_2)_7]_3PO$); tri-n-octylphosphine (TOP: $[CH_3(CH_2)_7]_3P$); hexadecylamine (HDA: $CH_3(CH_2)_{15}NH_2$); octadecene (ODE: $C_{18}H_{36}$); selenium powder (Se); cadmium oxide (CdO); toluene ($C_6H_5CH_3$); methanol (MeOH: CH_3OH); acetone ($OC(CH_3)_2$); and chloroform ($HCCl_3$).

The Cd-precursor is prepared as follows: In a flask, CdO is dissolved in OA and ODE, and is mixed well. The mixture is heated under vacuum up to 100 °C for 15-20 minutes for the sake of purification. Then, the temperature is increased to 300 °C under inert atmosphere until a transparent, yellowish and viscous solution is formed. After this, the mixture can be cooled down to room temperature and stored in an air tight bottle. The Se-precursor is prepared as follows: 1 M solution of selenium powder is prepared in trioctylphosphine (TOP). For dissolving the Se-powder in TOP, constant stirring and heating to a

temperature of ca. 200 °C are required. Later, the injection mixture is prepared by mixing the required amounts of Se-stock solution, TOP and ODE.

The synthesis procedure is as follows: In a small three-neck flask, the mixture of TOPO, HDA, ODE and Cd-stock solution are prepared. The flask is evacuated while increasing the temperature up to 100 °C, again for the purification purposes. Subsequently the temperature is raised to 300°C under Ar flow to obtain clear colorless solution. At this point, the Se injection mixture is introduced into the reaction. QDs start to grow with time; the desired emission wavelength (equivalently the desired size of QDs) can be controlled by setting the reaction time. To stop the reaction in a short time, toluene is injected and the flask is cooled down in a water bath. The synthesis of CdSe QDs is finished. Figure 3.2 presents an exemplary setup in our lab and Figure 3.3 shows the synthesized CdSe QDs.

Figure 3.2 Synthesis setup of CdSe quantum dots.

Figure 3.3 CdSe quantum dots synthesized in Demir Lab at UNAM.

Another important class of these materials is the core/shell QDs. Covering the core QD with a material having a larger bandgap allows for a better control of the optical properties of the QDs, protection against photo-oxidation, obtaining higher photoluminescence quantum efficiencies, and tuning of the emission within a wider range of wavelengths; in addition, the control of the band alignment is possible via the selection of the shell material [43]. As a result, type I and type II QDs can be synthesized. In type I QDs, the electrons and holes are both confined in the core, whereas in type II QDs electrons and holes are confined in different parts of the QD, one in the core and the other in the shell. The most common core/shell QDs are CdSe/CdS, CdSe/CdS/ZnS, PbSe/PbS, CdTe/CdSe, and CdSe/ZnTe. The first three of these QDs are of type I and the remaining two have a type II band alignment.

The synthesis of QDs in water has a significant importance since it is the natural medium where all the living organisms' habitat is located and the chemical reactions of the living species take place. Therefore, especially for the biological applications, it is required to obtain QDs which are dispersed in water [51].

Since the synthesis environment is water, the reaction temperature in this type of QDs is limited with the boiling temperature of water, 100 °C. This relatively low temperature makes this type of synthesis safer and easier to implement. One of the most common QDs synthesized in the aqueous medium

is CdTe [51]. Similar to the organic synthesis, surfactants are also very crucial for this type of synthesis. These surfactants serve as stabilizers. As stabilizers, thiols with a short chain (up to 4 carbon units) with several functional groups (amino, carboxylic, hydroxylic, etc.) are used. Most popular stabilizers are thioglycolic (or mercaptoacetic) acid (TGA), mercaptopropionic acid (MPA) and 2-mercaptoethylamine (or cysteamine). TGA and MPA allow for stable (typically for years) negatively charged aqueous solutions of CdTe QDs due to the presence of surface carboxylic groups [51]. Although cysteamine stabilized QDs are less stable, positive surface charge in a neutral or acidic medium is the reason of interest in them.

The pH value of the synthesis medium has very significant effects on the quality of the synthesis. Optimum pH depends on the choice of stabilizer. For cysteamine, this value should be between 5.6 and 6.0; for TGA, the recommended value is 11.2-11.8 [52]. As an exemplary synthesis of QDs in polar media, one of the methods for CdTe is given below according to Ref. 52:

The required chemicals for the synthesis are aluminum telluride lumps (Al_2Te_3); cadmium perchlorate hexahydrate ($Cd(ClO_4)_2{\cdot}6H_2O$); thioglycolic acid (*TGA*: $(SH)CH_2COOH$); milli-Q (MQ) water; sodium hydroxide ($NaOH$); sulfuric acid (H_2SO_4); iso-propanol (C_3H_7OH).

The synthesis procedure is as follows: In a round bottom 3-neck reaction flask, required amounts of $Cd(ClO_4)_2{\cdot}6H_2O$ and MQ water are put and stirred. After observing all of the Cd-source is dissolved, TGA is added to the mixture. At this step, the color of the solution becomes milky. Then the pH of the solution is set to 11.8 by adding NaOH solution. In a separate small three-neck flask, Al_2Te_3 is put. Also, in another bottle 0.5 M H_2SO_4 solution is prepared. After connecting the bottle containing Te-source to the big flask, the system is flashed with Ar to remove oxygen dissolved in water to keep the Te-source from oxidation. At the same time, bottle of H_2SO_4 is bubbled with Ar. Then, 10-12

mL of H_2SO_4 is taken with a syringe and it is injected on to the Te-source. This will create H_2Te gas, which will be carried to the flask containing the Cd-source with the help of Ar flow. The color of the solution turns into pinkish-red color at this step. Then the mixture is heated until it boils. Boling of the solution corresponds to the formation of the QDs. As the time passes, the size of the synthesized QDs becomes larger leading to a shift in the photoluminescence peak towards longer wavelengths. Figure 3.4 shows an exemplary setup of water soluble CdTe QD synthesis. Both type of the QDs described here can be synthesized in our lab at UNAM.

Figure 3.4 Synthesis setup of CdTe quantum dots.

3.1.2 Optical Properties of Quantum Dots

The optical properties of the quantum dots change dramatically by changing their sizes as a result of quantum confinement effect. The emission wavelength shifts to longer wavelengths as the size of the QD increases because the electrons and holes are confined within a larger volume and the ground state energy levels of QDs are reduced, which consequently decreases the optical gap in Equation (3.5) and causes a red shift in the emission. The emission spectra of QDs are well defined Gaussian functions with emission line-widths determined

by their size distributions [53]. If the size distribution of QD is narrowed down, the emission spectra would have a narrower full-width at half-maximum.

One can tune the emission spectrum of QDs by changing the QD size as well as by selecting the correct material system over a desired range of wavelengths (e.g., below 400 nm to ca. 2000 nm [54]). For example, ZnSe QDs can emit at very short wavelengths, below 400 nm; whereas CdS, CdSe and CdTe QDs emit within the visible region. Covering the core of the QDs with a shell material having a larger bandgap causes further red shift in the emission spectrum. The FWHMs of the QD emission vary from 15 nm [55] to 50 nm [43]. Since the emission wavelengths and the FWHMs of QDs can be tuned within a broad range, QDs are very suitable materials for applications that require good spectral tuning capabilities such as white light source design. On top of these, achieving photoluminescence quantum efficiencies above 90% in solution (and over 70% in film) further strengthens the position of QDs for this kind of applications [56].

Another striking feature of the QDs is their absorption properties. As opposed to organic molecules, QDs exhibit a very broad absorption spectrum, which starts at the energy level of the first excitonic state and further increases towards shorter wavelengths following a small decrease after the excitonic state. The location of the excitonic state is tunable by controlling the material system and particle size. As in the emission peak, the excitonic peak red-shifts with the increasing QD size. Typical absorption spectra of QDs are given in Figure 3.5 [57]. These properties of QDs make them even more suitable for lighting applications since it leads to high flexibility in the choice of pump wavelength.

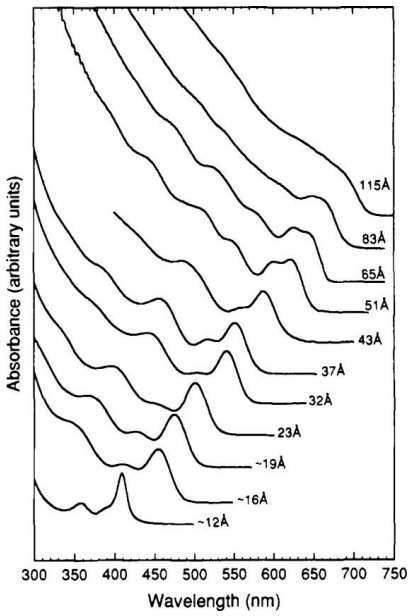

Figure 3.5 Absorption spectra of CdSe QDs having different sizes [57].

3.2 Conjugated Polymer Nanoparticles

Another material type that can be used for generating white light is the conjugated polymer nanoparticles (CNP). These nanoparticles, whose building blocks are the conjugated polymers, hold great promise also in the areas of bio-imaging, bio-sensing, and photonics in addition to the solid state lighting. Their optical properties can be tuned by selecting proper polymers and surface modification methods. In addition, their preparation is easier and they have less toxicity compared to other inorganic materials such as quantum dots. These are basically the main reasons why CNPs have attracted great attention in recent years [58]. In this section of the thesis, we focus our attention on CNPs dispersed in water.

There are mainly two different CNP preparation methods. These are the so-called miniemulsion and reprecipitation approaches [58]. The miniemulsion approach is the most frequently used one. According to this method, the polymer is first solved in an organic solvent, which is not miscible in water. The prepared

solution of polymer is then injected to water where surfactant molecules are dissolved prior to the injection of polymer [59]. Following this, the prepared mixture is ultrasonicated so that small and stable polymer droplets can be formed. Finally, the organic solvent, which is used to solve the polymer in the first step, is evaporated and polymer nanoparticles, whose sizes vary from 30 to 500 nm, are obtained [58]. Examples of polymer nanoparticles prepared using miniemulsion method are poly(3,4-ethylenedioxythiophene) (PEDOT), poly(thiphene-3-yl-acetic acid) [60], polyacetylene [60,61] and poly(arylene diethynylene) [62].

The second CNP preparation method is the reprecipitation approach. Here, first the conjugated polymers are dissolved in a good solvent, and then this prepared solution is added into a liquid medium, which is not compatible with the polymer but has a good miscibility with the solvent of the polymer. Subsequently, the prepared system is ultrasonicated to help the nanoparticle formation. The final step is the evaporation of the polymer solvent so that CNP dispersion in water is obtained [58]. An example for the polymer solvent is tetrahydrofuran (THF) and for the liquid medium miscible with the polymer solvent is water.

The mechanism leading to nanoparticle formation is basically the hydrophobicity. Upon the addition of the organic solvent into the water, hydrophobic polymer chains take a spherical form to minimize the contact with the water [58,63]. One of the main advantages of this method is the absence of any additive such as surfactants, which enables the applicability of the reprecipitation approach to many different conjugated polymers. Considering potential photophysical effects of these additional molecules, reprecipitation method provides a better control of the properties of the CNPs. Moreover, this method allows for the formation of nanoparticles, whose sizes change from 5-10 nm [58] to 400-500 nm [64], by controlling the polymer concentration and polymer molecular weight [58]. At this point it is worth mentioning that the

origin of the modified optical properties of CNPs is not the quantum confinement effects as opposed to inorganic quantum dots. Instead their optical properties mainly rely on the conformational change of polymers and the nature of aggregates [58]. However, the change of optical properties can still be observed depending on the particle size [65], although there have been reports on the stability of optical properties upon nanoparticle formation [66]. This basically shows us that there is no certain optical behavior modification of CNPs which can be given as a rule of thumb unlike QDs; on the contrary, each polymer, preparation method, solvents and surfactants might result in different optical properties of the nanoparticles.

In addition to these existing methods, there is another method which is based on the reprecipitation approach. In this case polymers containing functional groups, which can be crosslinked, form CNPs. After the nanoparticle preparation method, the CNPs are exposed to UV light so that a shell-like structure covers the CNP core [63]. The creation of a core/shell-like structures increases the mechanical stability of the nanoparticle and opens a pathway for the spectral tuning of CNP emission. Since the polymer core and crosslinked shell have different energy levels, they radiate in different wavelengths. In addition, radiative and non-radiative energy transfer occurs between the non-crosslinked core of the CNP and its crosslinked shell. As a result, color tuning can be succeeded via varying mechanisms. Figure 3.6 shows the SEM image of poly[(9,9-dihexylfluorene)-co-alt-(9,9-bis(3-azidopropyl)fluorene)] (PF3A) nanoparticles prepared using this method and crosslinked for three hours of UV exposure (Figure 3.6)[63].

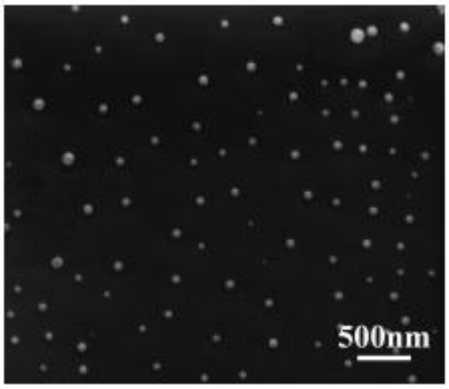

Figure 3.6 SEM image of conjugated polymer nanoparticles of poly[(9,9-dihexylfluorene)-co-alt-(9,9-bis(3-azidopropyl)fluorene)] (PF3A) which are crosslinked for three hours [63].

In the literature several optoelectronic device applications using CNPs are demonstrated, among these devices are polymer light emitting diodes, light emitting electrochemical cells and photovoltaics [67-74]. However, all of these devices are constructed using the CNPs prepared by miniemulsion method. Recently, we demonstrated a proof-of-concept LED relying on the color conversion phenomenon of crosslinked CNPs prepared by reprecipitation method [63]. However, there is still no demonstration of an electroluminescent device of CNPs prepared using this method [58].

Chapter 4

White Light Emitting Diodes

The solid state lighting is expected to replace the existing light sources such as incandescent and fluorescent lamps in the near future, because of its superiority [75]. In this chapter we focus on the existing technology of white light emitting diodes (white LEDs). We start reviewing the traditional light sources. Following this, we discuss the efficiency requirements for white light sources. Finally we review with white LEDs having different material systems and structures.

4.1 Traditional White Light Sources

Among the traditional sources, kerosene illumination is the most primitive and worst one as it possesses the lowest photometric quality. However, it still continues to be used in the countries where the electricity supply is not available [76]. On the other hand, incandescent light sources are very widely used throughout the world although their use is forbidden in some countries such as Argentina, Switzerland, European Union, Australia and Canada [77-80]. The main reason of this ban is their very low power conversion efficiency (PCE), which is around 5% [75]. They are basically black body radiators; therefore, they can render the real color of the illuminated objects almost perfectly, in other words, featuring a color rendering index (CRI) of 100. However, in addition to the low PCE, another weak point of them is the low luminous efficacy of optical radiation (LER) (ca. 15-20 lm/W_{opt}) [81], which is directly related to the broad blackbody radiation spectrum. When it comes to the

fluorescent lamps, low photometric performance issues still continue. Their emission spectra lead to a LER of ca. 70 lm/W_{opt} [82], which still remains low. Furthermore, its power conversion efficiency is also very low, though it is about five times better than incandescent lamps [75]. Another concern of fluorescent lamps is environmental (rather than being photometric). These lamps contain significant amount of mercury in gas phase; therefore, they present a serious risk of being harmful to environment as well as to human health in the case that the fluorescent tube is broken.

4.2 Requirements for High-efficiency in White Light Generation

As mentioned in Chapter 2, a good white light source has to satisfy some photometric and colorimetric properties so that it can deliver high-efficiency and high-quality. The most important two of these requirements are good color rendition and high-efficiency of the optical radiation perceived by the human eye. The first one is evaluated mostly using the metrics such as color rendering index (CRI) and color quality scale (CQS). As mentioned in Ref. 83, an efficient white light source should exhibit at least a CRI of 90 for indoor applications. Since the calculation method of CQS is very similar to CRI, this limit of CRI can also be used for CQS calculations. In addition to this, a warmer white shade is desirable for indoor lighting, which corresponds to correlated color temperatures (CCTs) less than 4000 K. On the other hand, for outdoor applications, CRI is also important because a high CRI increases the color contrast and consequently the objects under low optical power illumination can be perceived more easily [84]. The second performance criterion is evaluated in accordance with the luminance level of the light source. For indoor lighting, LER should be as high as possible, for which the targeted level is 408 lm/W_{opt} [83]. On the other hand, for outdoor applications the luminance in the mesopic regime should be higher. In addition, at even lower light levels, where the vision

regime is scotopic, having a high S/P helps to perceive higher brightness [31]. For example, the S/P of the standard daylight source D65, which is 2.47, can be used as a reference point. Obtaining a higher S/P yields a better brightness and perception at low light levels.

In addition to all of these points mentioned above, a high electrical efficiency is also important for the purposes of energy saving. According to the study of Phillips et al., the power conversion efficiency of the white LEDs have to be larger than 70% [83].

4.3 White Light Emitting Diodes

There are several methods of obtaining white light emission using light emitting diodes. The most important ones can basically be categorized into two. The first approach is the multichip LED approach, where the white light emission is generated via the radiation of individual LED chips. The latter method makes use of the photoluminescence of a fluorescent material, which is integrated on top of a LED emitting at a shorter wavelength. This phenomenon is called the color conversion, wavelength up-conversion, or energy down-conversion. Another important class of LEDs is the organic light emitting diodes (OLEDs), which are based on the electroluminescence of the organic molecules. Although they hold great promise in the future, currently, their efficiencies typically remain low and will have to be below 25% when the electroluminescence (and also photoluminescence) mechanisms relies on fluorescence (instead of phosphorescence).

4.3.1 Multichip White LEDs

In this method, LEDs emitting in different colors are packaged together such that a white light emission is collectively obtained. The blue and green colors are obtained via InGaN whereas red emission comes from AlGaInP [85]. Since the linewidth of LED emission is very narrow, around 20-25 nm, this method enables very good tuning of the emission spectra so that high photometric and colorimetric performance can be achieved. However, their main drawback is the cost of the overall system. Another important problem is the green gap. Today, there is no epitaxial material system, which provides an efficient electroluminescence in green region.

4.3.2 White LEDs Based on Color Conversion

The color conversion approach of white LEDs relies on the fact that the materials excited by a high-energy photon emit low-energy photons. There are several classes of these materials such as organic dyes, polymers, phosphors made of rare-earth ions and semiconductor quantum dots (QDs). The LED chip pumping the color convertors typically emits either in blue or near UV.

There are several organic dyes that can be incorporated in LEDs such as Coumarin 6 and Coumarin 450 [9,86]. Although this class of materials has very large quantum efficiencies, they have two serious drawbacks. One of them is their narrow absorption band, which limits the choice of the pump LED. Another one is their photo-bleaching problem.

The conjugated polymers can be incorporated on LEDs like the dyes mentioned above. By choosing appropriate polymers, one can tune the wavelength of the polymer emission. As in the case of dyes, these materials also have relatively narrow absorption bands, but very high quantum efficiencies.

Additionally, they also suffer from photo-bleaching. Another problem of the organic molecules is the change of optical properties in film as a result of restriction of conformational freedom. In addition to polymers themselves, their nanoparticles can also be used as color convertors, which substantially avoid strong modifications in the solid film once the particles are formed prior the casting them into a film. Furthermore, using conjugated polymer nanoparticles prepared by the reprecipitation method color tuning is possible, which might be helpful for lighting applications.

Another important and most widely used class of color conversion materials for white LEDs is the rare-earth ion doped phosphors. In general, yttrium aluminum garnet (YAG) is doped with the ions of rare-earth elements such as gadolinium (Gd), cerium (Ce) and terbium (Tb) [9,87]. Although this is the most common white light generation method using LEDs, it has some important pitfalls. One of them is the inevitable tail of red phosphors towards longer wavelengths, which significantly decreases LER and LE, although they have high photoluminescence quantum efficiencies [88]. It is not easy to control their emission spectra. Therefore, optimization of different colorimetric and photometric properties is not possible or very challenging. Moreover, in recent years, the mining of rare-earth elements, which is under the Chinese monopoly, encountered export quotas [87]. Therefore, Japan experienced a shortcoming on the supply of these elements and a global concern has risen whether the rare-earth element supply is going to be used for a bargaining chip in the international arena. Therefore, new alternatives are on high demand [89].

Considering the problems of phosphors, quantum dots (QDs) make a good alternative. Their narrow emission bands allow for good spectral tuning of white light; as a result, all of the photometric properties of the device can be optimized upon careful spectral designs [90]. Furthermore, recently QDs having high quantum efficiencies have been reported, which enables high power conversion efficiencies and consequently, high luminous efficiencies of white LEDs [56].

On top of these, the synthesis of QDs is easy and required materials do not suffer from supply problems. But a major issue is that cadmium-free QDs are required due to environmental concerns. However, the synthesis of these types of QDs is not as mature as Cd-containing ones and their quantum efficiencies typically remain lower compared to Cd-containing ones for the time being.

Chapter 5

Efficient White LEDs for Indoor Lighting using Quantum Dot Nanophosphors

5.1 Spectral Recommendations for White Light Emitting Diodes

This section is based in part on the publication "A photometric investigation of ultra-efficient LEDs with high color rendering index and high luminous efficacy employing nanocrystal quantum dot luminophores" T. Erdem, S. Nizamoglu, X. W. Sun, and H. V. Demir, Optics Express 18, 340 – 347(2010). Reproduced (or "Reproduced in part") with permission from Optical Society of America. Copyright 2010 Optical Society of America.

Warm white light sources with high CRIs and high LERs require the generation of a white emission spectrum by strategically selected colors with the lowest possible full-width-at-half-maximum (FWHM) values, as reported by Phillips et al. [83]. Our group previously reported that this requirement can be met in principle using semiconductor nanocrystal quantum dots. However, optical parameters including the peak emission wavelength (WL), full-width-at-half-maximum (FWHM), and the relative amplitude of each QD color component

need to be carefully designed to achieve such high-quality white light generation with CRI >90, LER >380 lm/W at a warm CCT (i.e., CCT <4000 K), which can compete with conventional white light sources [83]. Nevertheless, the previous works including ours and others have not addressed these requirements of ultra-efficient performance with CRI >90 and LER >380 lm/W_{opt} using quantum dot nanophosphors. Additionally, the fundamental relationship and trade-offs between CRI, LER, and CCT are still not completely understood for the case of luminophores with narrow FWHMs such as QDs. Prior to this work, only the dependence of CRI and LER at 4870 K has been reported with only 2000 different spectra [91]. In this work, we present the required parameters for high-quality warm white light generation as well as the relationship and trade-offs between the performance parameters of the light source by investigating 237,109,375 QD-WLED designs.

5.1.1 Calculations

We developed a computational approach to photometrically evaluate different LED designs. In our simulations, the emission spectrum of QDs is modeled as a Gaussian function [53]. The chosen wavelength intervals for each color source are swept with a 10 nm step size between 450 and 490 nm for blue, between 500 and 540 nm for green, between 550 and 590 nm for yellow, and between 600 and 640 nm for red. In addition, FWHM of each color component is changed between 30 and 54 nm with a step size of 6 nm. Furthermore, the amplitude of each color component spectrum is varied by multiplying with an integer between 1 and 5. Subsequently, the amplitudes of every color component are normalized to 1000 for easy comparison with other spectra. By considering all of the different spectral combinations, a total of 237,109,375 possible emission spectra have been systemically generated and investigated using [9] for LER and CRI calculations and [92] for CCT computations.

5.1.2 Results

To obtain warm white light sources with CRI >80, LER >300 lm/W_{opt} at 1500 K< CCT < 4000 K, the generated emission spectra are selected and tested. As a result of the simulations, only 4,896,155 spectra are left, which correspond to ca. 2% of the entire spectra generated. When the spectra with CRI <90 and LER <380 lm/W_{opt} are filtered out, the number of remaining spectra is decreased to 3192, corresponding to ca. 0.001% of the entire number of spectra tested. This finding shows that efficient white LEDs with high color quality are in fact hard to achieve. Therefore, it is very critical to understand the effect of the input parameters on the performance criteria and also the trade-offs between them as discussed below.

5.1.2.1 Input Independent Analysis

To understand the relationships between CRI, LER, and CCT, the graph of CRI vs. LER is presented in Figure 5.1 by only considering the data satisfying 2450 K< CCT <2550 K, 2950 K< CCT <3050 K, and 3450 K< CCT <3550 K. The investigation of these curves shows that CRI decreases as LER increases in all of the CCT cases. This relationship makes it clear that the performance in terms of CRI should be sacrificed to obtain high optical efficiency. Additionally, it is observed that the highest possible CRI value decreases when CCT increases. However, this change is not significant so that it is still possible to obtain high-quality warm white LEDs with high CRIs at low CCTs. For example, theoretically it is possible to achieve an emission spectrum satisfying LER >380 lm/W_{opt} and CRI >90 below a CCT of 2500 K (at CCT=2326 K). Another important result of the input independent analysis comes out to be the increase of the highest achievable LER when CCT increases. Thus, there is a trade-off for obtaining high efficacy and warm color temperature at the same time. Furthermore, as CCT increases, the slope of the curve gets gentler at the same

LER value on the border. This shows that the change of CRI with respect to LER slows down as CCT increases.

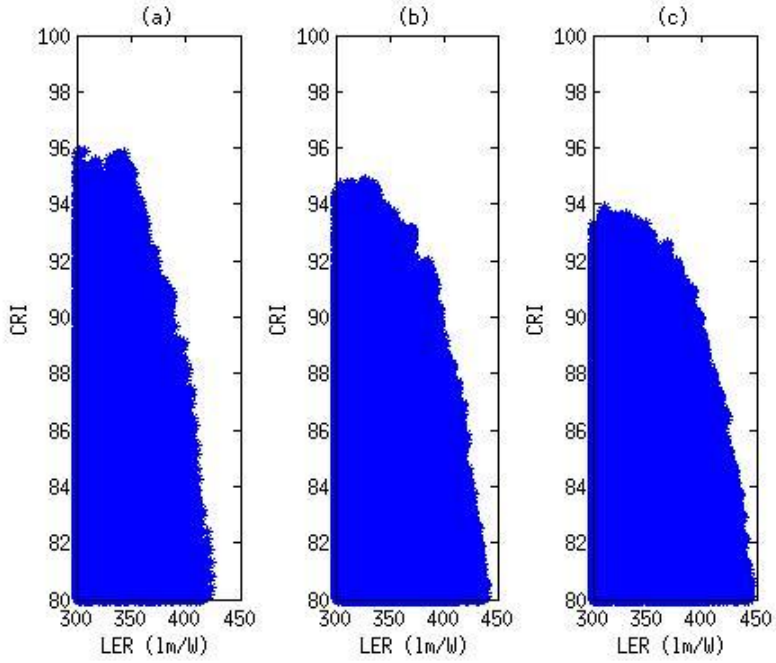

Figure 5.1 CRI vs. LER dependence between (a) 2450 K< CCT <2550 K, (b) 2950 K< CCT <3050 K, and (c) 3450 K< CCT <3550 K.

The relationships of CRI vs. CCT, CRI vs. LER, and LER vs. CCT are investigated and the results are shown in Figure 5.2(a), (b) and (c), respectively. In Fig. 2(a), the highest obtainable CRI value increases from 1500 to 2200 K. After 2200 K, CRI starts to decrease. The analysis of the spectra at the boundaries reveals that these points in the region between 1500 and 2200 K have LERs approximately 300 lm/W_{opt}, which is due to our restriction of LER >300 lm/W_{opt} in our calculations. After 2200 K, however, the boundary LER values are much higher than 300 lm/W_{opt}, and this is the region where the fundamental trade-off between CRI and CCT appears. In Figure 5.2(b), the maximum obtainable CRI does not change significantly for low LER values between 300 and 330 lm/W_{opt}; however, further increase of LER causes CRI to decrease. This relation between CRI and LER is expected because if one source has a high CRI, its spectrum should have a power distribution covering the visible region. Therefore, LER decreases with wider emission spectrum. Also

the analysis of the boundary points shows that there does not exist a general trend between CCT and CRI. By analyzing together with the results of the previous analysis, we conclude that the border of the CRI vs. LER graph is formed by the limiting trade-off of CRI vs. LER at different CCT levels. As shown in Figure 5.2(c), the increase of LER requires the increase of CCT. To obtain light sources with high LERs, the generated spectra should be cooler because the spectral power distribution around the peak of the eye sensitivity function increases. If we investigate the points having the highest LERs, these points are observed to exhibit CRI values very close to our restriction of 80, which limits the LER vs. CCT graph.

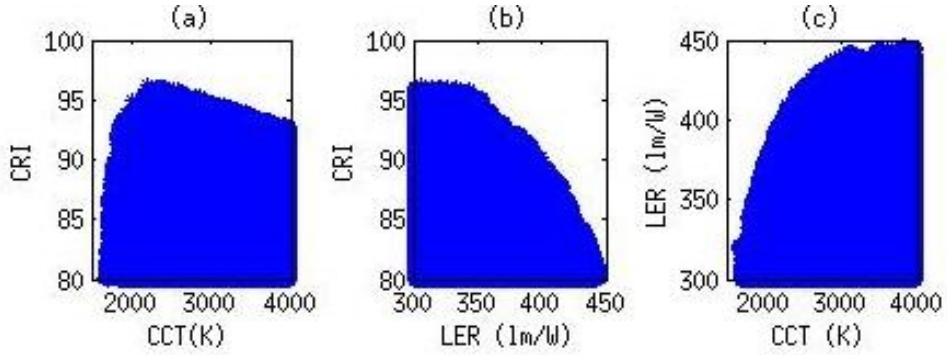

Figure 5.2 Relations between (a) CRI and CCT, (b) CRI and LER, and (c) LER and CCT.

We further investigate whether the analyzed spectra fall in the white region on CIE 1931 chromaticity diagram. This analysis, however, requires a mathematical definition of the white region, but such a commonly accepted or widely used definition has not been found in the literature. To define the white region, we mathematically analyze the elliptic white area given in Ref. 9. By fitting this ellipse, we derive Equations (5.1)–(5.3) to define the white region used in this work. Our analysis shows that the photometric relations for only white points (shown in red in Figure 5.3) follow those for all data points including near-white points (shown in blue in Figure 5.3). Noticeably, in Figure 5.3 most of the data points are found to fall in the white region.

$$x' = \frac{y + 1.67x - 0.885}{1.9495} \quad \textbf{(5.1)}$$

$$y' = \frac{y - 0.607x - 0.109}{1.1648} \quad \textbf{(5.2)}$$

$$\frac{x'^2}{0.1339^2} + \frac{y'^2}{0.0944^2} \leq 1 \quad \textbf{(5.3)}$$

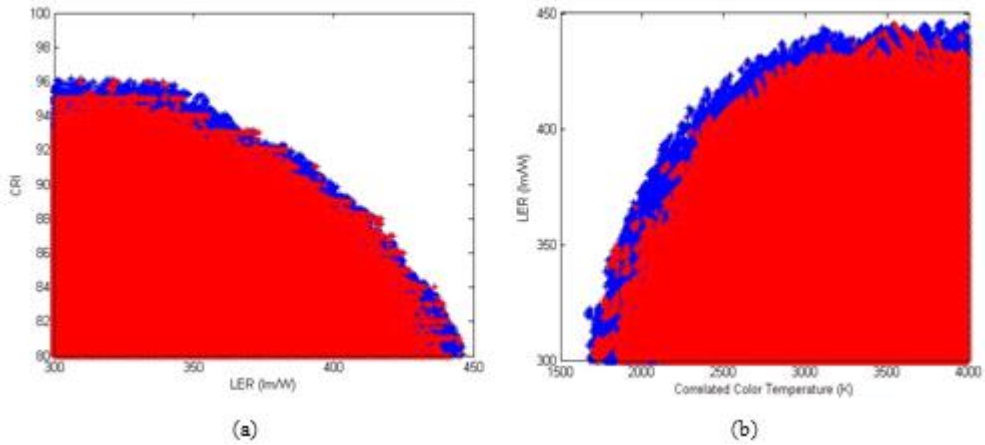

Figure 5.3 (a) CRI vs. LER relationship and (b) LER vs. CCT relationship for white data points (shown in red) and near-white points (shown in blue).

5.1.2.2 Input Dependent Analysis

The input parameters in our simulation include FWHM, relative amplitude, and peak emission wavelength. The analysis of the effects of the input parameters is carried out by calculating the average and standard deviation (stdev) of every input parameter satisfying two conditions: The first condition is CRI >80 and LER >300 lm/W_{opt} and the second one is CRI >90 and LER >380 lm/W_{opt}. The average and stdev of the cases passing these thresholds are presented in Table 5.1.

5.1.2.2.1 Analysis of FWHMs

When the FWHMs of blue, green, and yellow color components are studied for both sets of conditions, it is observed that their average is around 43 nm and their stdev is ca. 8.3 nm in both cases. Such a high stdev of FWHM and almost the same average values for both of the cases show that the choice of FWHM for these color components is not critical to obtain high performance in designing QD based white LEDs. When the same analysis is conducted for the red color region, significantly different results are obtained. For CRI >80 and LER >300 lm/W_{opt}, the average FWHM for red is around 40 nm with a similar stdev of other color components. However, for CRI >90 and LER >380 lm/W_{opt}, this average FWHM decreases to 32 nm and its stdev significantly decreases to 3.5 nm. Considering that the narrowest FWHM in these calculations is 30 nm, it can be concluded that the FWHM of the red component is very critical for high performance and the emission linewidth should be as narrow as possible.

5.1.2.2.2 Analysis of Peak Emission Wavelengths

The comparison of both performance criteria presented above in the blue spectral region shows that the average peak wavelength of blue color remains almost the same for both cases, around 465 nm, with a relatively high stdev (12.6 and 9.1 nm). Although there is a decrease in stdev in the high performance case, it is still not a very strong restriction for high performance. This shows that blue peak emission wavelength is not so critical, as long as it is not significantly different from 465 nm.

In the green spectral region the average peak emission wavelength for both cases is ca. 527 nm, again with a relatively high stdev (11.6 and 9.1 nm). Although we observe a decrease of 2.5 nm in the standard deviation, this decreased value of the standard deviation still does not strongly restrict the choice of peak emission wavelength in the green spectral range. This points out that the

green peak emission wavelength is not as critical, either, provided that it is close to 527 nm.

In the yellow spectral region, the average peak emission wavelength for CRI >80 and LER >300 lm/W_{opt} is 574.8 nm with a stdev of 13.2 nm. For CRI >90 and LER >380 lm/W_{opt}, the average peak emission wavelength is blue-shifted by ca. 6 nm. Although the standard deviation is not low (ca. 10 nm), it is still worth noting this shift of the average peak emission wavelength. By considering these results, it can be concluded that the peak emission wavelength of yellow component should be around 570 nm for high performance, but high stdev allows a wider window for choosing the peak emission wavelength.

		For CRI>80 & LER > 300 lm/W_{opt}		For CRI>90 & LER > 380 lm/W_{opt}	
		Average	Standard Deviation	Average	Standard Deviation
FWHM (nm)	Blue	43.2	8.4	44.4	8.3
	Green	42.4	8.5	43.3	8.4
	Yellow	44.1	8.3	44.0	8.2
	Red	40.4	8.3	32.1	3.5
WL (nm)	Blue	465.7	12.6	465.1	9.1
	Green	527.0	11.6	527.9	9.1
	Yellow	574.9	13.3	569.0	9.7
	Red	625.5	9.0	620.7	2.5
Relative amplitude (/1000)	Blue	160.9	64.3	97.5	19.6
	Green	213.2	81.1	229.0	77.5
	Yellow	243.0	78.2	241.3	71.1
	Red	383.2	75.9	432.4	48.7

Table 5.1 Average and standard deviation values of the input parameters of the spectra satisfying the conditions of CRI >80 and LER >300 lm/W_{opt}, and CRI >90 and LER >380 lm/W_{opt}.

The average peak emission wavelength of the red color component is around 625 nm with a relatively high stdev (ca. 9 nm) in the case of CRI >80 and LER >300 lm/W_{opt}. For CRI >90 and LER >380 lm/W_{opt}, the average peak emission wavelength shifts to 620.7 nm together with a strong decrease in stdev down to 2.5 nm. This shows that one of the most critical components for high performance is the peak emission wavelength in the red spectral region. To

obtain high performance, red peak emission wavelength needs to be close to 620 nm.

5.1.2.2.3 Analysis of Relative Amplitudes

In the case of CRI >80 and LER >300 lm/W_{opt}, the average relative amplitude of blue component is around 161/1000. This value decreases to 97.5/1000 for CRI >90 and LER >380 lm/W_{opt} case. This shows that the amount of blue color should be very small to obtain high performance. Additionally, the decrease of stdev from 64.3/1000 to 19.6/1000 indicates that the weight of the blue component should be close to the indicated average value.

The analysis of the relative amplitude values in the green spectral region shows that the average weight of the green component is 213.2/1000 in the case of CRI >80 and LER >300 lm/W_{opt}. For the high performance case, this value increases to 229.0/1000. The stdev for both of the cases is relatively high (around 80/1000), which indicates that the relative amplitude of green component has a relatively large window because of its high standard deviation value.

For CRI >80 and LER >300 lm/W_{opt} case, the average amplitude of the yellow component is observed to be 243.0/1000. In the high performance case, this value remains almost the same. Moreover, stdev values for both of the cases are relatively high (between 78.2/1000 and 71.1/1000, respectively). As a conclusion, in order to obtain high performance, the relative amplitude of the yellow component should be around 240/1000 and the high standard deviation value allows to cover a larger relative amplitude window.

In the lower performance case with CRI >80 and LER >300 lm/W_{opt}, the average value of the relative amplitude of the red color is around 383/1000. In the higher performance case with CRI >90 and LER >300 lm/W_{opt}, the red

component grows stronger and the average value increases to 432.4/1000. In addition to this, standard deviation decreases from 75.9/1000 to 48.7/1000. When all of this information is considered, it turns out that the weight of the red component is very critical for high performance due to its low standard deviation. Thus the relative amplitude of red color should be as close as possible to 430/1000. According to the results of these calculations, some exemplary spectra and their performance are given in Table 5.2.

WL (nm)	Relative amplitude (/1000)	FWHM (nm)	LER (lm/W_{opt})	CCT (K)	CRI
460, 530, 570, 620	91, 182, 273, 455	36, 54, 54, 30	380	2600	90.7
470, 530, 570, 620	91, 273, 182, 455	54, 48, 30, 30	388	3000	91.7
450, 510, 560, 620	83, 167, 333, 417	30, 30, 42, 30	384	3200	91.0
460, 520, 560, 620	100, 200, 300, 400	36, 42, 54, 30	385	3400	90.8

Table 5.2 Exemplary results of the photometric computations. In the columns of WL, relative amplitude, and FWHM, the first numbers belong to the corresponding property of the blue spectrum. The other numbers in those columns stand for green, yellow, and red spectral content, respectively.

The average values of CRI >80 and LER >300 lm/W_{opt} results in a spectrum with CRI=92.0, CCT=3308 K, and LER=352 lm/W_{opt}, and the photon counts in blue, green, yellow, and red region are 132.2/1000, 198.3/1000, 246.5/1000, and 423.0/1000, respectively. When the average values of the parameters in the high performance case (CRI >80 and LER >300 lm/W_{opt}) are used, the resulting spectrum exhibits CRI = 91.3, CCT = 3041 K, and LER=386 lm/W_{opt}, and the relative number of photons are 79.3/1000, 211.4/1000, 240.1/1000, and 469.3/1000 in blue, green, yellow, and red spectral regions, respectively. The relative spectral power distribution for the average values of input parameters for CRI >80 and LER >300 lm/W_{opt} and for CRI >90 and LER >380 lm/W_{opt} are shown in Figure 5.4(a) and Figure 5.4(b), respectively.

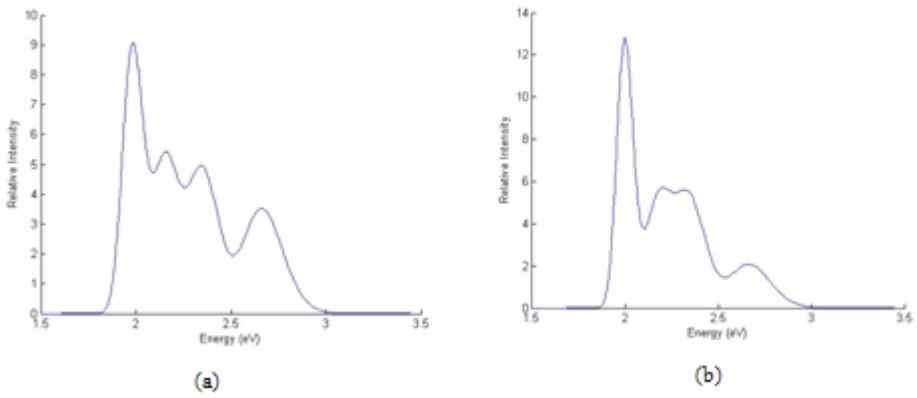

Figure 5.4 The relative spectral power distribution for the average values of input parameters in the case of (a) CRI >80 and LER >300 lm/W_{opt} and (b) CRI >90 and LER >380 lm/W_{opt}.

5.1.3 White LED design recommendations

To achieve white LEDs with high optical performance, it is advisable to use four colors in blue, green, yellow and red spectral ranges, as also suggested in [83]. Further recommendations can be considered in the light of Table 5.1, which presents a good pathway to obtain high performance. According to the results of this analysis, the color-component requirements for the corresponding peak emission wavelengths are 465.1 ± 9.1 nm for blue, 527.9 ± 9.1nm for green, 569.0 ± 9.7 nm for yellow, and 620.7 ± 2.5nm for red spectral region. Color-component FWHMs should be 44.4 ± 8.3 nm for blue emission, 43.3 ± 8.4 nm for green emission, and 44.0 ± 8.2 nm for yellow emission, considering the limitations determined by the respective standard deviation values. For the red region, however, it is important that its FWHM remains as narrow as possible (the smallest value in our simulations is 30 nm). Another significant parameter for high-quality white light generation is the relative amplitude of each color component. This should be 97.5/1000.0 ± 19.6/1000.0 (the weakest) for blue and 432.4/1000.0 ± 48.7/1000.0 (the strongest) for red, whereas the relative

amplitudes of green and yellow components need to be at the medium level of 229.0/1000.0 ± 77.5/1000.0 and 241.3/1000.0 ± 71.1/1000.0, respectively.

5.1.4 Conclusions

In conclusion, the relationship and trade-offs between the performance parameters including CRI, LER and CCT of the white LEDs are presented. Additionally, the effects of the parameters (peak emission wavelength, FWHM, and relative amplitude) of each QD color component are investigated on the performance of the resulting WLEDs. As a result, it is shown that the performance of ultra-efficient LEDs even with CRI >90 and LER >380 lm/W_{opt} is achievable in principle using QD luminophores. If such high-quality white LEDs integrated with QDs luminophores are realized, they are expected to be used in future indoor lighting applications to provide higher quality light compared to the current light sources.

5.2 Experimental Demonstration

This section is based in part on the publication "Warm-white light-emitting diodes integrated with colloidal quantum dots for high luminous efficacy and color rendering" S. Nizamoglu, T. Erdem, X. W. Sun, and H. V. Demir, Optics Letters 35, 3372 – 3374 (2010).

For generating white light emission, we hybridized CdSe/ZnS QDs on an InGaN/GaN blue LED emitting at 452 nm [93]. We used QDs emitting in three different colors; green at 528 nm, yellow at 560 nm and orange at 609 nm. However, these emission properties belong to QDs dissolved in toluene. Therefore, drop-casting these QDs in poly(methyl methacrylate) host results in unpredictable shifts in the emission properties due to environmental changes and

dipole-dipole interactions between QDs. To forecast whether the resulting spectrum can result in high photometric efficiency, we employed a simulation by modeling QD and blue LED emissions as Gaussian functions. We changed the peak emission wavelengths of the blue component between 450–470 nm, the green component between 535–555 nm, the yellow component between 557–577 nm and finally the orange component between 610–630 nm, all with a step size of 10 nm. The FWHMs of blue, green and yellow QD films are changed between 25 and 55 nm, with a step size of 10 nm. The FWHM of the red component is varied from 30 to 50 nm, with a 10 nm step size. As another parameter of optical spectrum design, we also changed the amplitudes of every color components. The amplitudes of blue, green and yellow components are changed between 430 and 470, 750 and 790, 470 and 510 units, respectively, all with a step size of 20 units. The red component is designed so that its amplitude changes between 1400 and 1500 with a step size of 50 units. All in all, we simulated 1,180,980 white LED designs and found out that high photometric performance can be achieved (Figure 5.5).

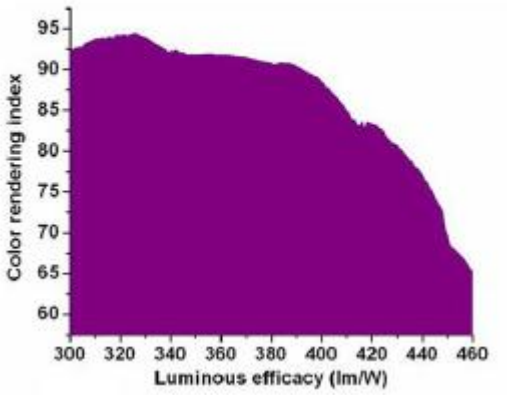

Figure 5.5 Potential performance of white LED designs using the combinations green, yellow and orange of QDs emitting at 528, 260 and 609 nm [93].

By using the QDs stated above, we hybridized three different white LEDs. The first one is built up using 31.91 nmol, 1.42 nmol and 0. 37 nmol of green, yellow and orange emitting QDs, respectively (WLED#1). This white LED possessed a CRI of 89.2 and a LER of 357 lm/W_{opt}, together with a CCT of

2982 K when the blue LED is driven with a current of 12 mA. The corresponding spectra and the chromaticity coordinates at various currents are given in Figure 5.6.

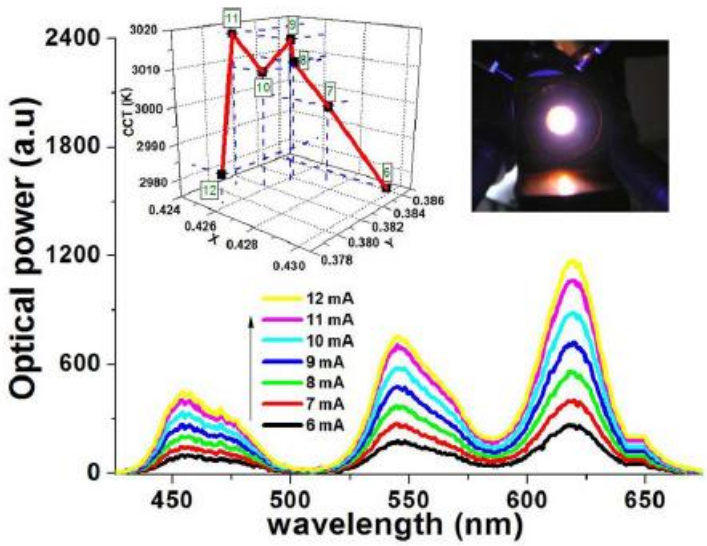

Figure 5.6 The emission spectra and chromaticity coordinates of WLED#1 together with the picture of the white LED [93].

The second white LED contains the same amount of green and yellow QDs, however, red content is increased to 0.55 nmol. As a result of this, the spectrum of WLED#2 reveals a CRI of 88.9 and LER of 349 lm/W_{opt}, together with a decreased CCT of 2781 K. Corresponding spectra at varying current levels can be found in Figure 5.7, which also demonstrates the change of chromaticity points and the picture of the WLED#2.

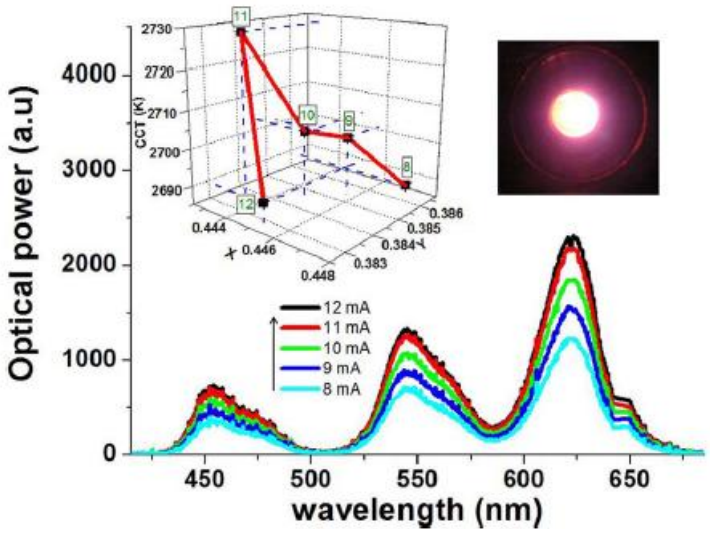

Figure 5.7 The emission spectra and chromaticity coordinates of WLED#2 together with the picture of the white LED [93].

Further increase of the red QD content to 0.74 nmol causes very small drops in CRI and LER down to 87.8 and 339 lm/W_{opt}, respectively. As the red content is increased, WLED#3 has a warmer white emission corresponding to a CCT of 2390 K. Figure 5.3 presents the electroluminescence spectra of WLED#3 together with their chromaticity coordinates and the picture of the working device.

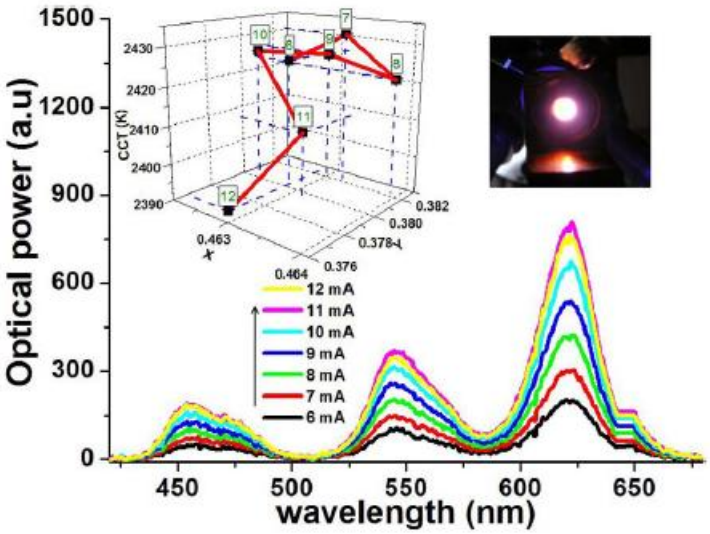

Figure 5.8 The emission spectra and chromaticity coordinates of WLED#3 together with the picture of the white LED [93].

In conclusion, we demonstrated that high photometric performance of QD-WLEDs is achievable and furthermore, the photometric properties of the device are tunable by controlling the QD amounts in the device architecture [93]. We further showed that we can tune the white LED spectra so that its color rendition performance is enhanced for all of the test samples used in the calculation of CRI.

5.3 Power Conversion and Luminous Efficiency Potentials of QD-WLEDs

This section is based in part on the publication "Power conversion and luminous efficiency performance of semiconductor quantum dot nanophosphors on light-emitting diodes" T. Erdem, S. Nizamoglu and H. V. Demir, in submission.

As mentioned in the previous chapter, rare-earth ion based phosphors are the most preferred color converters in white LEDs. Although they achieved individual levels of LER ≥270 lm/W_{opt} [94], CRI ≥90 [95], CCT ≤4000 K [96] and LE ≥140 lm/W_{elect} [97] in different implementations, optimization of these properties cannot be realized together because of their fundamental broad band emission and consequently because of the difficulties in spectral tuning. Additionally, the concerns have increased recently regarding the supply of the rare-earth elements and alternatives to them are therefore in high demand [87,89]. One of the candidates to replace phosphors is the semiconductor colloidal quantum dots (QDs). Using the QDs for color conversion on LED chips to generate white light emission allows the tuning and optimization of emission spectrum and corresponding color optimized thanks to their narrow emission linewidths. Because of the same reason, very high photometric performance (LER ≥380 lm/W_{opt}, CRI ≥90 and CCT ≤4000 K) can be achieved

simultaneously when QD combinations are selected carefully [90]. On top of these, the colloidal synthesis of QDs is easy and their quantum efficiencies reached very high levels, exceeding 90% in solution and 70% in film [56]. This may potentially lead to high levels of PCE and correspondingly high LE. However, PCEs and LEs of such high photometric quality QD-LEDs have not been studied and their potential for ultra-high performance have not been examined. Moreover, the potential effects of different architectural designs on QD-WLEDs were unknown till date. In this part of this thesis, we examined these missing points by studying and modeling the photon conversion processes of QDs as color convertor nanophosphors in two main architectures considering the changes of their quantum efficiencies.

5.3.1 Computational Models of PCE and LE Calculations

Our computational models are based on four-color mixing white LEDs, where green-, yellow- and red-emitting QDs are integrated on top of a blue LED. Furthermore, we worked only on the designs possessing CRI ≥90, LER ≥380 lm/W_{opt} and 1500 K ≤CCT ≤4000 K to satisfy high photometric performance criteria using the results of Ref. 90. In these architectures, the generation of white light relies on the color conversion phenomenon. Green, yellow and red QD layers are pumped by the blue photons generated by blue LED, or else these photons are extracted from the device without being absorbed in QD layers. The generated green photons are either absorbed within green QD layer or lost because of the non-unity quantum efficiency of the QDs. Some of them are also absorbed by yellow or red QDs whereas the remaining ones are out-coupled. Yellow photons are generated by the pumping of blue or green photons. These yellow photons can be absorbed by the yellow QDs, while some of them are absorbed by red QDs and remaining ones are extracted. Red photons are generated through the pumping of blue, green or yellow photons in the red QD

layer. Some of these photons are also lost because of the self-absorption and non-unity quantum efficiency of red QDs and the rest might be out coupled. As a result, a white light spectrum is obtained containing photons generated by blue LED and by green, yellow and red QD layers.

Our models are based on two basic white LED architectures. The first architecture (*A*) has red, yellow and green QD layers in order from bottom to top on the blue LED. The latter architectural design (*B*) is the blend of red, yellow and green QDs placed on the LED (Figure 5.9). The photon transfer equations of both of the architectures are derived using system box approach of control theory. Every system box denotes an emission or absorption process with a corresponding fraction (or probability) of photons experiencing the associated process within or between the QD layers. In our calculations, we made use of two different power conversion efficiency (PCE) for the blue LED: one having a unity PCE, which is used to examine the performance of QD layers on an ideal blue LED chip and explore the effects of color conversion alone, and the second one is taken as an experimentally demonstrated, high-performance LED having a reported PCE of 81.3% [98].

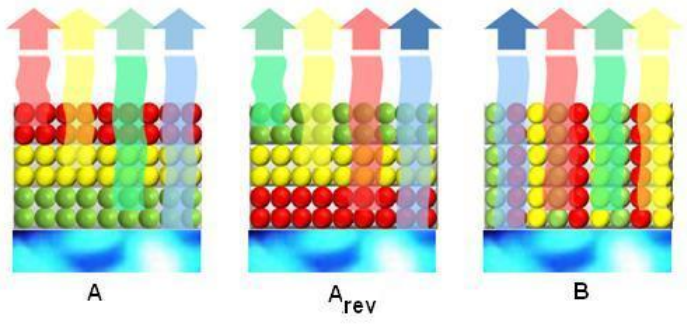

Figure 5.9 Three basic architectures of QD-WLEDs modeled in this work: *A*, A_{rev} and *B*.

In our computations we used several assumptions to make the calculations feasible. First, we assumed the full reflection of the downwards emitted light from the bottom perfect mirrors such that only the photons traveling upwards leave the device. Moreover, the effects of scattering occurring due to QDs are ignored together with the reflections between QD layers. We performed our

computations for an extraction efficiency of unity during the transition of photons from the red QD layer to the air, which can be approximately realized physically with specially designed structures. Also, the emission spectra of the blue LED and QDs are assumed to be Gaussian functions. Another assumption has been that all of the photons within the same Gaussian spectrum experience the same absorption coefficient. Although this one is a crude assumption, we have observed that this assumption still succeeds in providing very accurate results as long as the peak emission wavelength of the Gaussian spectrum to be absorbed is far away from the excitonic peak of the absorbing QD layer. The error is the largest when the emission peak is near to the excitonic peak of the absorbing QD layer. For the QD film thicknesses we use, this corresponds to a maximum error of ca. 0.1 in the absorbed photon fraction. Therefore, self-absorption (SA) is underestimated. If the quantum efficiencies of QDs decrease, the required layer thicknesses increase as well. Consequently, this deviation from the correct value is observed to decrease. Another assumption we further made in this work is that a fraction *k* of the generated photons from QDs is emitted upwards and remaining *1-k* downwards, that the downwards emitted photons are totally reflected back from a mirror so that all of the photons leave the device from its top side. The results that we present in this work correspond to the case of k=1/2.

To calculate PCE and LE, first the emission spectrum of QDs has to be related to their absorption spectrum. To achieve this, CdSe QDs are chosen because of the availability of the required information in the literature. The emission peak (λ_{em}) and the first exciton peak of the absorption spectrum (λ_{abs}) are related by fitting a linear semi-empirical curve to the data provided by Boatman et al. [99], as in Equation (5.4):

$$\lambda_{abs} = \frac{\lambda_{em} - 8.3045}{1.0308} \qquad \textbf{(5.4)}$$

The absorption spectrum of QD films are taken from Ref. 100 and absorbed fraction information is converted to absorption coefficient data for large QDs

having a thickness of 200 nm. The absorption coefficient of a QD given its emission peak is found by shifting the data obtained from Ref. 100 in accordance with λ_{abs}.

The PCE of a QD integrated white LED (QD-WLED) can be calculated when the necessary number of blue photons (S_{b1}) pumping QDs is found given the number of photons (per unit time) in all of the color components in the final white light spectrum, i.e., blue (S_b), green (S_g), yellow (S_y) and red (S_r). The calculation of S_{b1} depends on the architecture of QD-WLED. The methodology to calculate this quantity will be explained in the coming sections. In order to find the power conversion efficiency of QD-WLED, the number of the photons coming out of the blue LED (S_{b1}) should be compared with a real blue LED. For this purpose, we use the information of the blue LED given in Ref. 98, whose power conversion efficiency is 81.3%. This means given an electrical power (P_{elec}) of 1 W, this LED will radiate with an optical power (P_{opt}) of 813 mW. Now, we have to relate this optical power to the number of photons as in Eq. (5.5):

$$P_{opt} = \gamma \int S_{b1} g_{LED}\ \lambda_b, \Delta\lambda_b\ d\lambda \qquad \textbf{(5.5)}$$

where $g_{LED}(\lambda_b,\Delta\lambda_b)$ represents a normalized Gaussian function centered at the peak of blue LED with a given full-width-at-half maximum ($\Delta\lambda_b$) for a single photon. Thus, γ (the normalization factor) turns out to be as in Equation (5.6):

$$\gamma = \frac{P_{opt}}{\int S_{b1} g_{LED}\ \lambda_b, \Delta\lambda_b\ d\lambda} \qquad \textbf{(5.6)}$$

As a result, the number of photons for all of the color components scaled with respect to the real LED is given by Equations (5.7)-(5.10):

$$S_{b,\,final} = \gamma S_b \qquad \textbf{(5.7)}$$

$$S_{g,\,final} = \gamma S_g \qquad \textbf{(5.8)}$$

$$S_{y,\,final} = \gamma S_y \qquad \textbf{(5.9)}$$

$$S_{r,\,final} = \gamma S_r \qquad \textbf{(5.10)}$$

where $g(\lambda_i,\Delta\lambda_i)$ is a normalized Gaussian function centered at the wavelength λ_i and having a full-width at half-maximum of $\Delta\lambda_i$ containing a single photon of color i. Then, the resulting spectral power distribution of white emission is given in Equation (5.11):

$$s(\lambda) = S_{b,final}\, g(\lambda_b, \Delta_b) + S_{g,final}\, g(\lambda_g, \Delta_g) + S_{y,final}\, g(\lambda_y, \Delta_y) + S_{r,final}\, g(\lambda_r, \Delta_r) \quad \textbf{(5.11)}$$

As a result, the power conversion efficiency (PCE) is given by Equation (5.12).

$$PCE = \frac{\int s(\lambda)\, d\lambda}{P_{elec}} \quad \textbf{(5.12)}$$

Finally, the luminous efficiency (LE) is equivalent to the product of power conversion efficiency and luminous efficacy of optical radiation (LER), as given in Equation (5.13):

$$LE = PCE \times LER \quad \textbf{(5.13)}$$

5.3.1.1 Computational Modeling of Architectures

In this work, PCEs of two different QD-WLED architectures are computed. The first architecture consists of red, yellow and green QD layers from bottom to top on a blue LED chip (*A*). The second one models the film made of a QD blend. In addition, we modeled a third architecture by reversing the order of QD layers in *A* (A_{rev}) to compare with the original architecture (*A*) and the second basic one (*B*). However, it was obvious from the beginning that this structure will perform worse as a consequence of increasing photon transfer to other QD layers due to the order of QD layers.

5.3.1.2 Modeling the Architecture *A*

In *A* (and A_{rev}) c_1, c_2 and c_3 stand for the fraction of blue photons absorbed by green, yellow and red QDs, respectively. c_4 and c_5 denote the fraction of green photons absorbed by yellow and red QDs, respectively, whereas absorbed fraction of yellow photons within the red layer is expressed as c_6. By using the approximations stated in previous sections, c_4, c_5 and c_6 can be related to c_2 and c_3 as in Equations (5.14)-(5.16).

$$c_4 \approx 1 - \left(1 - c_2\right)^{\frac{\alpha_y(\lambda_g)}{\alpha_y(\lambda_b)}} \qquad \textbf{(5.14)}$$

$$c_5 \approx 1 - \left(1 - c_3\right)^{\frac{\alpha_r(\lambda_g)}{\alpha_r(\lambda_b)}} \qquad \textbf{(5.15)}$$

$$c_6 \approx 1 - \left(1 - c_3\right)^{\frac{\alpha_r(\lambda_y)}{\alpha_r(\lambda_b)}} \qquad \textbf{(5.16)}$$

where $\alpha_i(\lambda_j)$ stands for the absorption coefficient of QD layer of color *i* at the peak emission wavelength of Gaussian function emitting in color *j*. It is observed that this assumption does not yield an important deviation from the exact value; additionally, it provides simplicity in calculations and speed in numerical solutions of the equations by avoiding us dealing with broadband spectra. Having four equations that include our known parameters (i.e., S_b, S_g, S_y and S_r) gives us enough information to find S_{b1}, c_1, c_2 and c_3.

The self-absorption (SA) fractions are also included in the calculations; however, their mathematical formulation is not as simple as the previous ones. The calculation of SA depends on the architecture, the emission wavelength of absorbing QDs, the wavelength of the absorbed photons, and the pathway of the generated photon (for example, yellow photons generated as a result the absorption of blue and green photons have different photon self-absorbing fractions). In all of the architectures, c' denotes the fraction of self-absorbed photons when propagating upwards whereas c''_a denotes the self-absorbed fraction of downwards emitted photons. Additionally, c''_b expresses the fraction of self-absorbed photons while propagating upwards after the reflection of

downwards emitted photons. It is here worth mentioning that if all these phenomena are calculated by taking a single photon into account, then all these aforementioned fractions actually should be thought as probabilities.

Following the absorption of a photon by a QD layer in *A*, a new photon is generated and emitted upwards with a probability of *k* (1/2) and downwards with a probability of *1-k* (1/2). Self-absorption of photons occurs within the same QD layer, in which they are emitted, with a probability of c'. These photons might be reemitted with a probability of η and lost with a probability of $1-\eta$ due to non-radiative recombination. Upwards emitted photons, which are not absorbed by the same QD layer, leave the device. On the other hand, downwards emitted photons are absorbed within the same QD layer with a probability of c''_a, these photons are reemitted with a probability of η and lost with a probability of $1-\eta$. Photons survived from SA might transfer their energies to other QD layers with a probability of c_t. Upon the reflection of the survived photons from the bottom mirror, there is again a probability of c_t to be absorbed by other QD layers. The remaining photons have a probability of c_b'' being absorbed within the same layer that they are emitted. The probabilities of reemission and being lost are η and $1-\eta$, respectively. Finally, photons, which survived from SA, leave the device with a probability of $1-c_b''$. These photon transfer processes are illustrated in Figure 5.10.

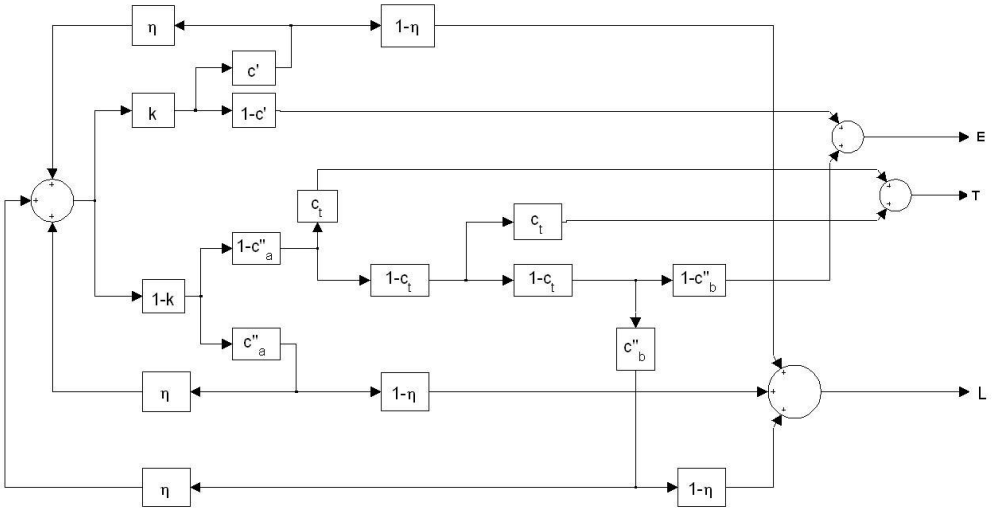

Figure 5.10 Illustration of optical mechanisms using system box model for architecture *A*.

The probabilities of extraction (E), of being transferred to other QD layers (T) and of being lost because of SA (L) can be found by solving Equations (5.17)-(5.19), which are found using the system box model given in Figure 5.10.

$$E = \frac{k\ (1-c')\ +\ (1-k)\ (1-c_a")\ (1-c_t)^2(1-c_b")}{1-kc'\eta-(1-k)c_a"\eta-(1-k)(1-c_a")\ (1-c_t)^2c_b"\eta} \quad \textbf{(5.17)}$$

$$T = \frac{(1-k)\ (1-c_a")c_t[1+(1-c_t)]}{1-kc'\eta-(1-k)c_a"\eta-(1-k)(1-c_a")\ (1-c_t)^2c_b"\eta} \quad \textbf{(5.18)}$$

$$L = \frac{(1-\eta)[kc'+\ (1-k)\ (1-c_a")(1-c_t)^2c_b"+\ (1-k)\ c_a"]}{1-kc'\eta-(1-k)c_a"\eta-(1-k)(1-c_a")\ (1-c_t)^2c_b"\eta} \quad \textbf{(5.19)}$$

SA probabilities for photons in a QD layer of color *m* with an excitation path of *j* are given in Equations (5.20)-(5.22). The bottom of this QD layer corresponds to *z=0*, and its film thickness is z_m.

$$c'_{mj} = \int_0^{z_m} d_{mj}\ \ z\ \ (1-e^{-\alpha_m\ \lambda_m\ \ z_m - z})dz \qquad \textbf{(5.20)}$$

$$c"_{mja} = \int_0^{z_m} d_{mj}\ \ z\ \ (1-e^{-\alpha_m\ \lambda_m\ z})dz \qquad \textbf{(5.21)}$$

$$c"_{mjb} = 1-e^{-\alpha_m\ \lambda_m\ z_m} \qquad \textbf{(5.22)}$$

where $d_{mj}(z)$ is the normalized excitation profile and correspondingly generated photon distribution due to this excitation within the QD layer. The normalization is carried out such that the integral between $z=0$ and $z=z_m$ is unity. Green, yellow and red photons generated by the excitation of blue photons have a distribution of $d_{g0}(z)$, $d_{y0}(z)$ and $d_{r0}(z)$ within green, yellow and red QD layers, respectively. The distribution of yellow and red photons within yellow and red QD layers pumped by the green photons are given by $d_{yg}(z)$ and $d_{rg}(z)$, respectively. The distribution of blue photons within green, yellow and red QD layers are given in Equation (5.23), where m stands for green (g), yellow (y) or red (r) QDs. κ_{m0} is the normalization coefficient and λ_b is the peak emission wavelength of blue LED. Since blue photons pump QDs from bottom, the number of photons decays exponentially. Consequently, QDs excited by blue LED generate photons with the same distribution. Therefore, Equation (5.23) actually formulates the normalized distribution for photons of color m generated by the excitation of blue photons within the QDs emitting in color m.

$$d_{m0}\ z = \kappa_{m0} e^{-\alpha_m \lambda_b z} e^{-\alpha_m \lambda_b z} \qquad \textbf{(5.23)}$$

The green photons are distributed within the yellow QD layer as given in Equation (5.24). κ_{yg} is the normalization coefficient, z_y is the thickness of the yellow QD layer, λ_g is the peak emission wavelength of green QDs and α_y is the absorption spectrum of yellow QDs. The first summand in Equation (5.24) is the distribution of downwards propagating photons, whereas the second one expresses the SA after the reflection from the bottom mirror.

$$\begin{aligned} d_{yg}\ z = \kappa_{yg}\{&[e^{-\alpha_y \lambda_g z_y - z} + 1-c_4\ \ 1-c_5{}^2 e^{-\alpha_y \lambda_g z}]e^{-\alpha_y \lambda_g z_y - z} \\ &+ 1-c_4\ \ 1-c_5{}^2 e^{-\alpha_y \lambda_g z}\} \end{aligned} \qquad \textbf{(5.24)}$$

The distribution of green photons within the red layer is expressed in Equation (5.25). κ_{rg} is the normalization coefficient, z_r is the thickness of the red QD layer, λ_g is the peak emission wavelength of the green QDs and α_r is the absorption spectrum of the red QDs. Similar to the distribution of green photons

within the yellow QDs, the first summand in Equation (5.25) stands for the absorption of downward emitted photons and second one corresponds to their self-absorption (SA) within the red QDs after being reflected from the bottom mirror.

$$d_{rg}\ \ z\ = \kappa_{rg}\{[e^{-\alpha_r\ \lambda_g\ \ z_r - z} + (1-c_5)e^{-\alpha_r\ \lambda_g\ z}]e^{-\alpha_r\ \lambda_g\ \ z_r - z} + (1-c_5)e^{-\alpha_r\ \lambda_g\ z}\} \textbf{(5.25)}$$

Finally, the distribution of the yellow photons within red layer is given in Equation (5.26). The same conventions are used, κ_{ry} stands for the normalization coefficient, z_r is the thickness of the red QD layer, λ_y and α_r denote the peak emission wavelength of the yellow QDs and the absorption spectrum of the red QDs, respectively. The first and second summands of Equation (5.26) express the same absorption mechanisms as in Equation (5.25), but this time yellow photons are absorbed instead of green photons.

$$d_{ry}\ \ z\ = \kappa_{ry}\{[e^{-\alpha_r\ \lambda_y\ \ z_r - z} + (1-c_6)e^{-\alpha_r\ \lambda_y\ z}]e^{-\alpha_r\ \lambda_y\ \ z_r - z} + (1-c_6)e^{-\alpha_r\ \lambda_y\ z}\} \textbf{(5.26)}$$

The photon transfer probabilities for green, yellow and red photons are formulated as given in Equations (5.27)-(5.29). Equation (5.27) denotes the absorption probability of green photons by the yellow and red QD layers and Equation (5.28) is the formulation for the probability of yellow photons to be absorbed by the red QD layer.

$$c_{tg} = c_4 + (1-c_4)(1-c_5)^2 c_4 + (1+c_4)c_5 + (1-c_4)(1-c_5)c_5 \textbf{(5.27)}$$

$$c_{ty} = c_6 + c_6(1-c_6) \textbf{(5.28)}$$

$$c_{tr} = 0 \textbf{(5.29)}$$

If the number of blue photons emitted from the blue LED chip is S_{b1}, then the number of generated green photons (S_{g0}) can be found using Equation (5.30) and the number of extracted photons (S_{gn}) turns out to be as given in Equation (5.31). Moreover, the number of yellow photons generated by blue (S_{y0}) and green (S_{yg0}) photons can be calculated using Equations (5.32) and (5.33), respectively. The number of extracted yellow photons is given by Equation (5.34). The number of

red photons pumped by blue photons (S_{r0}) is given in Equation (5.35), the number of red photons generated by green photons (S_{rg0}) is given in Equation (5.36), the number of red photons generated by yellow photons, which are generated through pumping of yellow QDs by blue (S_{ry0}) and green (S_{ryg0}) photons, are found using Equations (5.37) and (5.38), respectively. Finally, the number of extracted red and blue photons (S_{rn} and S_{bn}) are calculated using Equations (5.39) and (5.40), respectively.

$$S_{g0} = S_{b1} c_1 \ 1-c_2 \ \ 1-c_3 \ \eta_g \quad \textbf{(5.30)}$$

$$S_{gn} = S_{g0} E_{g0} \quad \textbf{(5.31)}$$

$$S_{y0} = S_{b1}(1-c_3) c_2 \eta_y \quad \textbf{(5.32)}$$

$$S_{yg0} = S_{g0} T_{g0} \frac{c_4 + \ 1-c_4 \ \ 1-c_5 \ ^2 c_4}{c_4 + (1-c_4) \ 1-c_5 \ ^2 c_4 + c_5 \ 1-c_4 \ + c_5 \ 1-c_4 \ \ 1-c_5} \eta_y \quad \textbf{(5.33)}$$

$$S_{yn} = S_{y0} E_{y0} + S_{yg0} E_{yg} \quad \textbf{(5.34)}$$

$$S_{r0} = S_{b1} c_3 \eta_r \quad \textbf{(5.35)}$$

$$S_{rg0} = S_{g0} T_{g0} \frac{c_5 \ 1-c_4 \ + c_5 \ 1-c_4 \ \ 1-c_5}{c_4 + (1-c_4) \ 1-c_5 \ ^2 c_4 + c_5 \ 1-c_4 \ + c_5 \ 1-c_4 \ \ 1-c_5} \eta_r \quad \textbf{(5.36)}$$

$$S_{ry0} = S_{y0} T_{y0} \eta_r \quad \textbf{(5.37)}$$

$$S_{ryg0} = S_{yg0} T_{yg} \eta_r \quad \textbf{(5.38)}$$

$$S_{rn} = S_{r0} E_{r0} + S_{rg0} E_{rg} + S_{ry0} E_{ry} + S_{ryg0} E_{ry} \quad \textbf{(5.39)}$$

$$S_{bn} = S_{b1} \ 1-c_1 \ \ 1-c_2 \ (1-c_3) \quad \textbf{(5.40)}$$

As S_{bn}, S_{gn}, S_{yn} and S_{rn} are known parameters, S_{b1} can be found using Equations (5.31), (5.34), (5.39) and (5.40); as a result, the PCE of a QD-WLED having the architecture *A* can be calculated.

5.3.1.3 Modeling the Architecture A_{rev}

Reversing the order of QDs does not change the main optical mechanisms; therefore, the mathematical notation does not change significantly. The only difference between A and A_{rev} is about the probability of photons transferred to other QD layers. In A, photons transfer occurs only during the downward emission (and after reflection from the bottom mirror). If the QD order is reversed, photons can transfer their energies to other QD layers only while propagating upwards. Corresponding optical mechanisms are illustrated in Figure 5.11 and equations defining the extraction (E), transfer (T) and loss (L) probabilities are given by Equations (5.41)-(5.43). The self-absorption probability equations are the same as in Equations (5.20)-(5.22).

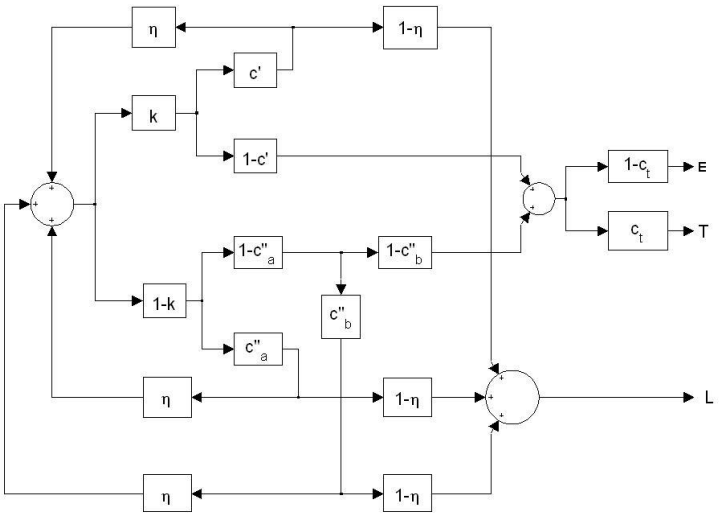

Figure 5.11 Illustration of optical mechanisms using system boxes for A_{rev}.

$$E = \frac{1-c_t \left[k\ 1-c'\ +\ 1-k\ \ 1-c_a"\ (1-c_b")\right]}{1-kc'\eta-(1-k)c_a"\eta-(1-k)(1-c_a")c_b"\eta} \quad \textbf{(5.41)}$$

$$T = \frac{c_t\left[k\ 1-c'\ +\ 1-k\ \ 1-c_a"\ (1-c_b")\right]}{1-kc'\eta-(1-k)c_a"\eta-(1-k)(1-c_a")c_b"\eta} \quad \textbf{(5.42)}$$

$$L = \frac{1-\eta\ \left[kc'+\ 1-k\ \ 1-c_a")c_b"+(1-k\ c_a"\right]}{1-kc'\eta-(1-k)c_a"\eta-(1-k)(1-c_a")c_b"\eta} \quad \textbf{(5.43)}$$

Because all of the pumping photons come to QDs from their bottom part (z=0), they experience an exponential decay as described in Equation (5.44).

$$d_{mj}\ \ z\ = \kappa_{mj} e^{-\alpha_m\ \lambda_j\ z} e^{-\alpha_m\ \lambda_j\ z} \quad \textbf{(5.44)}$$

where κ_{mj} is the normalization constant over the integral from z=0 to z=z_m. Furthermore, the transfer probability of green photons to other QD layers is $c_4+(1-c_4)c_5$, and the transfer probability of yellow photons to red QD layer is c_6. Finally, the transfer probability for red photons to another layer is taken as zero.

If the number of blue photons emitted from blue LED is given as S_{b1}, then the number of generated green photons (S_{g0}) becomes as in Equation (5.45) and the number of extracted green photons (S_{gn}) becomes as in Equation (5.46). Similarly, the number of yellow photons generated by blue (S_{y0}) and green (S_{yg0}) photons becomes as in Equations (5.47) and (5.48), respectively. The number of yellow photons being extracted is given in Equation (5.49). The number of red photons generated through the excitation of blue photons (S_{r0}) is given in Equation (5.50), the number of red photons generated by green photons (S_{rg0}) is expressed in Equation (5.51), the number of red photons generated by yellow photons, which are generated through pumping of yellow QDs by blue (S_{ry0}) and green (S_{ryg0}) photons, is formulated by Equations (5.51) and (5.52), respectively. Finally, the number of extracted red and blue photons (S_{rn} and S_{bn}) are presented in Equations (5.54) and (5.55), respectively.

$$S_{g0} = S_{b1} c_1 \eta_g \quad \textbf{(5.45)}$$

$$S_{gn} = S_{g0} E_{g0} \quad \textbf{(5.46)}$$

$$S_{y0} = S_{b1}(1-c_1)c_2\eta_y \quad \textbf{(5.47)}$$

$$S_{yg0} = S_{g0}T_{g0}\frac{c_4}{c_4 + \ 1-c_4 \ \ c_5}\eta_y \quad \textbf{(5.48)}$$

$$S_{yn} = S_{y0}E_{y0} + S_{yg0}E_{yg} \quad \textbf{(5.49)}$$

$$S_{r0} = S_{b1}(1-c_1)\ \ 1-c_2 \ \ c_3\eta_r \quad \textbf{(5.50)}$$

$$S_{rg0} = S_{g0}T_{g0}\frac{c_5(1-c_4)}{c_4 + \ 1-c_4 \ \ c_5}\eta_r \quad \textbf{(5.51)}$$

$$S_{ry0} = S_{y0}T_{y0}\eta_r \quad \textbf{(5.52)}$$

$$S_{ryg0} = S_{yg0}T_{yg}\eta_r \quad \textbf{(5.53)}$$

$$S_{rn} = S_{r0}E_{r0} + S_{rg0}E_{rg} + S_{ry0}E_{ry} + S_{ryg0}E_{ry} \quad \textbf{(5.54)}$$

$$S_{bn} = S_{b1}\ \ 1-c_1 \ \ \ 1-c_2 \ \ (1-c_3) \quad \textbf{(5.55)}$$

Since S_{bn}, S_{gn}, S_{yn} and S_{rn} are known, the solutions of Equations (5.46), (5.49), (5.54) and (5.55) give us S_{b1} and the PCE of the simulated QD-WLED in case that the quantum efficiencies of the color-converting QDs are available.

5.3.1.4 Modeling the Architecture *B*

The absorption and emission within a film of QD-blend are different than the previous ones. In the previous architectures, photon transfer to other layers occurs during upward or downward emissions. However, in blends photon absorption occurs during both emission directions. Thus, we changed our notation regarding photon transfer by separating photon transfer probabilities to other type of QDs for upwards and downwards emission. Furthermore, the blend structure is modeled as infinitesimally thin columns of QDs as illustrated in Figure 5.9. All of these QD columns have the same thickness in z-direction, z_l, and the fractional QD densities are introduced to our formulations so that the fractions of green QDs (f_g), yellow QDs (f_y) and red QDs (f_r) sum up to unity. Then, a photon with a higher photon energy excites the QDs with a probability

scaled by the QD-fraction (*f*); therefore, photon transfer probabilities (or fractions) should be scaled accordingly.

The photon transfer mechanisms in the QD-blend are summarized as follows: Upon the absorption of a photon within any type of QD, the upwards and downwards emission probabilities of the generated photons are k (1/2) and $1\text{-}k$ (1/2), respectively. They are absorbed or survived (not absorbed) within the same type of QDs with probabilities of c' and $1\text{-}c'$. The reemission probability of the absorbed ones is η and thus $1\text{-}\eta$ denotes the probability of energy loss due to non-radiative recombination. The survived ones from the SA during upwards emission are subject to be transferred to other type of QDs with a probability of c_t'. The ones that are not transferred to other QDs leave the device with a probability of $1\text{-}c_t'$. Downwards emitted photons are also subject to SA, this time with a probability of c_a''; and these photons are either reemitted or lost with probabilities of η and $1\text{-}\eta$, respectively. Photons survived from SA are subject to being transferred to other QD layers during downwards emission with a probability of c_{ta}''. The ones, which are not transferred to other QDs and not self-absorbed by the same QD layer, are reflected back. These reflected photons can be self-absorbed with a probability of c_b''. The probabilities corresponding to reemission or being lost are again η and $1\text{-}\eta$, respectively. The probability that photons survive from SA is $1\text{-}c_b''$. These photons might be transferred to other QDs with a probability of c_{tb}''. The ones that are not transferred to other QDs are extracted from the device. This process has a probability of $1\text{-}c_{tb}''$. The mechanisms explained above are illustrated in Figure 5.12 using the system box approach.

The formulations for probabilities of photons being extracted (E), photons being transferred to other QDs (T) and photons being lost (L) are given in Equations (5.56)-(5.58).

$$E = \frac{k\ 1-c'\ (1-c_t')+\ 1-k\ \ 1-c_a''\ (1-c_{ta}'')(1-c_b'')(1-c_{tb}'')}{1-\eta[kc'+\ 1-k\ \ c_a''+(1-k)\ 1-c_a''\ (1-c_{ta}'')c_b'']} \textbf{(5.56)}$$

$$T = \frac{k\ 1-c'\ \ c_t'+\ 1-k\ \ (1-c_a'')c_{ta}''+\ 1-k\ \ (1-c_a'')(1-c_{ta}'')(1-c_b'')c_{tb}''}{1-\eta[kc'+\ 1-k\ \ c_a''+(1-k)\ 1-c_a''\ \ (1-c_{ta}'')c_b'']} \textbf{(5.57)}$$

$$L = \frac{(1-\eta)[kc'+\ 1-k\ \ (1-c_a'')(1-c_{ta}'')c_b''+\ 1-k\ \ c_a'']}{1-\eta[kc'+\ 1-k\ \ c_a''+(1-k)\ 1-c_a''\ \ (1-c_{ta}'')c_b'']} \textbf{(5.58)}$$

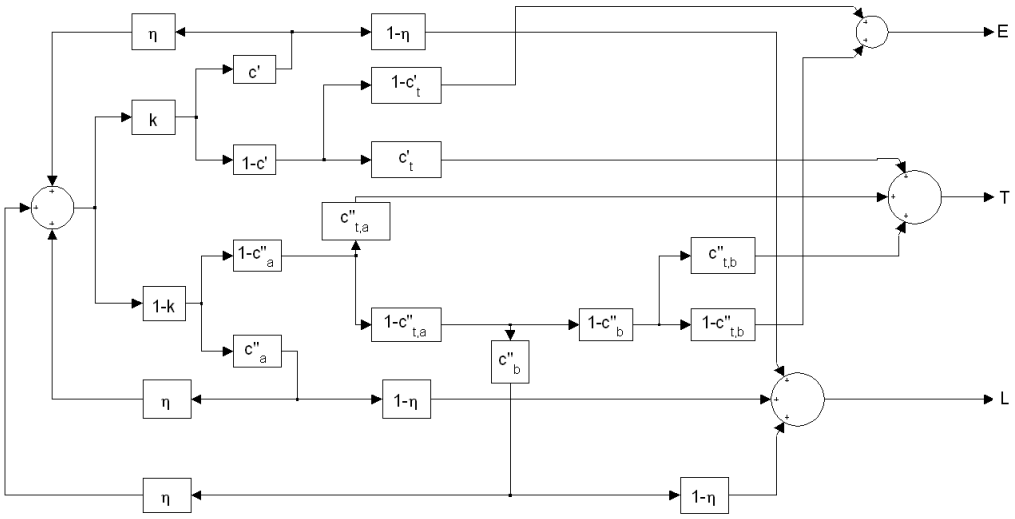

Figure 5.12 Illustration of optical mechanisms using system boxes for *B*.

The SA probabilities are given by Equations (5.59)-(5.61) for upwards and downwards (before and after reflection) emission, respectively.

$$c'_{mj} = \int_0^{z_l} f_m d_{mj}\ \ z\ \ (1-e^{-\alpha_m\ \lambda_m\ \ z_l - z})dz \qquad \textbf{(5.59)}$$

$$c''_{mja} = \int_0^{z_l} f_m d_{mj}\ \ z\ \ (1-e^{-\alpha_m\ \lambda_m\ z})dz \qquad \textbf{(5.60)}$$

$$c''_{mjb} = f_m(1-e^{-\alpha_m\ \lambda_m\ z_l}) \qquad \textbf{(5.61)}$$

where $d_{mj}(z)$ stands for the normalized distribution of photons over the integral from 0 to z_l. *m* denotes the color of the QDs; *g* for green, *y* for yellow and *r* for red QDs. *j* stands for the excitation path. The same nomenclature is followed as for *m*. In addition, here *0* means the excitation coming from the pump LED. For example, red QDs excited by yellow photons, which are generated through

absorption of the first blue photons in green QDs and then through the absorption of green photons in yellow QDs, are abbreviated as *yg0*. Then SA probability of upwards emission for this special case becomes c'_{ryg0}. Similarly, the distribution of blue photons within green, yellow and red QDs are denoted as $d_{g0}(z)$, $d_{y0}(z)$ and $d_{r0}(z)$, respectively. Yellow and red QDs excited by green photons have distribution functions of $d_{yg0}(z)$ and $d_{rg0}(z)$ within yellow and red QD layers, respectively. Finally, the distribution of yellow photons within red QDs are $d_{ryg0}(z)$ and $d_{ry0}(z)$. The first one describes the yellow photon distribution within red QDs when yellow photons are generated by the energy down-conversion of green photons in yellow QDs. The second one stands for the yellow photon distribution function within red QDs when yellow photons are generated by the wavelength up-conversion of blue photons in yellow QDs.

The normalized distribution functions of blue photons within green (*g*), yellow (*y*) and red (*r*) QDs are given by Equation (5.62), where *m* is *g*, *y* or *r*, κ_{m0} is the corresponding normalization coefficient over the integral between z=0 and $z=z_l$. Furthermore, λ_b is the peak emission wavelength of blue LED.

$$d_{m0}(z) = \kappa_{m0} e^{-\alpha_m \lambda_b z} e^{-\alpha_m \lambda_b z} \qquad \textbf{(5.62)}$$

The normalized distribution of green photons within yellow QDs is given by Equation (5.63) where κ_{yg0} is the normalization constant. This distribution depends on the distribution of green photons. Additionally, it contains the distribution of green photons in yellow QDs while propagating upwards and downwards, denoted in the first and second summands of Equation (5.63), respectively. Furthermore, it includes terms for the distribution of green photons within yellow QDs, which are not absorbed by green, yellow and red QDs during downward emission but absorbed in yellow QDs after the reflection from the bottom mirror, as expressed in the third, fourth and fifth summands of Equation (5.63), respectively.

$$d_{yg0}(z) = \kappa_{yg0} d_{g0}(z) \left[\begin{array}{l} \int_0^{z_l} f_y e^{-\alpha_y \lambda_g (z - z_i)} dz_i + \int_0^{z_l} f_y e^{-\alpha_y \lambda_g (z_i - z)} dz_i + \\ f_y e^{-\alpha_y \lambda_g z} \int_0^{z_l} f_g e^{-\alpha_g \lambda_g z_i} dz_i + \\ f_y e^{-\alpha_y \lambda_g z} \int_0^{z_l} f_y e^{-\alpha_y \lambda_g z_i} dz_i + f_y e^{-\alpha_y \lambda_g z} \int_0^{z_l} f_r e^{-\alpha_r \lambda_g z_i} dz_i \end{array} \right] \quad \textbf{(5.63)}$$

The normalized distribution of green photons within red QDs is very similar to the previous case and given in Equation (5.64), where κ_{rg0} is the normalization constant. As in the previous equation, this distribution is strongly dependent on the distribution of green photons. Furthermore, it contains the distribution of green photons absorbed in red QDs while propagating upwards and downwards, expressed in the first and second summands of Equation (5.64), respectively. In addition, the distribution of green photons within red QDs, which are not absorbed by green, yellow and red QDs during downward emission but absorbed in red QDs after reflection from the bottom of the device are expressed in the third, fourth and fifth summands of Equation (5.64).

$$d_{rg0}(z) = \kappa_{rg0} d_{g0}(z) \left[\begin{array}{l} \int_0^{z_l} f_r e^{-\alpha_r \lambda_g (z - z_i)} dz_i + \int_0^{z_l} f_r e^{-\alpha_r \lambda_g (z_i - z)} dz_i + \\ f_r e^{-\alpha_r \lambda_g z} \int_0^{z_l} f_g e^{-\alpha_g \lambda_g z_i} dz_i + f_r e^{-\alpha_r \lambda_g z} \int_0^{z_l} f_y e^{-\alpha_y \lambda_g z_i} dz_i + \\ f_r e^{-\alpha_r \lambda_g z} \int_0^{z_l} f_r e^{-\alpha_r \lambda_g z_i} dz_i \end{array} \right] \quad \textbf{(5.64)}$$

The distribution of yellow photons generated by the blue photons coming from the LED chip within red QDs has also a similar behavior, and it is given in Equation (5.65). Again κ_{ry0} is the normalization constant, and the distribution is scaled with $d_{y0}(z)$. It depends also on the distribution of yellow photons absorbed in red QDs while propagating upwards and downwards, as the first and second summands of Equation (5.65)present, respectively. In addition, the distribution function of yellow photons within red QDs, which are not absorbed by yellow and red QDs during downward emission but absorbed in red QDs after reflection

from the bottom of the device, are expressed in the third and fourth summands of Equation (5.65).

$$d_{ry0}\ \ z\ \ =\kappa_{ry0}d_{y0}\ \ z\ \left[\begin{array}{l}\int_0^{z_l} f_r e^{-\alpha_r\ \lambda_y\ (z-z_i)}dz_i+\int_0^{z_l} f_r e^{-\alpha_r\ \lambda_y\ (z_i-z)}dz_i+\\ f_r e^{-\alpha_r\ \lambda_y\ z}\int_0^{z_l} f_y e^{-\alpha_y\ \lambda_y\ z_i}dz_i+f_r e^{-\alpha_r\ \lambda_y\ z}\int_0^{z_l} f_r e^{-\alpha_r\ \lambda_y\ z_i}dz_i\end{array}\right] \textbf{(5.65)}$$

The distribution of yellow photons, which are generated through the pumping of yellow QDs by green photons, within red QDs is almost identical to Equation (5.66). In this case, the distribution is scaled by $d_{yg0}(z)$ instead of $d_{g0}(z)$ and a new normalization coefficient, κ_{ryg0}, is introduced. The final form of the expression is given in Equation (5.66).

$$d_{ryg0}\ \ z\ \ =\kappa_{ryg0}d_{yg0}\ \ z\ \left[\begin{array}{l}\int_0^{z_l} f_r e^{-\alpha_r\ \lambda_y\ (z-z_i)}dz_i+\int_0^{z_l} f_r e^{-\alpha_r\ \lambda_y\ (z_i-z)}dz_i+\\ f_r e^{-\alpha_r\ \lambda_y\ z}\int_0^{z_l} f_y e^{-\alpha_y\ \lambda_y\ z_i}dz_i+f_r e^{-\alpha_r\ \lambda_y\ z}\int_0^{z_l} f_r e^{-\alpha_r\ \lambda_y\ z_i}dz_i\end{array}\right] \textbf{(5.66)}$$

The photons emitted by the green QDs can be absorbed by yellow and green QDs. These photon transfer probabilities for upwards emission, and downward emission before and after the reflection from the bottom of the device are given in Equations (5.67)-(5.69), respectively.

$$c'_{tg0}=\int_0^{z_l} d_{g0}\ \ z\ \ f_y(1-e^{-\alpha_y\ \lambda_g\ (z_l-z)})dz+\int_0^{z_l} d_{g0}\ \ z\ \ f_r(1-e^{-\alpha_r\ \lambda_g\ (z_l-z)})dz \textbf{(5.67)}$$

$$c''_{tg0a}=\int_0^{z_l} d_{g0}\ \ z\ \ f_y(1-e^{-\alpha_y\ \lambda_g\ z})dz+\int_0^{z_l} d_{g0}\ \ z\ \ f_r(1-e^{-\alpha_r\ \lambda_g\ z})dz \textbf{(5.68)}$$

$$c''_{tg0b}=f_r\ \ 1-e^{-\alpha_r\ \lambda_g\ z_l}\ \ +f_y(1-e^{-\alpha_r\ \lambda_y\ z_l}) \textbf{(5.69)}$$

The yellow photons can be transferred to red QDs as well. These transfer probabilities for upwards propagating, downwards propagating (before and after the reflection) from the bottom mirror are given in Equations (5.70)-(5.72) for the case of yellow QDs pumped by the blue photons and in Equations (5.73)-

(5.75) for the case of yellow QDs pumped by green photons. Finally, it should be noted that all the transfer probabilities of red photons are zero.

$$c'_{ty0} = \int_0^{z_l} d_{y0}\ \ z\ \ f_r(1-e^{-\alpha_r\ \lambda_y\ (z_l - z)})dz \qquad \textbf{(5.70)}$$

$$c''_{ty0a} = \int_0^{z_l} d_{y0}\ \ z\ \ f_r(1-e^{-\alpha_r\ \lambda_y\ z})dz \qquad \textbf{(5.71)}$$

$$c''_{ty0b} = f_r\ \ 1-e^{-\alpha_r\ \lambda_y\ z_l} \qquad \textbf{(5.72)}$$

$$c'_{tyg0} = \int_0^{z_l} d_{yg0}\ \ z\ \ f_r(1-e^{-\alpha_r\ \lambda_y\ (z_l - z)})dz \qquad \textbf{(5.73)}$$

$$c''_{tyg0a} = \int_0^{z_l} d_{yg0}\ \ z\ \ f_r(1-e^{-\alpha_r\ \lambda_y\ z})dz \qquad \textbf{(5.74)}$$

$$c''_{tyg0b} = f_r\ \ 1-e^{-\alpha_r\ \lambda_y\ z_l} \qquad \textbf{(5.75)}$$

Before expressing the equations of final photon numbers, finding the ratio of the green photons being transferred to yellow (t_y) and red (t_r) QDs to the total fraction of transferred green photons will make equations easier to follow. Those expressions are given in Equations (5.76) and (5.77), respectively.

$$t_y = \frac{k\ \ 1-c'\ \ c'_y + 1-k\ \ \ 1-c''_a\ \ c''_y + 1-k\ \ \ 1-c''_a\ \ \ 1-c''_{ta}\ \ \ 1-c''_b\ \ c''_{yb}}{k\ \ 1-c'\ \ (c'_y + c'_r) + 1-k\ \ \ 1-c''_a\ \ (c''_y + c''_r) + 1-k\ \ \ 1-c''_a\ \ \ 1-c''_{ta}\ \ \ 1-c''_b\ \ (c''_{yb} + c''_{rb})} \qquad \textbf{(5.76)}$$

$$t_r = 1 - t_y \qquad \textbf{(5.77)}$$

where c_y' and c_r' denote the absorption probability of green photons by yellow and red QDs during upward emission, respectively. c_y'' and c_r'' are the probabilities of photon transfer to yellow and red QDs during downward emission before getting reflected from the bottom of the device, respectively. The probabilities for both type of QDs after the reflection become c''_{yb} and c''_{rb}. Expressions for these probabilities are given in Equations (5.78)-(5.83).

$$c'_y = \int_0^{z_l} d_{g0}\ \ z\ \ f_y(1-e^{-\alpha_y\ \lambda_g\ \ z_l - z})dz \qquad \textbf{(5.78)}$$

$$c''_{y} = \int_{0}^{z_l} d_{g0}\ z\ f_y(1-e^{-\alpha_y\ \lambda_g\ z})dz \qquad \textbf{(5.79)}$$

$$c''_{yb} = f_y(1-e^{-\alpha_y\ \lambda_g\ z_l}) \qquad \textbf{(5.80)}$$

$$c'_{r} = \int_{0}^{z_l} d_{g0}\ z\ f_r(1-e^{-\alpha_r\ \lambda_g\ z_l - z})dz \qquad \textbf{(5.81)}$$

$$c''_{r} = \int_{0}^{z_l} d_{g0}\ z\ f_r(1-e^{-\alpha_r\ \lambda_g\ z})dz \qquad \textbf{(5.82)}$$

$$c''_{rb} = f_y(1-e^{-\alpha_r\ \lambda_g\ z_l}) \qquad \textbf{(5.83)}$$

The number of generated green, yellow and red photons by blue photons (S_{g0}, S_{y0}, S_{r0}) are given in Equations (5.84)-(5.86) and the number of green photons being extracted (S_{gn}) is given in Equation (5.87). Then, the number of yellow and red photons generated by green photons (S_{yg0} and S_{rg0}) can be found using the Equations (5.88) and (5.89), respectively. The number of yellow photons that successfully out-couple (S_{yn}) can be found using Equation (5.90). Furthermore, the number of red photons generated by yellow photons, which are generated through excitation of yellow QDs by blue (S_{ry0}) and green (S_{ryg0}) photons, are given in Equations (5.91) and (5.92), respectively. Finally the number of red and blue photons that are out coupled (S_{rn} and S_{bn}) are given in Equations (5.93) and (5.94), respectively.

$$S_{g0} = S_{b1} f_g\ \ 1-e^{-\alpha_g\ \lambda_b\ z_l}\ \ \eta_g \qquad \textbf{(5.84)}$$

$$S_{y0} = S_{b1} f_y\ \ 1-e^{-\alpha_y\ \lambda_b\ z_l}\ \ \eta_y \qquad \textbf{(5.85)}$$

$$S_{r0} = S_{b1} f_r\ \ 1-e^{-\alpha_r\ \lambda_b\ z_l}\ \ \eta_r \qquad \textbf{(5.86)}$$

$$S_{gn} = S_{g0} E_{g0} \qquad \textbf{(5.87)}$$

$$S_{yg0} = \eta_y S_{g0} T_{g0} t_y \qquad \textbf{(5.88)}$$

$$S_{rg0} = \eta_r S_{g0} T_{g0} t_r \qquad \textbf{(5.89)}$$

$$S_{yn} = S_{y0} E_{y0} + S_{yg0} E_{yg0} \qquad \textbf{(5.90)}$$

$$S_{ry0} = S_{y0} T_{y0} \eta_r \qquad \textbf{(5.91)}$$

$$S_{ryg0} = S_{yg0} T_{yg0} \eta_r \quad \textbf{(5.92)}$$

$$S_{rn} = S_{r0} E_{r0} + S_{rg0} E_{rg0} + S_{ry0} E_{ry0} + S_{ryg0} E_{ryg0} \quad \textbf{(5.93)}$$

$$S_{bn} = S_{b1} \left[f_g e^{-\alpha_g \lambda_b z_l} + f_y e^{-\alpha_y \lambda_b z_l} + f_r e^{-\alpha_r \lambda_b z_l} \right] \quad \textbf{(5.94)}$$

Since S_{bn}, S_{gn}, S_{yn} and S_{rn} are known, by solving Equations (5.87), (5.90), (5.93) and (5.94) for S_{b1}, the power conversion efficiency of QD-WLED can be calculated given the quantum efficiencies of QDs (η).

5.3.2 Analyses

We start our analyses with PCE and LE for the ideal case of 100% quantum efficiency (η) of QDs. As given in Table 5.3, only the Stoke's shift causes a loss of at least 15% of the optical power for the photometrically efficient spectra satisfying CRI $\geq$ 90 and LER $\geq$ 380 lm/W_{opt} in all of the architectures. This corresponds to a maximum LE of 326.6 lm/W_{elect}. If a realistic blue LED having a reported PCE of 81.3% is taken into account, the maximum achievable PCE drops to 69% and the maximum LE decreases to 265.5 lm/W_{elect}. These results show that QD-WLEDs have the potential to surpass the ultra-efficiency limitations stated in Ref. 83 in case that high extraction efficiencies and high PCE of blue LEDs are realized.

	max.	min.	aver.	st. dev.
PCE (%) (excluding PCE of blue LED)	84.9	78.4	81.6	1.2
LE (lm/W_{elect}) (including PCE of blue LED)	265.5	242.3	254.2	4.1

Table 5.3 Maximum, minimum, average and standard deviation of PCE (excluding PCE of blue LED) and LE (including PCE of blue LED) for the photometrically efficient spectra.

A further investigation is carried out for finding out the effect of color conversion architectures and quantum efficiencies on LE. Here we fixed the quantum efficiencies of the two QD-WLED architectures and then computed their corresponding LEs and PCEs (Table 5.4 and 5.5). We found out that the layered QDs in architecture *A* perform better compared to the blend of QDs in architecture *B*. Furthermore, LE and PCE are observed to have very narrow standard deviation for photometrically efficient spectra considered in these models. In addition, we observed that the self-absorption (SA) of the photons (for example, absorption of green photons by green QDs) increases the standard deviation of both LE and PCE. Moreover, reversing the order of the QD layers in *A* results in a worse performance compared to *A* and *B*.

Architecture	η = 80 %				η = 50 %				η = 20 %			
	max.	min.	aver.	st. dev.	max.	min.	aver.	st. dev.	max.	min.	aver.	st. dev
A without SA	213.1	190.5	201.6	4.1	133.9	116.3	124.0	3.3	53.7	44.8	48.6	1.6
A with SA	209.4	182.7	195.3	4.9	127.2	99.3	112.3	5.2	48.3	30.3	38.7	3.5
B	203.6	176.7	188.8	4.9	115.3	93.2	102.1	4.0	38.7	29.4	33.6	1.6
A without SA – *A* w. SA	12.2	2.8	6.4	1.9	21.3	5.3	11.7	3.6	16.7	4.2	9.9	2.9
A w. SA – B	9.9	3.5	6.5	1.1	16.0	3.5	10.2	2.6	12.4	0.2	5.1	2.7

Table 5.4 Maximum, minimum, average and standard deviation of LE (including PCE of blue LED) in lm/W_{elect} for the photometrically efficient spectra at QD's η = 80%, 50% and 20% for two different architectures: *A* and *B*. The effect of self-absorption (SA) is also investigated for architecture *A*.

Architecture	η = 80 %				η = 50 %				η = 20 %			
	max	min	aver	st. dev	max	min	aver	st. dev	max	min	aver	st. dev
A without SA	68.4	61.7	64.7	1.2	42.9	37.4	39.8	1.0	17.2	14.4	15.6	0.5
A w. SA	67.3	59.0	62.7	1.5	41.1	31.9	36.0	1.7	15.6	9.7	12.4	1.1
B	65.2	57.1	60.6	1.5	37.2	30.0	32.8	1.3	12.4	9.4	10.8	0.5
A without SA - A w. SA	3.8	0.9	2.0	0.6	6.6	1.7	3.7	1.1	5.3	1.3	3.2	0.9
A w. SA – B	3.2	1.1	2.1	0.4	5.1	1.1	3.3	0.8	4.0	0.1	1.7	0.9

Table 5.5 Maximum, minimum, average and standard deviation of PCE (excluding PCE of blue LED) in percentages for the photometrically efficient spectra at η = 80%, 50% and 20% for two different architectures. The effect of self-absorption (SA) is also investigated for architecture *A*.

Another analysis has been carried out to find the minimum η values for limiting LEs (with PCE of the blue LED taken as 81.3%) assuming the same quantum efficiency for all of the QD layers. Our results showed that, to obtain

an LE of 100 lm/W_{elect}, the quantum efficiencies of QDs should be at least 39% and 44% in the color conversion film for *A* and *B*, respectively. In order to achieve an LE of 150 lm/W_{elect}, η should be at least 58% and 62% in the film for *A* and *B*, respectively. Increasing this LE limit to 200 lm/W_{elect}, increases the quantum efficiency limits to 76% and 78% in the film for *A* and *B*, respectively.

We further investigated the transfer of photons in *A* and *B* at η=100% and η=50%. The results are presented in Figure 5.13 and 5.14, respectively. When η=100%, most of the blue photons are absorbed within the red layer in both of the architectures. The second most absorbing layer for blue photons is the yellow QD layer in *A*. For the blend case, green and yellow QDs absorb almost the same number of blue photons. As opposed to blue photons, however, most of the green photons are extracted without being absorbed. When it comes to the transfer of the yellow photons, we find out that they are mostly extracted and a small amount is absorbed within red QDs. Moreover, the number of yellow photons transferred to red QD layer turns out to be higher in *B* compared to *A*. In the case of η=50% for *A*, no significant change occurs in photon transfer behaviors. An important point is that still ca. 50% of the green photons manage to leave the device in spite of the self-absorption. However, some changes occur in the transfer of blue and green photons within *B*. In this architecture, we observe that all of the transferred amounts of green photons are similar to each other as opposed to the case of η=100%. One interesting point is that most of the blue photons are transferred to yellow QDs in the case of η=50%; however, blue photons are absorbed mostly by the red QDs if η is 100%.

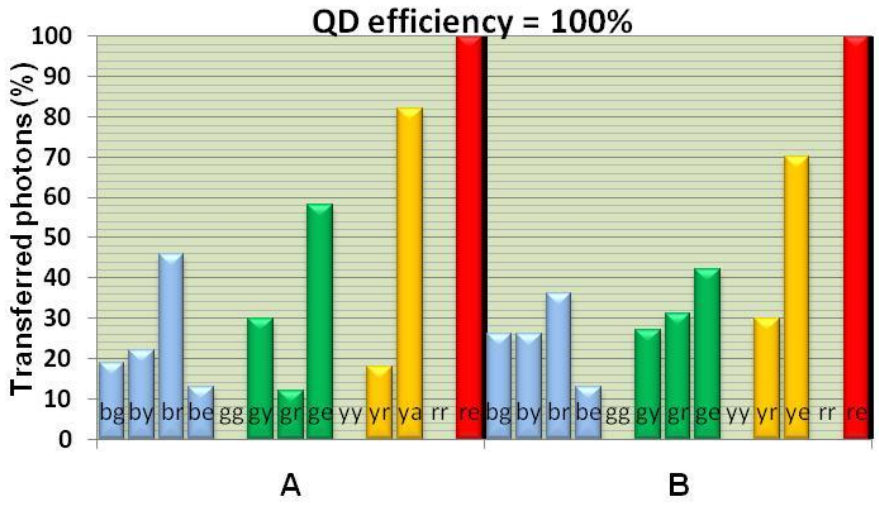

Figure 5.13 Fraction of blue photons transferred to green QDs (bg), to yellow QDs (by), to red QDs (br), and being extracted (be); fraction of green photons self-absorbed (gg), transferred to yellow QDs (gy), to red QDs (gr), and being extracted (ge); fraction of yellow photons self-absorbed (yy), transferred to red QDs (yr), and being extracted (ye); fraction of red photons self-absorbed (rr) and being extracted (re) in *A* and *B* at η=100%.

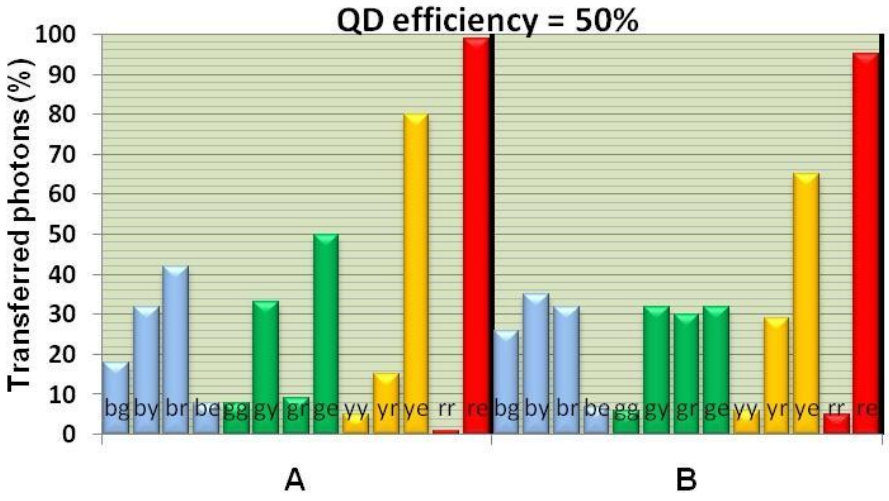

Figure 5.14 Fraction of blue photons transferred to green QDs (bg), to yellow QDs (by), to red QDs (br), and being extracted (be); fraction of green photons self-absorbed (gg), transferred to yellow QDs (gy), to red QDs (gr), and being extracted (ge); fraction of yellow photons self-absorbed (yy), transferred to red QDs (yr), and being extracted (ye); fraction of red photons self-absorbed (rr) and being extracted (re) in *A* and *B* at η=50%.

We investigated the effect of quantum efficiency change of QDs in different architectures. For this purpose, we fixed the efficiencies of two of the QD types and changed the efficiency of the remaining one between 20% and 100%. As test designs, spectra that lead to the highest PCE when three η values are equal

are selected. For η=100%, the red component effects PCE and LE of the device more severely compared to other components in all architectures. When η is fixed at 80%, PCE and LE beecome most sensitive to the efficiency changes of red QDs both in *A* and *B.* Fixing η at 50% does not change the behavior stated for η=80% case. Further decrease of η to 20% makes the change in QD efficiency of green layers to be the most effective one for both of the architectures.

We also investigated whether the change of the quantum efficiency affects the spectral content by calculating the average peak emission wavelength, full-width at half-maximum, and relative amplitudes of every color component of the spectra having PCE larger than the average of PCEs at that quantum efficiency. We did not observe any significant change in the spectral content as η changes. Corresponding values can be found in Table 5.6.

Architecture	η_{QD}	100%	80%	50%	20%
A	λ_b, λ_g, λ_y, λ_r *(nm)*	470.5, 531.6, 569.2, 620.3	469.9, 533.3, 570.0, 620.1	469.3, 530.4, 567.2, 620.2	469.9, 530.8, 568.1, 620.2
	$\Delta\lambda_b$, $\Delta\lambda_g$, $\Delta\lambda_y$, $\Delta\lambda_r$ *(nm)*	43.4, 41.6, 42.8, 33.4	42.8, 42.2, 43.2, 33.2	43.4, 39.9, 43.8, 33.2	44.2, 40.3, 43.3, 32.8
	a_b, a_g, a_y, a_r *(/1000)*	105.0, 215.3, 186.5,493.2	107.1, 214.1, 175.7, 503.1	106.0, 201.5, 196.9, 495.6	105.8, 207.2, 193.4, 493.6
B	λ_b, λ_g, λ_y, λ_r *(nm)*	470.5, 531.6, 569.2, 620.3	469.7, 534.1, 570.5, 620.0	469.0, 526.8, 563.3, 620.0	469.9, 531.1, 568.7, 620.3
	$\Delta\lambda_b$, $\Delta\lambda_g$, $\Delta\lambda_y$, $\Delta\lambda_r$ *(nm)*	43.4, 41.6, 42.8, 33.4	42.1, 42.9, 42.9, 33.4	41.9, 38.0, 45.3, 33.2	44.1, 40.6, 42.9, 32.9
	a_b, a_g, a_y, a_r *(/1000)*	105.0, 215.3, 186.5, 493.2	107.4, 216.1, 169.8, 506.8	106.1, 176.9, 220.2, 496.8	105.5, 211.6, 191.8, 491.2

Table 5.6 Average of the spectral parameters belonging to the computed spectra whose PCE is larger than the average of the PCEs of the photometrically efficient spectra in *A* and *B* at varying quantum efficiencies. λ_i: peak emission wavelength, $\Delta\lambda_i$: full-width at half-maximum, a_i: weight of the color component *i*. *i* is either blue (*b*), green (*g*), yellow (*y*) or red (*r*).

To verify the results of our computational model with real LEDs, we used the QD-WLED given in Ref. 11. This LED features an LE of 41 lm/W_{elect}. Our calculated LE result is ca. 75 lm/W_{elect}. This corresponds to an extraction efficiency of slightly larger than 50%, which is comparable to the extraction efficiencies of silicone encapsulated LEDs. As a result, this shows that our

modeling is in agreement with the performance of real devices and estimations based on these models are consistent proving the starting assumptions to make calculations possible are reasonable.

In conclusion, in this work we developed models to study the power conversion efficiency and luminous efficiency of QD integrated white LEDs. Using these models we investigated the effect of quantum efficiency change on PCE and LE. Furthermore, we found out that QD-WLEDs can be more efficient than phosphor based white LEDs both photometrically and electrically when high enough quantum efficiency of QDs and LEDs together with high extraction efficiencies are realized. In addition to these, we also found that placing red, yellow and green QD layers on blue LED (architecture *A*) is the most efficient one for color conversion QD-WLEDs compared to the QD blends (architecture *B*).

Chapter 6

Efficient White LEDs for Outdoor Lighting using Quantum Dot Nanophosphors

6.1 Spectral Recommendations for White Light Emitting Diodes with High Scotopic-to-Photopic Efficiency Ratio

This section is based in part on the publication "Computational analyses of white LEDs exhibiting high color rendition and high scotopic/photopic efficacy ratio for outdoor lighting applications" T. Erdem, S. Nizamoglu, X. W. Sun, and H. V. Demir, in submission.

The performance of white light generation can be photometrically evaluated by using different quantitative criteria. For the purpose of outdoor lighting, one of the most important figure-of-merits is the ratio of luminous efficacy of optical radiation in scotopic (dark adapted) vision to that of photopic (photon adapted) vision, the S/P ratio. This criterion takes into account the response of both rod and cone photoreceptors, which are responsible for scotopic and photopic modes, respectively. The difference between the photopic and scotopic vision results from the fact that the sensitivity of the human eye changes with the level of luminance. While the human eye is the most sensitive at 555 nm at high

luminance values (>5 cd/m^2), its sensitivity peak shifts to 507 nm at low luminance (<0.005cd/m^2) and rods begin to dominate the vision instead of cones [30]. This shift is called the Purkinje shift and S/P ratio signifies the effect of this shift in the human vision. The resulting value determines the capability of light source to provide better perceived brightness and better visual acuity [101]. Sources having higher S/P ratios provide better vision under low optical power levels compared to other sources with lower S/P ratios. Therefore, in the case that the optical power of two sources is the same, the one exhibiting higher S/P ratio yields better lighting. If we consider outdoor lighting in particular, we find out that it is technically (and economically) difficult to maintain high level of luminance at all points of targeted illumination area and that light sources with higher S/P ratios are thus of further importance for better illumination to enhance vision and road safety at night, effectively increasing the quality of life. Here we investigated S/P ratio performance for targeted levels higher than 2.50 so that we can achieve better performance than standard daylight source D65, which has an S/P ratio of 2.47, and those of typical white LEDs commonly below the S/P barrier of 2.50.

Another important indicator of high-quality white light generation is the color rendering property. A light source having high color rendering should reflect the real colors of illuminated objects as much as possible. The standard measure of this property is the color rendering index (CRI) developed by Commission Internationale de l'Eclairage (CIE). However, CRI has important shortcomings at cool correlated color temperatures (CCTs) in the case that the color of the white light source becomes bluish tint and CCT increases [7]. Since high S/P ratios require significant amount of blue-green color content to match the Purkinje shift, CCT increases and falls into cool white region while S/P ratio increases and CRI cannot be used as a measure of color rendering in this case. Instead, it is possible to use color quality scale (CQS), recently developed by Davis and Ohno [102], which determines the color rendering quality of light sources at all color temperatures. Because this metric takes the effect of high

CCTs into account, it relies on more test sources to give better rendering information and penalizes the sources for chromatic saturation. Furthermore, the computation method is similar to that of CRI; consequently, comparison and interpretation of the resulting values is conveniently straightforward. The highest possible value of CQS is set to 100, whereas the worst CQS is 0. Here we computationally investigated different cases of CQS for various targeted levels higher than 70, 80 and 90 to indicate correspondingly good to excellent levels of color rendering while keeping track of the evolution of S/P ratio, LER and CCT for the first time.

To satisfy high-quality lighting requirements, the emission spectra of light sources should be designed very carefully. For this purpose, combinations of narrow band emitters such as quantum dot nanophosphors (QDs) provide a great benefit of tuneability, one by which their white light sources can be precisely controlled to confer the luminous efficacy high while the color rendering is simultaneously made almost perfect [86,90]. In our previous work, we evaluated such photometric performance with high CRI and high LER at warm CCTs [90], which is for indoor lighting, excluding the study of S/P ratio and CQS unlike in this work. Here, different than the previous works of our group and others, specifically for outdoor lighting, we show that high S/P values (>2.50) can also be achieved in principle using these narrow band emitting nanoluminophors, while maintaining an excellent level of color rendering with high CQS (>90).

6.1.1 Computational Approach

The photometric performances of QD-WLEDs are evaluated from a computational point of view. The emission spectra of the narrow band emitters are modeled as a Gaussian function. Although the radiation of a monochromatic LED is not perfectly Gaussian, one can safely treat it as a Gaussian or sum of

Gaussians [83]. While generating white light, the critical point is that we need three or more color components to obtain superior photometric properties. In our numerical simulations, the blue peak emission wavelengths are examined in the range from 425 to 445 nm with a step size of 5 nm and 450 to 490 nm with a 10 nm step size. Green emission is modeled with peak emissions at 500, 505, 510, 530, 530 and 540 nm. Central wavelengths of yellow and red components are changed from 550 to 590 nm and from 600 to 640 nm, both with a step size of 10 nm, respectively. Furthermore, the full-width at half-maximum (FWHM) of each Gaussian is varied from 30 to 54 nm with a step size of 6 nm. Additionally, the amplitudes of each color component are altered between 0 and 4 units. Subsequently, normalization of the sum of amplitudes is carried out to compare their results with each other. Resultantly, 495,937,500 WLED designs are modeled and photometrically computed.

The luminous efficacy of optical radiation in photopic (LER) and scotopic (SLER) regimes, and their S/P ratio are computed using Equation (2.54). CQS levels are calculated as described in Chapter 2. The CCT values up to 21,000 K are obtained directly by calculating the temperature of the closest Planckian blackbody radiator in the (u,v) color space. To increase computation speed, CCTs larger than 21,000 K are computed using the approximation given in Ref. 92. To consider high S/P ratios, we limit our computational design pool only to the cases with S/P ratios larger than 2.50. Moreover, the cases of bad color rendering (CQS <70) and low luminous efficacy of optical radiation (LER <250 lm/W_{opt}) are excluded in our analyses. Furthermore, the analyses of CQS larger than 80 and 90 are separately studied to understand the spectral requirements for two separate restriction levels of high color rendering.

6.1.2 Computational Analyses

6.1.2.1 Input Independent Analysis

Our computations return only 2.7% of the generated designs that achieve CQS ≥70 together with the restrictions of S/P ≥2.50 and LER ≥250 lm/W_{opt}. Increasing the color rendering limit results in even fewer designs that surpass these restrictions. For the case of CQS ≥80, only 0.86% of the modeled designs satisfy the conditions. Increasing CQS limit further to 90 decreases this fraction down to 0.067%. All of these findings show that high-efficiency and good color rendering of a light source cannot be achieved by arbitrarily selecting the spectra; instead, the source spectrum needs to be carefully designed.

According to the simulation results, the highest CQS is found to be 98.28 together with an S/P ratio of 2.55, an LER of 281 lm/W_{opt} and a CCT of 6,991 K. For the case of CQS ≥ 70, the highest LER is obtained at 386 lm/W_{opt} (while S/P=2.51, CQS=70.24 and CCT=7,197 K). This value decreases to 359 lm/W_{opt} (while S/P=2.50, CQS=80.30 and CCT=6,928 K) for CQS ≥80. Further increasing CQS limit to 90 decreases the maximum possible LER down to 330 lm/W_{opt} (while S/P=2.51, CQS=90.39 and CCT=7,115 K). Another important criterion for high performance is the S/P ratio for our purposes. This metric also follows a decreasing trend upon increasing the CQS limit as in the case of LER. For CQS ≥70, the highest S/P ratio is 4.19 (while CQS=70.84, CCT=42,815 K and LER=252 lm/W_{opt}). When the CQS limit is set to 80, the highest possible S/P ratio decreases to 3.92 (while CQS=81.69, CCT=54,310 K and LER=250 lm/W_{opt}). When the CQS restriction is finally raised to 90, the highest possible S/P ratio drops to 3.57 (while CQS=90.27, CCT=38,527 K and LER=251 lm/W_{opt}). As another performance metric, CCT is investigated as well. The minimum CCT (corresponding to the warmest white light) is obtained at 2,728

K (while CQS=70.50, S/P=2.51 and LER=251 lm/W_{opt}) when CQS ≥ 70 limit is applied. Further raising CQS limit increases the minimum possible CCT. For CQS ≥80, the lowest CCT becomes 3,068 K (while CQS=80.81, S/P=2.50 and LER=250 lm/W_{opt}) and for CQS ≥ 90, this increases to 5,004 K (while CQS=90.80, S/P=2.50 and LER=264 lm/W_{opt}).

In this work, we also investigated the fundamental relation and tradeoffs between these photometric figure-of-merits. The investigated combinations of boundary performance includes LER *vs.* S/P ratio, CQS *vs.* S/P ratio, CQS *vs.* LER, CCT *vs.* LER, CCT *vs.* CQS and CCT *vs.* S/P ratio, which are shown in Figure 6.1(a)-(f), respectively. The relation of LER *vs.* S/P ratio is analyzed for three CQS restrictions, namely CQS ≥ 70, 80 and 90. As given in Figure 6.1(a), these boundaries follow a decreasing behavior, indicated by the three iso-CQS curves, each one corresponding to one of the CQS restriction levels that increase in order outwards. CQS *vs.* S/P ratio is presented in Figure 6.1(b). Investigation of the computational data building up the boundary performance reveals that this curve represents the tradeoff between CQS and S/P ratio up to S/P=3.20. After this value, however, it becomes an iso-LER curve, restricted to LER=250 lm/W_{opt} in this case. The relation of CQS *vs.* LER is given in Figure 6.1(c). This shows a fundamental tradeoff between CQS and LER up to LER=290 lm/W_{opt}. After this point, we observe a decreasing behavior corresponding to the iso-S/P ratio curve for S/P=2.50 restriction. Figure 6.1(d) shows the relationship between CCT and LER. This boundary performance graph exhibits an increasing trend, which is shaped by both CQS=70 and S/P=2.50 limitations. Figure 6.1(e) presents the relation of CCT *vs.* CQS. The investigation of their data shows that restrictions are effective until CQS=85, S/P=2.50 and LER=250 lm/W_{opt}. After this value, we observe an iso-S/P ratio curve corresponding to S/P=2.50. Finally, the behavior of CCT *vs.* S/P ratio is investigated, which is depicted in Figure 6.1(f). This relation has an increasing trend upon increasing S/P ratio because blue-green content increases in the spectrum for obtaining

high S/P ratio. Investigation of the corresponding data reveals that this curve is shaped by both CQS=70 and LER=250 lm/W_{opt} limitations.

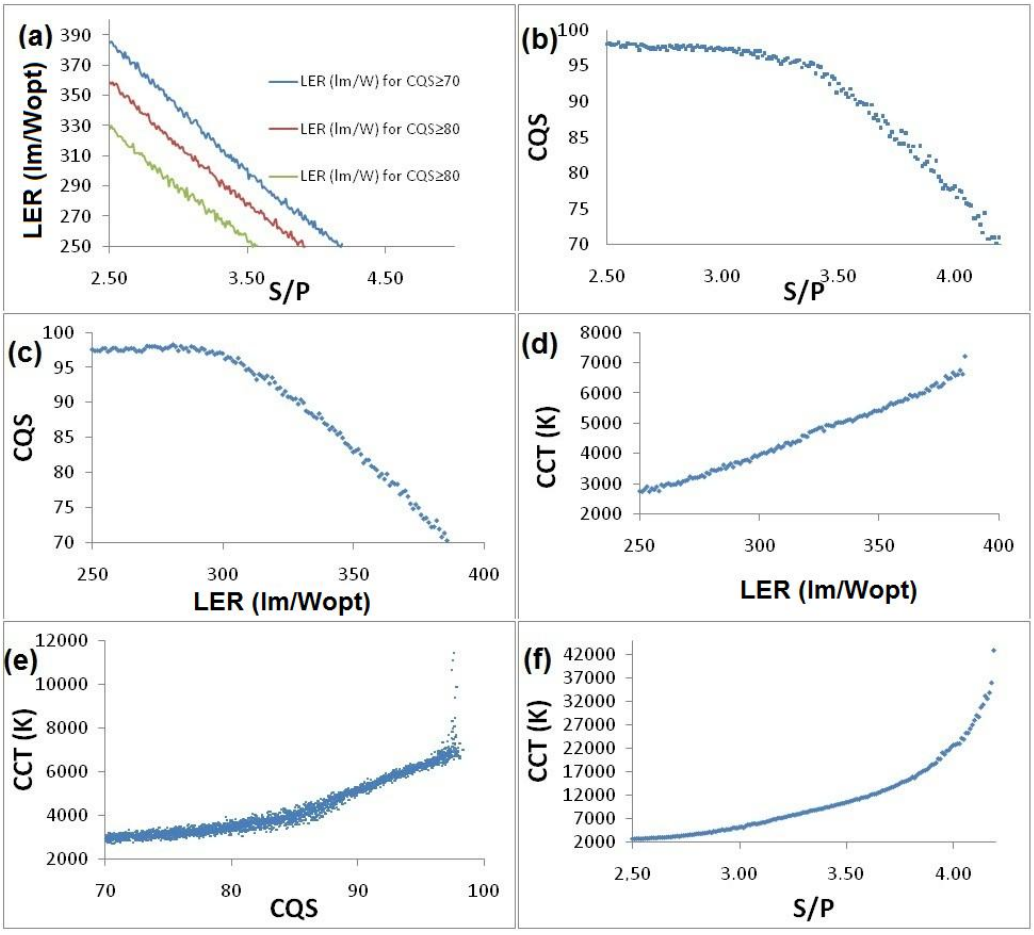

Figure 6.1 Relation and tradeoffs between (a) LER *vs.* S/P ratio, (b) CQS *vs.* S/P ratio, (c) CQS *vs.* LER, (d) CCT *vs.* LER, (e) CCT *vs.* CQS, and (f) CCT *vs.* S/P ratio.

6.1.2.2 Input Dependent Analysis

The input parameters, which we use for the generation of white light, are peak emission wavelengths, full-width at half-maximum (FWHM), and relative amplitudes for all four color components namely, blue, green, yellow and red. Here the analysis is carried out by investigating the average and standard deviation (stdev) of every input parameter. The results are separated into three groups. All of the groups satisfy S/P ratio ≥2.50 and LER ≥250 lm/W_{opt}. Their

difference comes from the distinct restrictions of CQS ≥70, 80 and 90. The resulting cases satisfying the corresponding conditions are summarized in Table 6.1.

		CQS ≥ 70		CQS ≥ 80		CQS ≥ 90	
Input Parameters	Colors	Average	Standard Deviation	Average	Standard Deviation	Average	Standard Deviation
Peak Emission Wavelength (nm)	Blue	451.06	13.75	449.66	11.29	447.69	7.78
	Green	513.09	11.35	512.98	11.17	509.69	9.07
	Yellow	566.55	14.15	565.34	13.41	564.86	11.23
	Red	621.82	13.24	623.33	11.93	625.47	9.94
FWHM (nm)	Blue	43.48	8.31	44.02	8.15	45.01	7.88
	Green	43.76	8.34	43.84	8.38	44.09	8.38
	Yellow	41.79	8.52	41.98	8.53	42.51	8.51
	Red	41.27	8.46	41.54	8.47	42.01	8.47
Relative Amplitude (/1000)	Blue	323.77	79.68	329.22	68.77	322.40	53.07
	Green	294.03	91.64	272.57	74.18	254.70	44.36
	Yellow	169.93	92.36	173.71	81.15	196.27	50.44
	Red	212.45	83.54	224.73	68.05	226.95	47.94

Table 6.1 Average and standard deviation of the input parameters satisfying the conditions S/P ratio ≥2.50, LER ≥250 lm/W_{opt} and CQS ≥70, 80 and 90.

6.1.2.2.1 Analysis of Peak Emission Wavelengths

As presented in Table 6.1, the emission wavelengths should be selected within a relatively narrow band for all of the color components and CQS limitations. For blue, the average wavelength comes out to be 451.06 nm with a stdev of 13.75 nm when CQS ≥70 restriction is applied. Increasing the CQS limitation to 90 results in narrowing the stdev to 7.78 nm and consequently a small blue-shift is observed in the average value from 451.06 to 447.69 nm. An almost identical behavior is observed for all of the other three color components. The average peak emission wavelengths shift from 513.09 nm, 566.55 nm and 621.82 nm to 509.69 nm, 564.86 nm and 625.47 nm upon application of CQS ≥90 limit, for green, yellow and red components, respectively. Following this blue-shift, the stdev values also become smaller for all of the color components. Conclusively,

we can state that the selection of peak emission wavelengths is important for obtaining good performance in outdoor lighting. From the fact that the shift of wavelengths is very small for stricter color rendering limitations, we can conclude that the choice of wavelengths is more effective on the S/P ratio and LER performance than on the CQS performance.

6.1.2.2.2 Analysis of FWHMs

According to Table 6.1, the design of FWHMs follows a different trend than that of peak emission wavelengths. As opposed to the previous case, investigation of the color components reveals that the FWHM values are not as critical for the generation of white light with high S/P ratio and good color rendering as the peak wavelengths (Table 6.1). For all of the color cases, the average FWHM values are around 43 nm. More importantly, the values of FWHMs can be selected within a relatively large interval as it can be understood from the large stdev values (around 8.1 nm) for all of the color components. In addition, we observe that stdev does not change significantly although CQS limit is made stricter. Furthermore, a very small increase in the FWHM is found out upon raising the color rendering limitation. Therefore, we can claim that the choice of FWHMs is not as effective within this range as other parameters for obtaining high optical performance as long as the peak emission wavelengths and relative amplitudes are set right.

6.1.2.2.3 Analysis of Relative Amplitudes

The analysis of the relative amplitudes gives important information about the requirements for high optical performance of outdoor lighting. As given in Table 6.1, the amplitude of the blue component should be selected around 323/1000. The decrease of the stdev from 79.68/1000 to 53.07/1000 for large CQS limit shows that obtaining good color rendition is strongly dependent on the choice of amplitude of blue component. We observe a similar behavior for other color components as well; stdev values decrease significantly in the case of higher

CQS. This finding shows that the choice of relative amplitude is very critical for good color rendition. Additionally, we observe some changes in the average values of relative amplitudes upon increasing CQS restriction. However, these changes are very small; as a result, we can recommend that the relative amplitudes should be chosen between 255/1000-290/1000, 170/1000-195/1000 and 210/1000-225/1000 for green, yellow and red color components to obtain high color rendering and high-efficiency in scotopic vision.

6.1.3 Spectral recommendations for highly efficient outdoor lighting using white LEDs

To make conclusive spectral recommendations for outdoor lighting, we examine the photometric performance of average spectra for every color rendering restriction. Corresponding spectral distributions can be found in Figure 6.2 and input parameters are given in Table 6.1. The average spectrum exhibits a color operating point (color chromaticity) at x=0.2866 and y=0.3108, and yields LER=284.21 lm/W_{opt}, S/P ratio=2.80, CQS=92.87 and CCT=8,506 K when CQS ≥70 limitation is applied. Increasing the CQS limitation to 80 changes the performance of the spectrum created using average values. The resulting figure-of-merits are LER=277.98 lm/W_{opt}, S/P ratio=2.74, CQS=94.50 and CCT=8,461 K. The corresponding color is located at x=0.2897 and y=0.3042 on the chromaticity diagram. Further increasing the CQS limit to 90 changes the coordinates of the color to x=0.2905 and y=0.2893. The resulting performance is LER=262.52 lm/W_{opt}, S/P ratio=2.80, CQS=95.63 and CCT=8,907 K. By comparing these three sets of performance, we can state that all of them lead to really good outdoor lighting. However, here we can accept the best performance is obtained with excellent color rendering of CQS ≥90, accompanied with high S/P ratio reaching 2.80. The corresponding wavelengths for this spectrum are 447.69, 509.69, 564.86, and 625.47 nm for blue, green, yellow, and red, respectively. The FWHM values are 45.01, 44.09, 42.51, and 42.01 nm; and

relative amplitudes are 322.40/1000, 254.70/1000, 196.27/1000, and 226.95/1000 from blue to red color components, respectively.

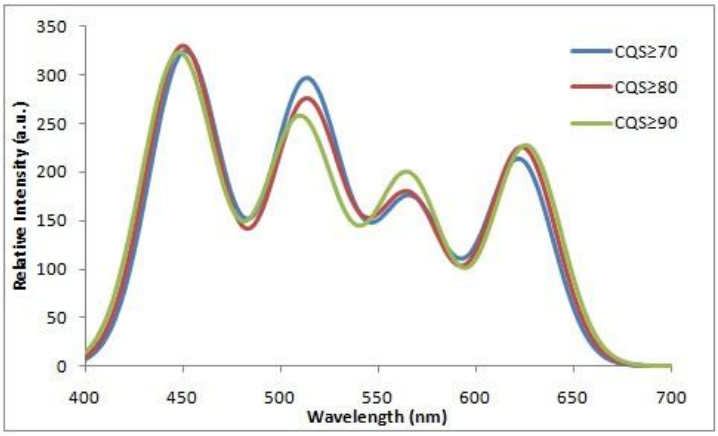

Figure 6.2 White LED designs with input parameters modeled for CQS ≥70, 80 and 90 restrictions in order. All of these WLED designs satisfy S/P ratio ≥2.50 and LER ≥250 lm/W$_{opt}$.

Here we presented the results of our computational analyses of white LEDs for outdoor lighting. High-quality lighting is critical for street lighting. This is important both for energy saving and safety issues. We demonstrated that high S/P >2.50 can be achieved in principle using narrow band emitting quantum dot nanoluminophors, while also reaching an excellent level of color rendering of CQS >90. Additionally, we studied and evaluated the relationship of S/P ratio, color quality scale, luminous efficiency of optical radiation and correlated color temperature with each other, by modeling and computing the photometric performance of over 495 million QD-LED designs. Moreover, we investigated the input requirements (peak emission wavelengths, FWHMs, and relative amplitudes) of high-quality white light generation for the purposes of outdoor lighting.

Finally, we provided spectral recommendations for color conversion LEDs using quantum dot nanoluminophors that exhibit almost perfect color rendition and an S/P ratio exceeding by far those of the standard daylight source (D65) and typical white LEDs. The results of this work might in general be applied to multichip white LEDs as well. Such high-quality LEDs that are specifically

designed for outdoor lighting are essential for future high-efficiency street lighting.

6.2 Experimental Demonstration of high S/P QD-WLEDs

There are still continuing debates on the implications of high S/P ratio. Regardless of these discussions, however, there have been no reports on a light source that achieves a high S/P ratio together with good color rendition properties. It is basically because of the trade-off between both of the performance metrics mentioned in the previous section. In this part of the thesis, we report the first demonstration of a QD-LED having a high S/P ratio and a relatively good color rendition [103]. The emission spectra of the common white light sources reveal S/P ratios between 0.80 to 2.50 [104]. An incandescent lamp, which has a CRI of 100, has an S/P ratio of 1.41 [103]. S/P ratios of phosphor based white LEDs vary between 1.68 and 2.38 [9,105].

To obtain a QD-LED having a high S/P ratio together with a reasonable CRI, our approach has been to mimic the blackbody radiator spectra having high color temperatures. Since blue and cyan color components raise the color temperatures and S/P ratios, we made use of a blue LED and QDs emitting in cyan. In addition, integration of green, yellow and red QDs are added as they help to obtain a good CRI.

The blue LED chip that we used is an InGaN/GaN quantum well based LED emitting at 452 nm. Furthermore, we used CdSe/ZnS core/shell QDs dissolved in toluene emitting at 490 (cyan), 540 (green), 580 (yellow) and 620 nm (red). We used 119.7 nmol of cyan, 4.652 nmol of green, 0.990 nmol of yellow and 0.158 nmol of red QDs in our QD-WLED. At 25 mA of current level, we

obtained white light emission corresponding to the chromaticity coordinates of (0.251,0.246) and a CRI of 71.7. The S/P of this device turned out to be 3.41 at CCT of 45,000 K. As CRI might give inaccurate information at the extreme CCTs, we evaluated the color rendition performance of the QD-LED using CQS, and this also gave a similar result, CQS=70.3. The emission spectrum of the device and the chromaticity point of this spectrum can be found in Figure 6.3 together with the photo of the light sources.

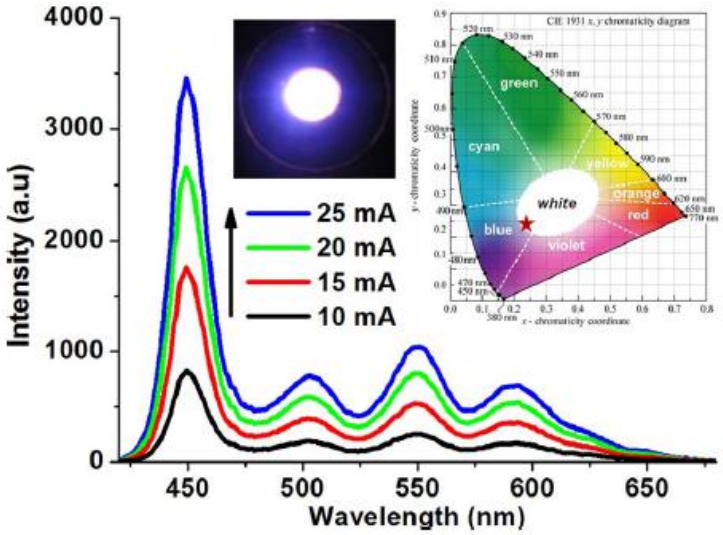

Figure 6.3 The emission spectra of the QD-LED and corresponding chromaticity point on CIE 1931 chromaticity diagram along with the photo of the QD-LED [103].

In summary, in this work we demonstrated a white QD-LED having a S/P ratio larger than the most commonly used light sources together with a reasonable color rendition performance for the first time.

6.3 Spectral Recommendations for White Light Emitting Diodes with High Mesopic Luminance

This section is based in part on the publication "Efficient street lighting with good color rendering using semiconductor quantum dot nanophosphors" T. Erdem, S. Nizamoglu, X. W. Sun, and H. V. Demir, in submission.

In this part of the thesis, we present a photometric study of color-conversion LEDs integrated with semiconductor nanophosphors of colloidal quantum dots (QDs) that enable higher luminance than those of conventional light sources in mesopic regimes given the road lighting standards in the US and the UK. Having worked with over 10 million designs, we have found that QD-LEDs can supply 15-20% better mesopic luminance than both cold white fluorescent lamp and high-pressure sodium lamps, while providing a color quality scale ≥80 at the same time. These QD-LEDs prove to be electrically more efficient than conventional sources provided that their power conversion efficiencies are ≥70-75%, depending on the luminance level standards. As stated by Raynham [106], the quality of the road lighting is evaluated using average luminance, overall and longitudinal uniformity of luminance, threshold increment, and surround ratio. Among these parameters, in this work we focus on the average luminance, which strongly depends on the materials chosen and spectra designed, whereas other quality parameters vary mostly during the luminary design and their large scale use.

6.3.1 Computational Approach

Designing light sources with high luminance and good color rendering requires careful spectral design. To this end, narrow light emitter combinations are desirable as they enable precise spectrum control. Because of their low energy consumption and narrow emission bandwidths, light emitting diodes (LEDs) are good candidates for this purpose. However, current commercial white LEDs use rare-earth ion based phosphors as their color conversion materials. Apart from raising concerns regarding their supply security [87], phosphors possess a very broad emission band; and more importantly, tuning their emission spectrum and achieving narrow bands is technically a very challenging task. On the other hand, using separate LED chips emitting different colors increases the cost of production tremendously although good spectral tuning can be realized. Furthermore, obtaining an efficient LED in green region is another important drawback of multi-chip systems [9]. Considering all of these limitations, colloidal semiconductor nanophosphors are the most appropriate material systems since their narrow emission bandwidths allow for good spectral tuning [90,93], and their quantum efficiency may exceed 90% in solution and 70% in film, which makes such QD integrated white LEDs (QD-WLEDs) promising candidates of next generation lighting systems [56], for both indoor and outdoor applications. The spectral requirements of QD-WLEDs for indoor applications have already been studied [90] and efficient devices have been demonstrated [93]. However, those for the outdoor lighting given varying levels of luminance (mesopic vision conditions) have not been studied to date.

The performance criteria for road lighting are different than the indoor case. As mentioned above, good quality road lighting requires high luminance in mesopic light levels, good color rendering and low energy consumption. In this part, we investigate the performance of QD-WLEDs for road lighting and investigate spectral requirements such that higher luminance can be obtained per

supplied optical power together with high color rendering performance. In our study, we compared the mesopic luminance performance of the designed QD-WLEDs with the conventional light sources including the standard daylight source D65, a cool white fluorescent lamp (CWFL), a blackbody radiator at 3,000K, a metal-halide lamp (MH), a high pressure sodium lamp (HPS), and a mercury vapor lamp (MV). Furthermore, we evaluated the color rendition performance of QD-WLEDs using color quality scale (CQS), which provides healthier results than color rendering index (CRI) for narrow emitters [17]. In our calculations, we excluded all of the designs having a CQS less than 80 to satisfy the condition of good color rendering.

6.3.1.1 Structure of spectral designs

To examine the efficiency of light sources in the mesopic region, we selected four photopic luminance levels so that road lighting standards in the USA [22] and the UK [23,24] are satisfied. We chose 0.50 cd/m^2 for freeway, collector and local road lighting according to the USA and link road standards for the UK. 0.80 cd/m^2 satisfies the US standards of express way and major road lighting, and the secondary distributor lighting standard of the UK. 1.25 cd/m^2 is chosen to fulfill the UK requirements for strategic route, major distributor, secondary distributor, and finally 1.75 cd/m^2 is selected for motorway lighting standards in the UK. We found out that CWFL is the most efficient commercial light source for the case of photopic luminances of 0.50 and 0.80 cd/m^2, whereas HPS becomes the most efficient one when photopic luminances of 1.25 cd/m^2 and 1.75 cd/m^2 are considered (Figure 6.4). At photopic luminances of 0.50 and 0.80 cd/m^2, CWFL achieves the highest ratio of mesopic luminance to optical radiance of 369.8 and 362.6 lm_{mes}/ W_{opt}. HPS features ratios of 356.6 and 359.9 lm_{mes}/W_{opt}. Considering these values, we place a threshold to our investigated QD-WLED designs; only those having higher luminance than CWFL and HPS at the same radiance values are selected for all four photopic luminance ranges together with CQS ≥80. We designed these QD-WLED spectra similar to Ref.

90 using Gaussian-type spectrum for each color component of blue, green, yellow and red, where the blue is generated by the electroluminescence of an LED chip and other color components are generated by the photoluminescence of quantum dot nanophosphors. We varied the blue wavelength to 450, 470 and 470 nm, the green to 510, 525 and 540 nm, the yellow to 555, 570 and 585 nm, and the red to 600, 620 and 640 nm. Totally, 81 wavelength combinations were tested. We also changed the full-width at half maximum (FWHM) of each of the Gaussian-type spectrum as 25, 35, 45, and 55 nm. FWHM combinations constituted 256 cases: Moreover, the amplitude of the color components were varied over 0, 1, 2 and 3 units and then normalized to 1000. As a result, 529 amplitude combinations were obtained. In total, 10,969,344 QD-WLED designs were generated and the L_{mes} and CQS thresholds mentioned above were applied on them. The simulation results of these QD-LED design variations are summarized in Table 6.2-6.4, which will be discussed one by one below for different luminance level standards.

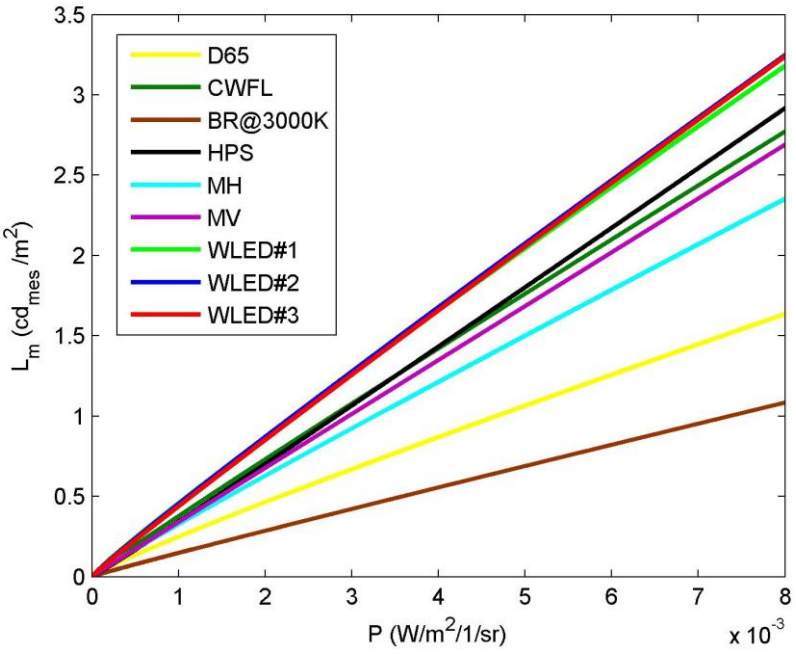

Figure 6.4 Mesopic luminance (L_{mes}) *vs.* radiance (P) for several light sources: standard daylight source (D65), cool white fluorescent lamp (CWFL), blackbody radiator at 3000 K (BR@3000K), metal-halide lamp (MH), high pressure sodium lamp (HPS) and mercury vapor lamp (MV), and our WLED#1, WLED#2, WLED#3.

	Standard 1, WLED#1	Standard 2, WLED#2	Standard 3&4, WLED#3
λ(nm)	450, 525, 570, 620	450, 525, 570, 620	450, 525, 570, 620
Δλ(nm)	25, 45, 25, 25	25, 45, 45, 25	25, 25, 55, 25
a (/1000)	200, 300, 200, 300	182, 273, 182, 364	167, 333, 167, 333

Table 6.2 Spectral parameters of our WLED#1-3 resulting in the highest L_{mes} for all the four standards used. λ: peak emission wavelength, $\Delta\lambda$: FWHM, and a: amplitudes of color components of blue, green, yellow and red.

	Standard 1		Standard 2		Standard 3		Standard 4	
	Average	stdev	Average	stdev	Average	stdev	Average	stdev
L_{mes} (cd_{mes}/m^2)	0.57	0.02	0.89	0.03	1.26	0.04	0.89	0.03
CQS	87.7	2.12	87.6	2.04	1.26	2.00	87.6	2.04
CCT (K)	5,151	1,642	4,854	1,342	4,679	1,223	4,854	1,342

Table 6.3 Average and stdev of L_{mes}, CQS, CCT for QD-WLED designs

	Standard 1		Standard 2	
	Average	stdev	Average	stdev
λ(nm)	458, 524, 569, 623	9.7, 10.4, 12.2, 7.5	458, 525, 569, 622	9.7, 10.3, 12.2, 6.7
Δλ(nm)	41.8, 41.8, 41.3, 41.2	11.0, 11.0, 11.3, 10.7	41.3, 41.8, 41.4, 41.2	11.1, 11.0, 11.3, 10.7
a (/1000)	242, 263, 188, 307	73, 75, 82, 83	230, 264, 190, 316	70, 75, 83, 83
	Standard 3		Standard 4	
	Average	stdev	Average	stdev
λ(nm)	458, 525, 569, 622	9.7, 10.3, 12.2, 6.4	457, 525, 569, 621	9.6, 10.1, 12.2, 4.9
Δλ(nm)	41.0, 41.7, 41.5, 41.3	11.1, 11.0, 11.3, 10.6	41.0, 41.7, 41.5, 41.3	11.2, 11.0, 11.3, 10.6
a (/1000)	222, 264, 190, 323	67, 75, 84, 84	206, 267, 194, 334	62, 75, 83, 83

Table 6.4 Average and stdev of spectral parameters for all four standards studied here. λ: peak emission wavelength, $\Delta\lambda$: FWHM and a: amplitudes of color components of blue, green, yellow and red.

6.3.2 Standard 1: L_p of CWFL = 0.50 cd/m^2

At a radiance level of ca. 1.47 mWm^{-2}sr^{-1}, CWFL provides a L_p of 0.50 cd/m^2 and a L_{mes} of 0.54 cd$_{mes}$/m^2. QD-WLED designs exhibiting the same radiance and having higher L_{mes} values and CQS ≥80 are selected. 61,736 LED spectra, corresponding to only 0.56% of the whole spectra tested, passed these thresholds. This finding shows that careful spectral design is required to generate an efficient light source, as in the case of indoor lighting [90]. Our results also indicate that QD-WLEDs can achieve a L_{mes} of 0.65 cd$_{mes}$/m^2 with a CQS of 85.7. This L_{mes} value is ca. 20% better than what CWFL provides. At this radiance, spectrum giving the highest L_{mes} (WLED#1) reaches a L_p of 0.57 cd/m^2, which still remains within the same standards as CWFL with L_p=0.50 cd/m^2 does. Furthermore, correlated color temperature (CCT) of this spectrum turns out to be 5,437 K. The spectral parameters of WLED#1 are given in Table 6.2. By changing the spectral parameters, one can achieve CQS up to 96.5 and CCT can be set within a very broad range from 2,362 K -corresponding to a warm white- to 24,066 K, which is a bluish cold white. As given in Table 6.3, the average L_{mes} of the spectra passing the thresholds is 0.57 cd$_{mes}$/m^2, which is 5% higher than L_{mes} of CWFL. Standard deviation (stdev) of L_{mes} turns out to be 0.02 cd$_{mes}$/m^2; 65% and 96% of the spectra tested have L_{mes} values between the average L_{mes} ± 1 stdev and the average L_{mes} ± 2 stdev, respectively. This points out that an extraordinary enhancement of L_{mes} at such a level of 20% is really hard to achieve and requires good spectral tuning. Average of CQS (87.7) shows that good color rendering can be obtained using QD nanophosphors while still providing a better L_{mes} than CWFL. Very low stdev of CQS values of the spectra passing the thresholds, only 2.12, supports this observation. In addition, the average of CCT turns out to be 5,150 K, which is 20% higher than the CCT of CWFL.

An important point that we need to understand is the set of spectral parameters, i.e., the peak emission wavelength (λ_i), FWHM ($\Delta\lambda_i$) and the

amplitudes of color components (a_i) required to produce spectra with high performance for road lighting applications (where the subscript *i* is blue (b), green (g) or red (r)). The average and standard deviation (stdev) of these parameters are listed in Table 6.4. Blue color component has an average and stdev of λ_b of 457.5 nm and 9.67 nm, respectively. The average values of λ_g, λ_y, and λ_r are 524.2, 569.1 and 622.6 nm. Green and yellow components have stdev larger than 10 nm; however, interestingly red exhibits a very low stdev. This shows that the peak emission wavelength of the red component should definitely be in the close vicinity of 620 nm as in the case of efficient indoor lighting [90]. Furthermore, we find out from the stdev values given in Table 6.4 that FWHMs can vary significantly while still satisfying high L_{mes} and CQS as opposed to the case of indoor lighting. When it comes to the amplitudes of the color components, the red one is the most dominant one and the yellow is the weakest. However, their large stdev provides us enough room to play with these values while still satisfying high L_{mes} and CQS. We also investigate the performance of the spectrum defined by the average values (Table 6.4). We find that this spectrum provides a very good CQS of 94.5 together with a L_p of 0.49 cd/m^2 and L_{mes} of 0.57 cd_{mes}/m^2, which is much lower than the maximum attainable L_{mes}.

6.3.3 Standard 2: L_p of CWFL = 0.80 cd/m^2

At a radiance level of 2.36 $mWm^{-2}sr^{-1}$, CWFL has a L_p of 0.80 cd/m^2 and a L_{mes} of 0.85 cd_{mes}/m^2. The number of QD-WLED spectra having higher L_{mes} values than CWFL while featuring CQS larger than 80 at the same time decreases to only 0.46% of the designs tested at this radiance. As in the previous case, this finding shows how important the spectral design is in order to achieve high-quality road lighting. By changing the spectral parameters of QD-WLEDs, we can achieve a L_{mes} of 1.01 cd_{mes}/m^2 with a CQS of 85.8 at the same radiance, which is 19% higher than CWFL. This spectrum (WLED#2) has a CCT of 4,563

K, only 6% higher than that of CWFL. Moreover, its L_p is 0.94 cd/m^2, which still satisfies the requirements of the same standards as CWFL does at this radiance. The parameters of this spectrum are presented in Table 6.2. Playing with the parameters of QD-WLED, a CQS of 96.1 can be reached and CCTs between 2,347 and 15,267 K can be obtained while still providing good color rendering and a high L_{mes}. The average L_{mes} of the QD-WLEDs passing the stated thresholds is 0.89 cd_{mes}/m^2, whereas the average CQS and CCT are 87.6 and 4,854 K, respectively (Table 6.3). The stdev of L_{mes} is only 0.03 cd_{mes}/m^2, and the ratio of the spectra having L_{mes} between the average L_{mes} ± 1 and 2 stdev, which defines an interval far away from the maximum L_{mes}, to the number of spectra exceeding the thresholds are 65% and 96%, respectively. As a result, again we conclude that careful spectral tuning is the key to achieving high L_{mes} (as high as 1.01 cd_{mes}/m^2). Although obtaining a very high L_{mes} is challenging, a large CQS can be reached more easily as the high average and the low stdev of CQS indicate (Table 6.3). A further remark is that increasing radiance limitation allows spectra with warmer shade to pass the thresholds applied for this standard. Investigation of average and stdev of the spectral parameters (Table 6.4) does not lead to any significant conclusion different than the previous case where L_p of CWFL is 0.50 cd/m^2. However, one point worth mentioning is that the amplitude of the blue component decreases with increasing red component. In addition, we computed that this average spectrum provides a CQS of 93.8, a L_p of 0.81 cd/m^2 and a L_{mes} of 0.90 cd_{mes}/m^2.

6.3.4 Standard 3: L_p of HPS = 1.25 cd/m^2

Increasing the photopic luminance level to 1.25 cd/m^2 changes the type of the light source that we compare. As mentioned before, HPS becomes the efficient source at this luminance with a radiance of 3.39 $mWm^{-2}sr^{-1}$. The mesopic luminance of HPS then becomes 1.21 cd_{mes}/m^2. The number of QD-WLED spectra, whose L_{mes} values pass this value and have CQS ≥80 at the same

radiance, is 45,043 corresponding to ca. 0.41% of the designs tested. This shows that our conclusions about the careful spectral designs are still valid at this radiance level. The highest L_{mes} achieved by a QD-WLED becomes 1.42 cd_{mes}/m^2, 19% higher than what HPS provides. CQS and L_p of this design (WLED#3) are 85.2 and 1.36 cd/m^2, which remains in the same road lighting standard as HPS. The spectral parameters of WLED#3 can be found in Table 6.2. The CCT values of the tested spectra cover a range between 2,347 and 12,926 K, which corresponds to white light spectra having reddish to bluish shades. Furthermore, a CQS of 95.4 can be achieved using quantum dot nanophosphors. Average L_{mes} of the designs are 1.26 cd_{mes}/m^2 with a stdev of 0.04 cd_{mes}/m^2. This finding shows that obtaining enhanced L_{mes} requires careful spectral optimization, as we concluded for the previous two cases. The average of CQS and its stdev are almost the same as in the previous cases. When it comes to the average and stdev of spectral parameters, we again have almost the same findings as in the previous cases. One important point to mention is that increasing L_p level slightly decreases the amplitude of the blue component and slightly increases the amplitude of the red component. Photometric performance of this average spectrum is as follows: CQS=93.9, L_p=1.17 cd/m^2, L_{mes}=1.26 cd_{mes}/m^2.

6.3.5 Standard 4: L_p of HPS = 1.75 cd/m^2

Finally, increasing the radiance level of HPS to 4.74 $mWm^{-2}sr^{-1}$ increases its L_p to 1.75 cd/m^2 and its L_{mes} to 1.71 cd_{mes}/m^2. The number of QD-WLED designs having better L_{mes} at this radiance decreases down to 27,395 corresponding to only 0.25% of the spectra under test. Together with the previous findings, one can easily conclude that obtaining L_{mes} higher than these of the conventional sources is more challenging as the radiance and correspondingly photopic luminance levels increase. WLED#3 provides the highest L_{mes} at this radiance

level as well. This time it achieves a L_{mes} of 1.98 cd_{mes}/m^2, 16% higher than what HPS can supply at the same radiance. Photopic luminance of WLED#3 is 1.91 cd/m^2, which still falls within the desired range of L_p to satisfy the standards. Among the tested spectra, the warmest QD-WLED design provides 2,347 K and the coldest one has a CCT of 9,422 K; furthermore, average CCT decreases to 4,445 K. The average and stdev values of L_{mes} of the designs passing the thresholds are 1.77 and 0.05 cd_{mes}/m^2, respectively. The number of spectra providing $L_{mes} \pm 2$ stdev constitutes 95% of the spectral designs that passed the thresholds. Using this information, we can conclude that achieving a L_{mes} such as 1.91 cd_{mes}/m^2 is still tricky at this radiance level. As in the previous cases, however, obtaining high CQS is much easier as indicated by the high average (87.3) and low stdev (1.82). Investigation of spectral parameters does not reveal a significant change when compared to the previous cases (Table 6.4). Further points that require attention are the decreasing stdev of red peak emission wavelength, and increasing and decreasing amplitudes of red and blue components as the radiance level further increases, respectively. This average spectrum provides a CQS of 93.2, a L_p of 1.68 cd/m^2 and a L_{mes} of 1.77 cd_{mes}/m^2.

6.3.6 Spectral recommendations and electrical efficiency conditions

Considering all the results obtained above, we can state that QD-WLEDs can provide much better optical performance than conventional light sources. However, careful spectral optimization is required. For optimum spectra, we recommend using the highest L_{mes} spectra given in Table 6.2 and in Figure 6.5 instead of using average parameters in Table 6.4. Using these spectra, one can generate 16-20% more optically efficient white light for road lighting applications with QD-WLEDs. On the other hand, high optical performance

does not guarantee low energy consumption. To realize electrically efficient devices, one also needs to overcome the electrical performance of the conventional sources. For example, HPS and CWFL have average power conversion efficiencies (PCEs) of 30% and 50%, respectively [109]. To resolve this issue, we calculated the radiances needed using CWFL and HPS to obtain the highest L_{mes} of QD-WLEDs. We found that CWFL requires 1.78 and 2.82 $mWm^{-2}sr^{-1}$ for the first two cases, respectively; and HPS requires 4.00 and 5.47 $mWm^{-2}sr^{-1}$ for the third and fourth cases, respectively. Radiances generated by QD-WLEDs are 83%, 84%, 85% and 87% of these conventional sources, respectively. By taking the PCEs of CWFL and HPS, we find that QD-WLEDs need to have PCEs of at least 29.1%, 29.4%, 42.5% and 43.5% for being more electrically efficient than these conventional sources, which prove to be feasible.

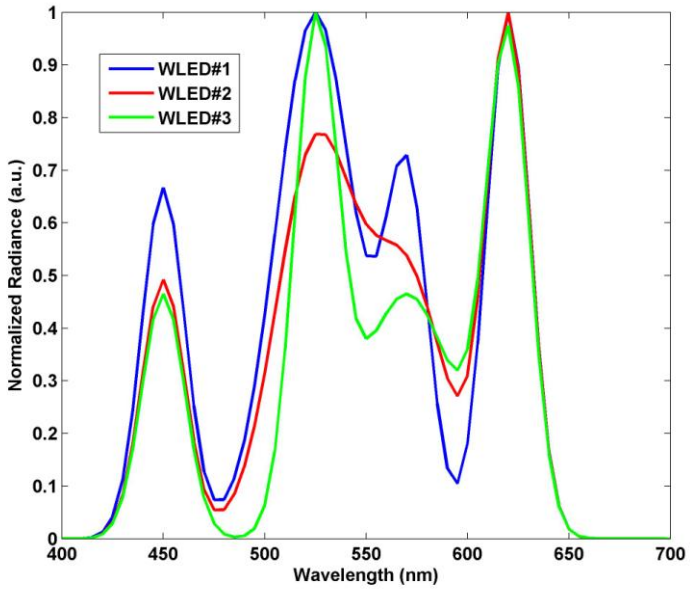

Figure 6.5 QD-WLED spectra leading to the highest mesopic luminance (L_{mes}) for standard 1 (WLED#1), standard 2 (WLED#2), and standards 3&4 (WLED#3).

6.3.7 Conclusions

In conclusion, we show that QD-WLEDs can provide up to 20% higher efficiency at the mesopic light levels than the conventional light sources used for

road lighting, thanks to the combination of their narrow emission bands that are strategically placed. Moreover, we find the necessary spectral parameters for achieving this high performance in four different luminance levels chosen in accordance with the road lighting standards of the USA and UK. Additionally, we predict that these QD-WLEDs are also electrically more efficient as long as their power conversion efficiencies are kept above 70%, 71%, 73% and 75%, depending on the corresponding standards chosen. All in all, these results indicate that quantum dot integrated white LEDs are strong candidates for replacing conventional light sources in the future.

Chapter 7

Colorimetric and Photometric Investigation of Conjugated Polymer Nanoparticles

This chapter is based in part on the publication "White-Emitting Conjugated Polymer Nanoparticles with Cross-Linked Shell for Mechanical Stability and Controllable Photometric Properties in Color-Conversion LED Applications" E.-J. Park, T. Erdem, V. Ibrahimova, S. Nizamoglu, H. V. Demir, and D. Tuncel ACS Nano 5, 2483 – 2492 (2011).

In this chapter, we review our efforts on the generation of white light emission using conjugated polymer nanoparticles whose emission spectra are tunable via the crosslinking mechanism under UV–illumination at 254 nm. Poly[(9,9-dihexylfluorene)-co-alt-(9,9-bis-(3-azidopropyl)fluorene)] (PF3A) polymers are synthesized and converted into a nanoparticle structure by using the reprecipitation method, as described in Chapter 3. The chemical structure of the polymer is given in Figure 7.1 [63]. The nanoparticles are prepared in two different sizes by controlling the concentration of the polymer. The larger particles (PF3A-L) have an average diameter of 166 nm whereas the size of the smaller ones (PF3A-S) is 42 nm. These nanoparticle dispersions are then illuminated under UV-light at a wavelength of 254 nm for durations changing from 1 to 6 hours in air and under nitrogen atmosphere. As a result, azide groups are decomposed into very reactive nitrene species so that crosslinking between

polymer chains is realized. Corresponding photoluminescence graphs of PF3A-L and PF3A-S nanoparticles can be found in Figure 7.2 and 7.3 [63].

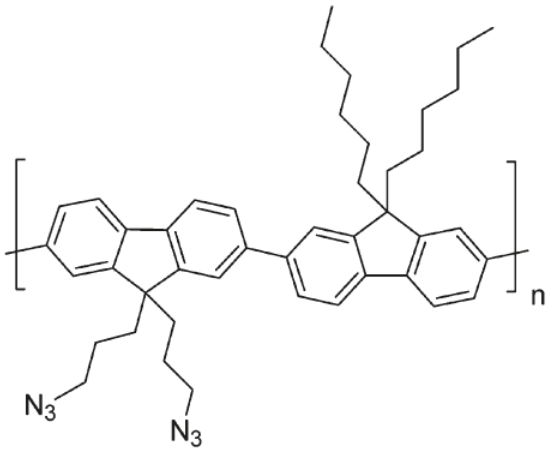

Figure 7.1 Molecular structure of poly[(9,9-dihexylfluorene)-co-alt-(9,9-bis-(3-azidopropyl)fluorene)] (PF3A) [63].

First, photometric investigations are carried out for the nanoparticle dispersions to evaluate their performance. The results of the calculations for PF3A-L conjugated polymer nanoparticles (CNPs) are given in Table 7.1 [63]. We found out that the CCTs of the dispersions cannot be calculated except the case of crosslinking for 6 h. The reason for this is the very dominant blue emission of the nanoparticles. As the crosslinking duration increases, the green-yellow content gets stronger compared to blue, as a result the emitted color changes from blue to yellowish white. These changes can easily be followed from Figure 7.2. Since the green-yellow content of the spectrum increases as the crosslinking time is increased, LER levels increase whereas S/P becomes even lower because the emission spectra starts having a better match to photopic eye sensitivity function compared to the scotopic eye sensitivity function. Another point that deserves attention is the stronger increase of green-yellow content of the spectrum upon crosslinking in an oxygen-free atmosphere. This results in higher LERs and lower S/P values.

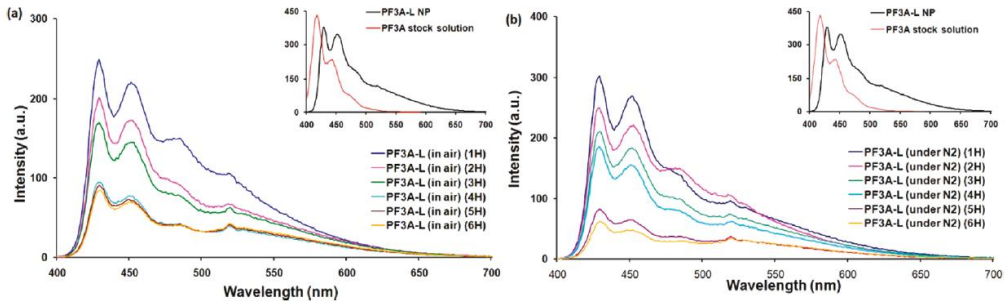

Figure 7.2 Photoluminescence graphs of PF3A-L nanoparticles crosslinked (a) in air and (b) under nitrogen atmosphere for varying durations between 1 and 6 hours [63].

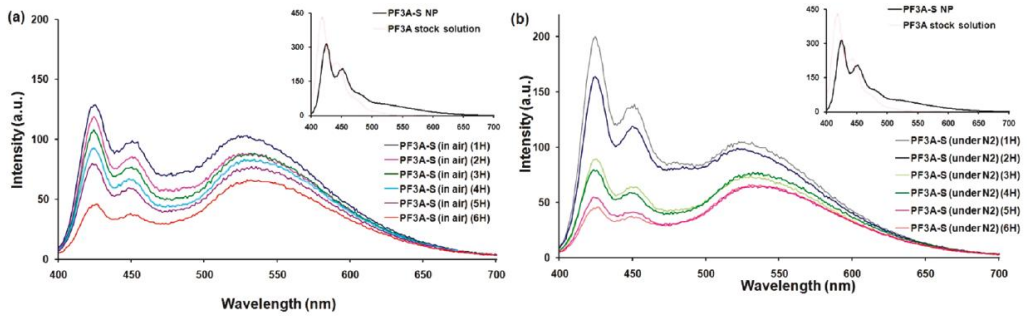

Figure 7.3 Photoluminescence graphs of PF3A-S nanoparticles crosslinked (a) in air and (b) under nitrogen atmosphere for varying durations between 1 and 6 hours [63].

Crosslinking has similar consequences on the small nanoparticles (PF3A-S) as it can be seen in Figure 7.3. Increased crosslinking duration strengthens the relative content of green-yellow part. Consequently, LER increases and S/P decreases as the nanoparticles are hold under UV illumination. More importantly, crosslinking has a more significant effect on the emission spectrum of the particles. Compared to larger particles, PF3A-S nanoparticles exhibit lower CCTs and S/Ps and higher LERs as a natural consequence of stronger rising of green-yellow content of the emission spectrum (Figure 7.2). The LER values came out to be as high as 350 lm/W_{opt}, which is really a high level for a broad band emitter while still preserving S/Ps over 2.00.

Nanoparticle	CCT (K)	LER (lm/W_{opt})	S/P	x	y
PF3A-L NP	N/A	188	4.56	0.1928	0.1838
PF3A-L NP (1H, in air)	N/A	203	4.51	0.1879	0.2065
PF3A-L NP (2H, in air)	N/A	199	4.27	0.1985	0.1960
PF3A-L NP (3H, in air)	N/A	207	4.08	0.2029	0.2057
PF3A-L NP (4H, in air)	N/A	224	3.72	0.2127	0.2243
PF3A-L NP (5H, in air)	N/A	235	3.55	0.2187	0.2380
PF3A-L NP (6H, in air)	52117	247	3.38	0.2249	0.2523
PF3A-L NP (1H, under N_2)	N/A	192	4.42	0.1955	0.1879
PF3A-L NP (2H, under N_2)	N/A	203	4.48	0.1887	0.2064
PF3A-L NP (3H, under N_2)	N/A	203	4.18	0.2006	0.2013
PF3A-L NP (4H, under N_2)	N/A	201	4.16	0.2007	0.1982
PF3A-L NP (5H, under N_2)	N/A	228	3.68	0.2134	0.2311
PF3A-L NP (6H, under N_2)	24231	260	3.22	0.2314	0.2687

Table 7.1 Photometric computation results of PF3A-L dispersions for different cross-linking durations [63].

Nanoparticle	CCT	LER	S/P	x	y
PF3A-S NP	N/A	165	4.45	0.1950	0.1720
PF3A-S NP (1H, in air)	N/A	220	3.42	0.2216	0.2364
PF3A-S NP (2H, in air)	8462	299	2.59	0.2662	0.3347
PF3A-S NP (3H, in air)	7733	311	2.45	0.2750	0.3489
PF3A-S NP (4H, in air)	7293	320	2.37	0.2813	0.3602
PF3A-S NP (5H, in air)	6090	349	2.11	0.3075	0.3987
PF3A-S NP (6H, in air)	5835	355	2.04	0.3155	0.4071
PF3A-S NP (1H, under N_2)	15286	263	2.95	0.2428	0.2893
PF3A-S NP (2H, under N_2)	13261	272	2.91	0.2463	0.3019
PF3A-S NP (3H, under N_2)	7865	310	2.49	0.2727	0.3476
PF3A-S NP (4H, under N_2)	7109	324	2.35	0.2842	0.3660
PF3A-S NP (5H, under N_2)	6490	342	2.22	0.2964	0.3881
PF3A-S NP (6H, under N_2)	6257	353	2.19	0.3013	0.4033

Table 7.2 Photometric calculation results of PF3A-S dispersions at different crosslink durations [63].

After investigating these photometric properties of the dispersions, we move to the optical properties of the films prepared by drop-casting on a quartz substrate. The resulting films showed significant differences from the dispersions. For both of the nanoparticles, i.e., PF3A-L and PF3A-S sharp peaks emerged in the green-yellow region of the photoluminescence curve (Figures 7.4) [63]. The intrinsic properties of the material is not expected to yield such a difference in the emission spectrum; therefore, we believe that the spectral

sharpening might be due to the optical effects caused by the environmental and morphological changes though we still do not have a conclusive remark.

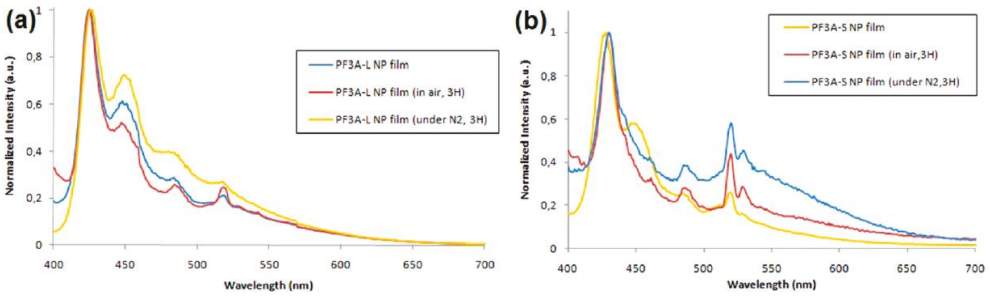

Figure 7.4 Photoluminescence spectra of the films prepared using (a) PF3A-L NP and (b) PF3A-S NP dispersions that are not crosslinked at all and crosslinked for 3 hours in air and under nitrogen [63].

Because the green-yellow content of the films of PF3A-L nanoparticles is weak, their photometric properties are clearly very bad, even not worth calculating. Therefore, we only calculated the photometric performance of the films of PF3A-S nanoparticles. Their photometric performance remained lower compared to the dispersion case. For example, blue content in their spectrum is so dominant that CCT of none of the films could be calculated. The LER of the not-crosslinked particles is 137 lm/W_{opt}, whereas crosslinking increases the LER levels to 195 lm/W_{opt} and 209 lm/W_{opt} depending on the environment, i.e., air or nitrogen atmosphere, respectively. As a consequence of the strengthening of green-yellow content, S/P values decrease from 5.32 of not-crosslinked nanoparticles to 3.64 and 3.47 of the films made of nanoparticles crosslinked for 3 hours in air and under nitrogen, respectively. These results and CIE 1931 chromaticity coordinates of the photoluminescence spectra of these films are given in Table 7.3 [63].

By considering these results, we integrated only PF3A-S nanoparticles crosslinked for 3 hours on a near-UV LED made of InGaN/GaN emitting at 380 nm. The final spectra followed the photoluminescence curves of the films as expected. The corresponding electroluminescence graph is given in Figure 7.5 [63].

Nanoparticle	CCT (K)	LER (lm/W_{opt})	S/P	x	y
PF3A-S NP-film	N/A	137	5.32	0.1820	0.1363
PF3A-S NP-film (3H,in air)	N/A	195	3.64	0.2144	0.2152
PF3A-S NP-film (3H,in N_2)	N/A	209	3.47	0.2209	0.2299

Table 7.3 Results of the photometric calculations carried out on the photoluminescence of the films made of PF3A-S nanoparticles [63].

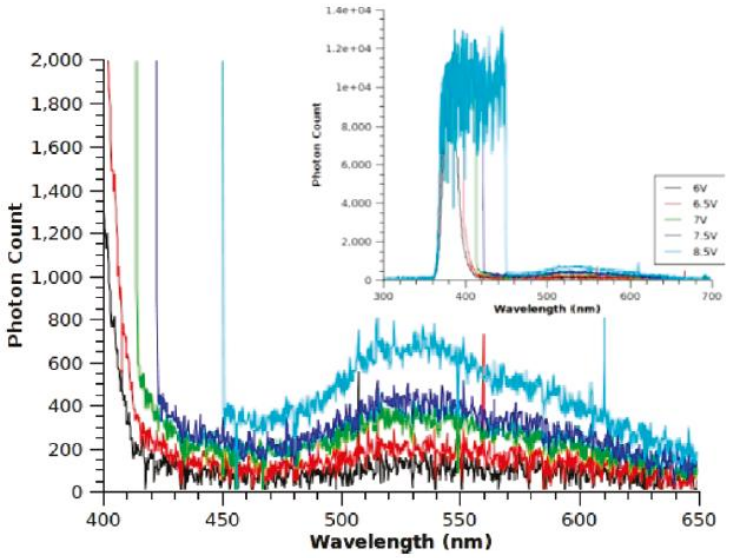

Figure 7.5 Electroluminescence spectrum of the final device where PF3A-S nanoparticles are integrated on a near-UV LED [63].

In conclusion, in this work we investigated the properties of polymer nanoparticles from a colorimetric and photometric point of view. We found out that the optical properties of the nanoparticles can be tuned within a wide range via crosslinking. However, the performance turned out to be inappropriate for indoor lighting applications but more suitable for outdoor applications as it can possess very high S/P values.

Chapter 8

Conclusion

In this thesis, we reviewed our efforts on high-quality and highly efficient white light generation at different light levels appropriate for indoor and outdoor lighting. To achieve the required performance levels, we made use of novel materials such as colloidal semiconductor quantum dots and conjugated polymer nanoparticles, both of which enable good spectral tuning.

First, we reviewed the basics of color science and photometry, which we use for evaluating the quality of the emitted light and for defining the generated color. Within the frame work of color science, we presented the color matching functions and color spaces together with the correlated color temperature that are used to define the colors of the objects and emitted light. Furthermore, two important metrics, color rendering index and color quality scale, are discussed, which are used to evaluate the capability of the light sources in rendering the real colors of the objects. In addition, we explained some important radiometric and photometric criteria such as luminous efficacy of optical radiation, efficiency ratios of scotopic to photopic visions (S/P), photopic and mesopic luminances after defining the eye sensitivity functions corresponding to the ambient light level.

Next we moved to the description of materials that have been in the focus of this thesis: quantum dots and conjugated polymer nanoparticles. We discussed their optical properties followed by their potentials for white light applications having high-efficiency and high-quality. As the quantum dots have very narrow emission bands, they allow for good spectral tuning so that the properties of the

generated white light can be easily controlled. On the other hand, crosslinking of the polymer nanoparticles provides another pathway for tunable light generation.

After describing the most widely preferred method for white light emitting diode designs, we presented trade-offs of the photometric performance criteria and provided spectral recommendations for high-quality white light generation for indoor lighting using quantum dot nanoluminophors. Then we continued with our experimental work on the state-of-the art white LED in terms of photometric performance for indoor applications. In the following section we explained our theoretical photon conversion model, which we developed for predicting the electrical performance of the quantum dot integrated white light emitting diodes, and showed that these devices can reach significant levels of efficiency and has a great potential to surpass the traditional light sources and existing LED technologies both photometrically and electrically.

Subsequently, we focused on the outdoor lighting instead of indoor lighting. Since the corresponding luminance levels are very different than indoor applications, the spectral requirements of the efficient light sources change significantly. Considering these changes, we presented spectral recommendations for efficient white light generation, which can enhance the vision in scotopic and mesopic vision regimes; using quantum dot integrated white LEDs.

Finally, we evaluated colorimetric and photometric performance of conjugated polymer nanoparticles. Especially, observing and quantifying the evaluations in their photometric performances showed that crosslinkable polymer nanoparticles can be a novel class of materials, which allow for color tuning and, as a result, become a good alternative material for white light generation in outdoor applications.

In conclusion, we presented our research work in high-quality high-efficiency light generation for indoor and outdoor lighting applications. Considering the deep-red emission tail issue of phosphors, and the cost and green gap problem of multichip LED approaches, we can easily claim that quantum dots can open up a new path for achieving the targeted efficiency levels of 200 lm/W_{elect} [75] so that the energy consumption for lighting decreases significantly. As crosslinkable conjugated polymer nanoparticles are totally novel materials, they can also be integrated in white light emitting diodes after spectral optimization.

The results of this thesis work led to 5 science citation index (SCI) papers and 3 peer-reviewed international conference papers along with 5 SCI papers in submission and one conference paper in submission, which are listed below:

SCI papers:

1. T. Erdem, S. Nizamoglu, X.W. Sun and H. V. Demir, *Optics Express*, 18, 340-347 (2010).
2. S. Nizamoglu, T. Erdem, X. W. Sun and H. V. Demir, *Optics Letters*, 35, 20, 3372-3374 (2010).
3. S. Nizamoglu, T. Erdem and H. V. Demir, *Optics Letters*, 36, 1893 (2011).
4. T. Erdem and H. V. Demir, *Nature Photonics*, 5, 126 (2011). Correspondence letter.
5. E.-J. Park, T. Erdem, V. Ibrahimova, S. Nizamoglu, H. V. Demir and D. Tuncel, *ACS Nano*, 5, 2483 (2011).

SCI papers in submission:

6. T. Erdem, S. Nizamoglu, H. V. Demir, "Power conversion and luminous efficiency performance of semiconductor quantum dot nanophosphors on light-emitting diodes," in submission.
7. T. Erdem, S. Nizamoglu, X. W. Sun, H. V. Demir,"Efficient street lighting with good color rendering using semiconductor quantum dot nanophosphors," in submission.

8. T. Erdem, S. Nizamoglu, X. W. Sun, H. V. Demir, “Computational analyses of white LEDs exhibiting high color rendition and high scotopic/photopic efficacy ratio for outdoor lighting applications,” in submission.
9. S. Nizamoglu, T. Erdem, H. V. Demir, N. Gaponik, A. Eychmüller, “Quantum dot integrated LEDs based on photonic and excitonic color conversion” in submission.
10. T. Erdem, V. Ibrahimova, D. Tuncel, H. V. Demir, “Hybrid structures of polyflourene nanoparticles and InGaN/GaN quantum well nanopillars,” in submission.

Peer-reviewed international conference publications:

11. S. Nizamoglu, T. Erdem, X. W. Sun and H. V. Demir, CLEO/IQEC Baltimore, Maryland, USA, May 1-6, 2011. Paper Efficient Lighting AWA2.
12. T. Erdem, S. Nizamoglu and H. V. Demir, Proceedings of 23rd IEEE Annual Photonics Society Meeting, Denver, CO, USA (7 – 11 November 2010). Session: ThL: LED Technologies. Paper: ThL 5.
13. B. Guzelturk, T. Erdem, E. Unal, S. Nizamoglu, D. Tuncel and H. V. Demir, Proceedings of 23rd IEEE Annual Photonics Society Meeting, Denver, CO, USA (7 – 11 November 2010). Session: TuE: Engineered Quantum Dot Devices and Materials. Paper: TuE 3.

International conference publications in submission:

14. T. Erdem, S. Nizamoglu, H. V. Demir, “Power conversion and luminous efficiency performance of nanophosphor quantum dots on color-conversion LEDs for high-quality general lighting,” submitted for SPIE Photonics West 2011.

BIBLIOGRAPHY

[1] S. A. Zimov, E. A. G. Schuur, F. S. Chapin III, "Permafrost and the global carbon budget," Science, 2006, pp. 1612-1613.

[2] F. Scrimgeour, L. Oxley, K. Fatai, "Reducing carbon emissions? The relative effectiveness of different types of environmental tax: The case of New Zealand," Environmental Modeling & Software, 2005, pp. 1439-1448.

[3] S. Pacala and R. Socolow, "Stabilization wedges: Solving the climate problem for the next 50 years with current technologies," Science, 2004, pp. 968-979.

[4] D. Irvine-Halliday, R. Peon, G. Doluweera, I. Platonova, G. Irvine-Halliday,"Solid state lighting: The only solution for the developing world," SPIE Newsroom, 2006.

[5] R. Peon, S. Leon, D. Irvine-Halliday, "Solid state lighting for the developing countries: A cost effective solution, facilitator of gender equity and encourager of peace," Proceedings of World Renewable Energy Congress VIII, 2004.

[6] Energy Savings Estimates of Light Emitting Diodes in Niche Lighting Applications, Building Technologies Program, Office of Energy Efficiency and Renewable Energy, U.S. Department of Energy, 2011.

[7] G. Wyszecki and W. S. Stiles, *Color Science Concepts and Methods, Quantitative Data and Formulae*, 2nd ed. Wiley, 2000.

[8] W. K. Stell, "The morphological organization of the vertebrate retina," in: *Handbook of Sensory Physiology*. Springer-Verlag, 1972.

[9] E. F. Schubert, *Light-Emitting Diodes*. Cambridge University Press, 2000.

[10] J. E. Dowling and B. B. Boycott, "Organization of the primate retina: Electron microscopy," Proc. Roy. Soc., pp 80-111.

[11] CIE Proceedings 1931. Cambridge University Press, 1931.

[12] A. Stockman, Colorimetry, in: T. G. Brown, K. Creath, H. Kogelnik, M. A. Kriss, J. Schmit, M. J. Weber (Eds.), *The Optics Encyclopedia: Basic Foundations and Practical Applications*. Wiley-VCH, 2004.

[13] CIE data of 1960 for (u,v) coordinates can be found in CIE, 1986.

[14] CIE data of 1960 for (u',v') coordinates can be found in CIE, 1986.

[15] CIE publication No. 15, "Colorimetry," 1971.

[16] CIE publication No. 13.3, "Method of measuring and specifying color-rendering of light sources," 1995.

[17] W. Davis and Y. Ohno, "Color quality scale," Optical Engineering, 2010, pp. 033602.

[18] C. J. Li, M. R. Luo, B. Rigg and R. W. G. Hunt, "CMC 2000 chromatic adaptation transform: CMCCAT2000," Color Res. Appl., 2002, pp. 49-58.

[19] M. Rea, M. G. Figueiro, A. Bierman and J. D. Bullough, "Circadian light," 2010, J Circadian Rythms, 8:2.

[20] CIE Proceedings 1951, 1951.

[21] Osram Sylvania Corporation, "Lumens and mesopic vision," Application Note FAQ0016-0297, 2000.

[22] L. B. Johnson, "Upper limit of mesopic vision," Trans. Illum. Eng. Soc. 1937, pp. 646-650.

[23] Y. LeGrand, *Handbook of sensory physiology, Vol. VII/4 Visual psychophysics*. Springer-Verlag, 1972.

[24] S. Kokoschka, "Das V(λ)-Dilemma in der Photometrie," in Proceedings of 3. Internationales Forum fur den lichttechnischen Nachswuchs, 1997.

[25] IESNA Illuminating Engineering Society of North America, *IESNA Lighting Handbook: Reference and Application, 9th ed.* 2000.

[26] CIE 41:1978, "Light as a true visual quantity: Principles of measurement," 1978.

[27] M. S. Rea, J. D. Bullough, J. P. Freyssinier-Nova, and A. Bierman, "A proposed unified system of photometry," Lighting Res. Technol., 2004, pp. 85-111.

[28] M. Eloholma, M. Viikari, L. Halonen, H. Walkey, T. Goodman, J. Alfrendick, A. Freiding, P. Bodrogi and G. Várady, "Mesopic models – from brightness matching to visual performance in night-time driving: a review," Lighting Res. Technol., 2005, pp. 155-175.

[29] T. Goodman, A. Forbes, H. Walkey, M. Eloholma, L. Halonen, J. Alferdinck, A. Freiding, P. Bodrogi, G. Várady and A. Szalmas, "Mesopic visual efficiency IV: A model with relevance to night-time driving and other applications," Lighting Res. Technol., 2007, pp. 365-392.

[30] CIE Technical Report 191:2010, "Recommended system for mesopic photometry based on visual performance," 2010.

[31] S. M. Berman, "Energy Efficiency Consequences of Scotopic Sensitivity," J. Illum. Eng. Soc., 1992, pp. 3-14.

[32] R. Koole, "Fundamentals and applications of semiconductor nanocrystals," 2008, (PhD Thesis, Utrecht University, Utrecht).

[33] A. J. Houtepen, "Charge injection and transport in quantum confined and disordered systems," 2007, (PhD Thesis, Utrecht University, Utrecht).

[34] S. F. Wuister, "Optical studies of capped quantum dots," 2005, (PhD Thesis, Utrecht University, Utrecht).

[35] S. V. Gaponenko, *Optical Properties of Semiconductor Nanocrystals.* Cambridge University Press, 1998.

[36] L. E. Brus, "Electron-electron and electron-hole interactions in small semiconductor crystallites: the size dependence of the lowest excited electronic state," J. Chem. Phys., 1984, pp. 4403-4409.

[37] A. Franceschetti and A. Zunger, "Pseudopotential calculations of electron and hole addition spectra of InAs, InP, and Si quantum dots," Phys. Rev. B: Condens. Matter Mater. Phys. 2000, pp. 2614-2623.

[38] S. Kudera, L. Carbone, L. Manna and W. J. Parak, "Growth mechanism, shape and composition control of semiconductor nanocrystals," *Semiconductor Nanocrystal Quantum Dots,* ed. A. L. Rogach. Springer-Verlag, 2008.

[39] L. Manna, E. C. Scher and A. P. Alivisatos, "Synthesis of soluble and processable rod-, arrow-, teardrop-, and tetrapod-shaped CdSe nanocrystals," J. Am. Chem. Soc., 2000, pp. 12700-12706.

[40] Z. A. Peng and X. G. Peng, "Mechanisms of the shape evolution of CdSe nanocrystals," J. Am. Chem. Soc., 2001, pp. 1389-1395.

[41] C. B. Murray, D. J. Norris and M. G. Bawendi, "Synthesis and characterization of nearly monodisperse CdE (E=S, Se, Te) semiconductor nanocrystallites," J. Am. Chem. Soc., 1993, pp. 8706-8715.

[42] W. W. Yu, Y. A. Wang and X. Peng, "Formation and stability of size-, shape-, structure-controlled CdTe nanocrystals: ligand effects on monomers and nanocrystals," Chem. Mater. 2003, pp. 4300-4308.

[43] P. Reiss, "Synthesis of semiconductor nanocrystals in organic solvents," *Semiconductor Nanocrystal Quantum Dots*, ed. A. L. Rogach, Springer-Verlag, 2008.

[44] D. V. Talapin, A. L. Rogach, A. Kornawski, M. Haase and H. Weller, "Highly luminescent monodisperse CdSe and CdSe/ZnS nanocrystals synthesized in a hexadecylamine-trioctylphosphine oxide-trioctylphosphine mixture," Nanoletters, 2001, pp. 207-211.

[45] A. M. Munro, I. J. L. Plante, M. S. Ng and D. S. Ginger, "Quantitative study of the effects of surface ligand concentration on CdSe nanocrystal photoluminescence," J. Phys. Chem. C, 2007, pp. 6220-6227.

[46] E. Jang, S. Jun, Y. S. Chung and L. S. Pu, "Surface treatment to enhance the quantum efficiency of semiconductor nanocrystals," J. Phys. Chem. B, 2004, pp. 4597-4600.

[47] O. I. Micic, H. M. Cheong, H. Fu, A. Zunger, J. R. Sprague, A. Mascarenhas and A. J. Nozik, "Size-dependent spectroscopy of InP quantum dots," J. Phys. Chem. B, 1997, pp. 4904-4912.

[48] D. V. Talapin, N. Gaponik, H. Borchert, A. L. Rogach, M. Haase and H. Weller, "Etching of colloidal InP nanocrystals with fluorides: photochemical nature of the process resulting in high photoluminescence efficiency," J. Phys. Chem. B, 2002, pp. 12659-12663.

[49] C. Y. Yeh, Z. W. Lu, S. Froyen and A. Zunger, "Zinc-blende-wurtzite polytypism in semiconductors," Phys. Rev. B, 1992, pp. 10086-10097.

[50] W. W. Yu, L. Qu, W. Guo and X. Peng, "Experimental Determination of the Extinction Coefficient of CdTe, CdSe, and CdS Nanocrystals," Chem. Mater., 2003, pp. 2854-2860.

[51] N. Gaponik and A. L. Rogach, "Aqueous synthesis of semiconductor nanocrystals," *Semiconductor Nanocrystal Quantum Dots*, ed. A. L. Rogach. Springer-Verlag, 2008.

[52] N. Gaponik, D. V. Talapin, A. L. Rogach, K. Hoppe, E. V. Shevchenko, A. Kornowski, A. Eychmüller and H. Weller, "Thiol-capping of CdTe nanocrystals: an alternative to organometallic synthetic routes," J. Phys. Chem. B 2002, pp. 7177-7185.

[53] S. J. Rosentha, "Bar-coding biomolecules with fluorescent nanocrystals," Nat. Biotechnol., 2001, pp. 621-622.

[54] N. Gaponik, **"**Assemblies of thiol-capped nanocrystals as building blocks for use in nanotechnology," J. Mater. Chem., 2010, pp. 5174-5181.

[55] M. Protie`re and P. Reiss, "Facile synthesis of monodisperse ZnS capped CdS nanocrystals exhibiting efficient blue emission," Nanoscale Res. Lett., 2006, pp. 62–67.

[56] E. Jang, S. Jun, H. Jang, J. Lim, B. Kim and Y. Kim, "White-light-emitting diodes with quantum dot color converters for display backlights," Adv. Mater., 2010, pp. 3076-3080.

[57] C. B. Murray, D. J. Norris and M. G. Bawendi, "Synthesis and characterization of nearly monodisperse CdE (E=S, Se, Te) semiconductor nanocrystallites," J. Am. Chem. Soc., 1993, pp. 8706-8715.

[58] D. Tuncel and H. V. Demir, "Conjugated polymer nanoparticles," Nanoscale, 2010, pp. 484-494.

[59] P. Sarrazin, D. Chaussy, L. Vurth, O. Stephan and D. Beneventi, "Semiconducting Polymer Nanospheres in Aqueous Dispersion Prepared by a Miniemulsion Process," Langmuir, 2009, pp. 651-655.

[60] K. Müller, M. Klapper and K. Müllen, "Synthesis of Conjugated Polymer Nanoparticles in Non-Aqueous Emulsions," Macromol. Rapid Commun., 2006, pp. 586-593.

[61] A. Berkefeld and S. Mecking, "Mechanistic Studies of Catalytic Polyethylene Chain Growth in the Presence of Water," Angew. Chem., Int. Ed., 2006, pp. 6044-6046.

[62] M. C. Baier, J. Huber and S. Mecking, "Fluorescent Conjugated Polymer Nanoparticles by Polymerization in Miniemulsion," J. Am. Chem. Soc., 2009, pp. 14267-14273.

[63] E.-J. Park, T. Erdem, V. Ibrahimova, S. Nizamoglu, H. V. Demir and D. Tuncel, "White-Emitting Conjugated Polymer Nanoparticles with Cross-Linked Shell for Mechanical Stability and Controllable Photometric Properties in Color-Conversion LED Applications," ACS Nano, 2011, pp. 2483-2492.

[64] J. H. Moon, R. Deans, E. Krueger and L. F. Hancock, "Capture and detection of a quencher labeled oligonucleotide by poly(phenylene ethynylene) particles," Chem. Commun., 2003, pp. 104-105.

[65] N. Kurokawa, H. Yoshikawa, N. Hirota, K. Hyodo and H. Masuhara, "Size-Dependent Spectroscopic Properties and Thermochromic Behavior in Poly(substituted thiophene) Nanoparticles," ChemPhysChem, 2004, pp. 1609-1615.

[66] T. Piok, C. Gadermaier, F. P. Wenzl, S. Patil, R. Montenegro, K. Landfester, G. Lanzani, G. Cerullo, U. Scherf and E. J. W. List, "The photophysics of

organic semiconducting nanospheres: a comprehensive study," Chem. Phys. Lett., 2004, pp. 7-13.

[67] T. Piok, S. Gamerith, C. Gadermaier, H. Plank, F. P. Wenzl, S. Patil, R. Montenegro, T. Kietzke, D. Nehrer, U. Scherf, K. Landfester and E. J. W. List, "Organic Light-Emitting Devices Fabricated from Semiconducting Nanospheres," Adv. Mater., 2003, pp. 800-804.

[68] T. Kietzke, D. Nehrer, K. Landfester, R. Montenegro, R. Güntner and U. Scherf, "Novel approaches to polymer blends based on polymer nanoparticles," Nat. Mater., 2003, pp. 408-412.

[69] T. Kietzke, D. Nehrer, M. Kumke, R. Montenegro, K. Landfester and U. Scherf, "A Nanoparticle Approach To Control the Phase Separation in Polyfluorene Photovoltaic Devices," Macromolecules, 2004, pp. 4882-4890.

[70] T. Piok, H. Plank, G. Mauthner, S. Gamerith, C. Gadermaier, F. P. Wenzl, S. Patil, R. Montenegro, M. Bouguettaya, J. R. Reynolds, U. Scherf, K. Landfester and E. J. W. List, "Solution Processed Conjugated Polymer Multilayer Structures for Light Emitting Devices," Jpn. J. Appl. Phys., 2005, pp. 479-484.

[71] G. Mauthner, K. Landfester, A. Köck, H. Brückl, M. Kast, C. Stepper and E. J. W. List, "Inkjet printed surface cell light-emitting devices from a water-based polymer dispersion," Org. Electron., 2008, pp. 164-170.

[72] E. Fisslthaler, S. Sax, U. Scherf, G. Mauthner, E. Moderegger, K. Landfester and E. J. W. List, "Inkjet printed polymer light-emitting devices fabricated by thermal embedding of semiconducting polymer nanospheres in an inert matrix," Appl. Phys. Lett., 2008, pp. 183305.

[73] E. Fisslthaler, A. Blümel, K. Landfester, U. Scherf and E. J. W. List, "Printing functional nanostructures: a novel route towards nanostructuring of organic electronic devices via soft embossing, inkjet printing and colloidal

self assembly of semiconducting polymer nanospheres," Soft Matter, 2008, pp. 2448-.

[74] T. Kietzke, D. Nehrer, M. Kumke, R. Montenegro, K. Landfester and U. Scherf, "A Nanoparticle Approach To Control the Phase Separation in Polyfluorene Photovoltaic Devices," Macromolecules, 2004, pp. 4882-4890.

[75] R. Haitz and J. Y. Tsao, "Solid-state lighting: 'The case'10 years after and future prospects," Phys. Status Solidi A, 2011, pp. 17–29 (2011).

[76] R. Peon, G. Doluweera, I. Platonova, D. Irvine-Halliday, G. Irvine-Halliday, "Solid State Lighting for the Developing World – The Only Solution," Optics&Photonics 2005, Proc. SPIE 5941, 2005, pp. 109-123.

[77] http://www.dl-light.com/news/8.html

[78] "Grosses Lichterlöschen für die Glühbirnen," Tagesanzieger, 2008.

[79] J. Kanter, "Europe's Ban on Old-Style Bulbs Begins". The New York Times, 2010.

[80] "Canada to ban incandescent light bulbs by 2012," Reuters, 2007.

[81] D. C. Agrawal, H. S. Leff and V. J. Menon, "Efficiency and efficacy of incandescent lamps," Am J. Phys., 1996, pp. 649–654.

[82] Navigant, U.S. Lighting Market Characterization Volume I: National Lighting Inventory and Energy Consumption Estimate, 2002.

[83] J. M. Phillips, M. F. Coltrin, M. H. Crawford, A. J. Fischer, M. R. Krames, R. Mueller-Mach, G. O. Mueller, Y. Ohno, L. E. S. Rohwer, J. A. Simmons and J. Y. Tsao, "Research challenges to ultra-efficient inorganic solid-state lighting," Laser & Photon. Rev., 2007, pp. 307-333.

[84] P. Raynham and T. Saksvrikrønning, "White light and facial recognition," The Lighting Journal, 2003, pp. 29-33 (2003).

[85] M. Yamada, Y. Narukawa, H. Tamaki, Y. Murazaki and T. Mukai, "A methodological study of the best solution for generating white light," IEICE Trans. Electron., 2005, pp. 1860-1869.

[86] S. Guha and N. A. Bojarczuk, "Multicolored light emitters on silicon substrates," Appl. Phys. Lett., 1998, pp. 1487-1489.

[87] O. Graydon, "The new oil?," Nature Photon., 2011, pp. 1.

[88] D.-Y. Wang, C.-H. Huang, Y.-C. Wu and T.-M. Chen "$BaZrSi_3O_9:Eu^{2+}$: a cyan-emitting phosphor with high quantum efficiency for white light-emitting diodes," J. Mater. Chem., 2011, pp. 10818-10822.

[89] T. Erdem and H. V. Demir, "Semiconductor nanocrystals as rare-earth alternatives," Nature Photonics, 2011, pp. 126.

[90] T. Erdem, S. Nizamoglu, X. W. Sun and H. V. Demir, "A photometric investigation of ultra-efficient LEDs with high color rendering index and high luminous efficacy employing nanocrystal quantum dot luminophores", Opt. Express, 2011, pp. 340-347.

[91] A. Žukauskas, R. Vaicekauskas, F. Ivanauskas, R. Gaska, M. S. Shur, "Optimization of white polychromatic semiconductor lamps," Appl. Phys. Lett., 2002, pp. 234-236.

[92] A. R. Robertson, "Computation of correlated color temperature and distribution temperature," J. Opt. Soc. Am., 1968, pp. 1528-1535.

[93] S. Nizamoglu, T. Erdem, X. W. Sun, H. V. Demir, "Warm-white light-emitting diodes integrated with colloidal quantum dots for high luminous efficacy and color rendering," Opt. Lett., 2010, pp. 3372-3374.

[94] M. R. Krames, O. B. Shchekin, R. Mueller-Mach, G. O. Mueller, L. Zhou, G. Harbers and M. G. Craford, "Status and future of high-power light-emitting diodes," J. Display Technol., 2007, pp. 160-175.

[95] DEMA Electronic AG, http://www.zenigata.de/540lm-series.html (accessed on March 30, 2011).

[96] Cree Inc., http://www.cree.com/press/enlarge.asp?i=1174480795673 (accessed on March 30, 2011).

[97] OSRAM Opto Semiconductors GmbH, http://www.osram-os.com/osram_os/EN/Press/Press_Releases/Solid_State_Lighting/2011/From_the_OSRAM_laboratory_-_efficiency_record_for_warm_white.html (accessed on March 30, 2011).

[98] Y. Narukawa, M. Ichigawa, D. Sanga, M. Sano and T. Mukai, "White light emitting diodes with super-high luminous efficacy," J. Phys. D: Appl. Phys., 2010, 354002 (2010).

[99] E. M. Boatman, G. C. Lisensky and K. J. Nordell, "A safer, easier, faster synthesis for CdSe quantum dot nanocrystals,"J. Chem. Educ., 2005, pp. 1697-1699.

[100] D. S. Ginger and N. C. Greenham, "Charge injection and transport in films of CdSe nanocrystals," J. Appl. Phys., 2000, pp. 1361-1368.

[101] S. M. Berman, D. L. Jewett, G. Fein, G. Saika and F. Ashford, "Photopic luminance does not always predict perceived room brightness," Lighting Res. Technol., 1990, pp. 37-41.

[102] W. Davis and Y. Ohno, "Toward an Improved Color Rendering Metric," Proc. SPIE 5941, 2005, 59411G.

[103] S. Nizamoglu, T. Erdem, H. V. Demir, "High scotopic/photopic ratio white-light-emitting diodes integrated with semiconductor nanophosphors of colloidal quantum dots," Opt. Lett., 2011, pp. 1893-1895.

[104] J. A. Borton and K. A. Daley, "A comparison of light sources for the petrochemical industry," IEEE Ind. Appl. Mag., 1997, pp. 54-62.

[105] J. Van Derlofske, J. D. Bullough, and J. Watkinson, "Spectral effects of LED forward lighting," Tech Rep. TLA 2005-02, 2005.

[106] P. Raynham, "An examination of the fundamentals of road lighting for pedestrians and drivers," Lighting Res. Technol., 2004, pp. 307-316.